NASA CONTRACTOR REPORT

NASA CR-1545

A STUDY TO DETERMINE THE FLIGHT CHARACTERISTICS AND HANDLING QUALITIES OF VARIABLE GEOMETRY SPACECRAFT

Volume I - High L/D Concept With Single Pivot Two-Position Skewed Wing

by B. J. Kuchta

Prepared by
GENERAL DYNAMICS CORPORATION
San Diego, Calif
for Langley Research Center

NATIONAL AERONAUTICS AND SPACE ADMINISTRATION • WASHINGTON, D. C. • APRIL 1970

A STUDY TO DETERMINE THE FLIGHT CHARACTERISTICS AND HANDLING QUALITIES OF VARIABLE GEOMETRY SPACECRAFT

Volume I - High L/D Concept With Single Pivot Two-Position Skewed Wing

By B. J. Kuchta

Issued by Originator as Report No. GDC-DDE68-003

Prepared under Contract No. NAS 1-7971 by
GENERAL DYNAMICS CORPORATION
San Diego, Calif.

for Langley Research Center

NATIONAL AERONAUTICS AND SPACE ADMINISTRATION

For sale by the Clearinghouse for Federal Scientific and Technical Information
Springfield, Virginia 22151 – CFSTI price $3.00

TABLE OF CONTENTS

LIST OF FIGURES

LIST OF FIGURES, Contd

LIST OF FIGURES, Contd

LIST OF FIGURES, Contd

LIST OF FIGURES, Contd

LIST OF TABLES

LIST OF SYMBOLS

a_1	Body lower surface semi width at Station X, ft
a_2	Body upper surface semi width at Station X, ft
b	Aerodynamic reference span, ft
C_D	Drag coefficient
C_L	Lift coefficient
$C_{1/2}$	Cycles to one-half amplitude
C_{ℓ_β}	Lateral stability parameter
C_m	Pitching moment coefficient
C_{n_β}	Directional stability parameter
C_p	Center of pressure
C_{Y_β}	Side force parameter
c	Wing chord, ft
c.g.	Center of gravity percent of actual body length
g	Gravity, 32.2 ft/sec^2
h	Height of body at Station X, ft
H	Altitude, ft
I_{xx}	Moment of inertia about X body axis, slug-ft^2
I_{xz}	Cross product of inertia, slug-ft^2
I_{yy}	Moment of inertia about Y body axis, slug-ft^2
I_{zz}	Moment of inertia about Z body axis, slug-ft^2
i_w	Wing incident angle

K	Constant
K_P	Roll rate gain
K_Q	Pitch rate gain
K_R	Yaw rate gain
L	Rolling moment, ft-lb
ℓ	Aerodynamic reference length, ft
M	Pitching moment, ft-lb
N	Yawing moment, ft-lb
n_z	Normal load factor, g
P, p	Rolling rate, rad/sec
P_s	Stability axis roll rate, rad/sec
$\bar{Q}$	Free stream dynamic pressure, psf
Q, q	Pitching rate, rad/sec
R, r	Yawing rate, rad/sec
R_s	Stability axis yaw rate, rad/sec
S	Aerodynamic reference area, ft^2
T_{θ_2}	Zero in pitch-elevator transfer function, sec
t	Time, sec
$t_{1/2}$	Time to one-half amplitude, sec
U_B	Body velocity along body X axis
V	Free stream velocity, ft/sec

V_B	Body velocity along body Y axis
W_B	Body velocity along body Z axis
X	Longitudinal distance along body, downrange, ft
X_s	Acceleration along the X stability axis, ft/sec^2
Y	Spanwise, ft
Y_s	Acceleration along the Y stability axis, ft/sec^2
y_u	Wing upper surface ordinate, ft
y_ℓ	Wing lower surface ordinate, ft
Z_s	Acceleration along the Z stability axis, ft/sec^2
α	Angle of attack, deg
β	Angle of side slip, deg
γ	Flight path angle, deg
δ_a	Aileron deflection, deg
δ_e	Elevator or elevon deflection, deg
δ_r	Rudder deflection, deg
ϵ	Downwash angle, deg
ζ	Relative damping factor
μ	Relative density factor
ρ	Air density, slug/ft^2
ϕ	Euler roll angle, deg
ψ	Euler yaw angle, deg

θ	Euler pitch angle, deg
$\Lambda_{C/2}$	Wing half chord sweep angle, positive counterclockwise, deg
Σ	Summation
$\partial(\,)/\partial(\,)$	Partial derivative
$\dot{(\,)}$	$\frac{d(\,)}{dt}$

Subscripts

BODY	Portion due to body
TAIL, HT	Portion due to horizontal tail
VT	Vertical tail (dorsal fins)
W	Portion due to wing
x	Longitudinal distance
z	Vertical distance
0	Conditions at zero angle of attack

SUMMARY

A study was conducted to determine the flight characteristics and wing deployment transients for a variable geometry logistics spacecraft concept having a hypersonic lift-drag ratio near 3.0, and employing a single-pivot, two-position skewed wing for deployment at subsonic speeds. Unpowered flight conditions are considered throughout the study. The body of the spacecraft is trapezoidal in cross section and horizontal stabilizers and dorsal fins are located near the base of the body to provide longitudinal and directional stability. A highly cambered moderate aspect ratio wing is stowed on top of the body during entry and is deployed at a subsonic speed at a Mach number of 0.60 at an altitude of 30,000 feet to a zero sweep condition.

Detailed static wind tunnel aerodynamic data obtained from low subsonic to hypersonic speeds were used to estimate the dynamic aerodynamic stability characteristics throughout the entire entry flight regime. The aerodynamic data is presented as total vehicle derivates with the wing stowed, and as wing increment derivates which are added to the stowed wing values. The wing increments are presented for wing sweep positions of 0°, 15°, 30°, 45°, 60°, and 75°, with the wing considered rotated counterclockwise during deployment. Extendable wing trailing edge flaps are incorporated in some instances to provide increased lift at landing. Flap incremental aerodynamic data are presented at 0°, 12°, and 20° of flap deflection.

The spacecraft concept studied is dynamically stable throughout the flight envelope, but stability augmentation is required to provide acceptable handling qualities with the vehicle center of gravity located at 65 percent of the actual body length. The stability augmentation recommended is of the simple rate feedback type with gain scheduling.

Wing deployment transients are minor and the piloting task during wing deployment consists of a simple push-over maneuver. However, maintaining the vehicle in a low angle of attack, near zero lift condition is recommended. Deployment rates of 2, 5, 10, 15, 20, 30 and 40 degrees per second were analyzed. A rate of 10 degrees per second appears to be near optimum.

For the unflapped wing configuration, landing characteristics of this spacecraft concept are comparable to present day high performance fighter aircraft. The approach speed is in the 160-170 knot range with

a 10° flight path angle. The flare is initiated between 200 and 250 feet in altitude, and flare load factor is approximately 0.2g. Little improvement in landing characteristics was obtained with the addition of wing trailing edge flaps. Therefore the added system complexity and weight introduced by wing flaps is not warranted.

A STUDY TO DETERMINE THE FLIGHT CHARACTERISTICS AND HANDLING QUALITIES OF VARIABLE GEOMETRY SPACECRAFT

By B. J. Kuchta

Convair Division of General Dynamics Corporation
San Diego, California

SECTION 1

INTRODUCTION

Considerable effort is at present being devoted to the development of lifting entry spacecraft concepts for use as possible logistics systems with lift-drag ratios varying from near 1.0 to in excess of 3.0. Recent studies related to the development of hypersonic lifting bodies, optimized with regard to improved aerodynamic performance, have shown that body shapes of moderate fineness ratios having relatively good volume to wetted area relationships (and hence, lower weight) can provide hypersonic lift-to-drag ratios of up to approximately 3.5.

For vehicles conceived to be piloted or flown in the conventional sense during the entire entry and to land in the manner of aircraft, aerodynamic features must be tailored for both hypersonic and low-subsonic flight. The moderate-to-high lift-to-drag ratio hypersonic lifting body vehicles have unacceptable subsonic performance for horizontal landing without modification or compromise to the basic shape. The incorporation of some form of deployable lifting surface offers a possible means of providing efficient subsonic land recovery, while retaining the desired hypersonic shape. If manned spaceflight is to become a routine operation, independent of massive sea recovery logistics, the desirability of landing at one of several preselected sites with a minimum of ground support requirements must become a reality.

The purpose of this investigation is to provide information by use of static wind tunnel data input into the simulator to study handling qualities and the overall dynamic stability and control, wing deployment characteristics, and landing characteristics of a spacecraft concept having a hypersonic lift-drag ratio of approximately 3.0. The spacecraft concept incorporates a two-position single-pivot wing, deployed to improve subsonic aerodynamic characteristics. To aid in the landing approach, wing trailing edge flaps with three deflection positions have also been examined.

The investigation incorporated both analytical analysis and simulation. The analytical analysis provided information as to handling qualities relative to both longitudinal and

lateral modes, period and damping. The simulation provided a vehicle by which a flight could be flown from 100,000 feet altitude, through wing deployment, to touchdown.

The results of the investigation are presented in the form of time histories, periods, damping, and time to damp to one-half amplitude of the longitudinal and lateral oscillations. Where possible, the results are discussed in terms of handling qualities parameters which are in current usage for proposed entry vehicle configurations and high performance aircraft.

The sign convention used is presented in Figure 1-1.

SECTION 2

VEHICLE DESCRIPTION

The spacecraft concept investigated has a body with a trapezoidal cross section and an area distribution conforming to that required to minimize zero-lift hypersonic wave drag as determined under the geometric constraints of length and volume.[1] The effective fineness ratio of the body is 6.0 with a volume to (length)^3 ratio of 0.0110. Horizontal stabilizers and dorsal fins are located near the base of the body to provide longitudinal and directional stability. A moderate aspect ratio wing having a thick, highly cambered airfoil section is stowed on top of the body during entry and is deployed at subsonic speeds to a zero sweep condition. Elevon controls are located on the horizontal stabilizers to provide longitudinal control, and roll control when differentially deflected. Rudder controls are located on the dorsal fins to provide directional control.

A drawing of the complete spacecraft is shown in Figure 2-1. Table 2-1 presents body ordinates normalized with respect to length and Table 2-2 presents wing airfoil section ordinates normalized with respect to chord. Figure 2-2 shows the details of the wing and tails.

The trapezoidal body has a top-to-bottom ratio of 1 to 3. The flat bottom offers advantages with regard to aerodynamic heating, and also provides improved lift at hypersonic speeds.[1]* Negative camber was incorporated in the body by placing 0.333 of the vertical height above and 0.667 of the vertical height below the vehicle reference plane at all longitudinal stations, to provide positive pitching moments near zero angle of attack at hypersonic speeds. The large blunt base was retained for efficient spacecraft-booster integration.

The wing panel is an approximately 18-percent thick, highly cambered, St. Cyr (Royer 156) airfoil section measured parallel to the airstream at zero degree sweep of the half chord. The wing taper ratio is 0.60 and its aspect ratio is 9.42 based on its own projected wing planform area. The projected planform area is 23.1 percent of the body planform area. The wing incidence angle is 4 degrees, relative to wing ordinate reference line. See Figure 2-2.

The horizontal stabilizers are located along the body lower surface ridge line just ahead of the base and are at zero degrees dihedral. The stabilizers, which are 2-degree (included angle) wedge airfoil sections, have a 65-degree leading edge sweep. The elevon control surfaces used for pitch and roll control are located at the trailing edge of the stabilizers. Total exposed horizontal stabilizer area including the elevons is 19.87 percent of the body planform area.

*All references are listed on Page 37.

Table 2-1. Design Body Ordinates

x/ℓ	$*a_1/\ell$	$**a_2/\ell$	h/ℓ
0	0	0	0
0.01	0.00503	0.00168	0.00591
0.02	0.00794	0.00265	0.00936
0.03	0.01090	0.00363	0.01287
0.04	0.01349	0.00450	0.01590
0.05	0.01592	0.00531	0.01876
0.06	0.01826	0.00609	0.02151
0.07	0.02050	0.00683	0.02415
0.08	0.02270	0.00757	0.02675
0.09	0.02476	0.00825	0.02919
0.10	0.02775	0.00925	0.03271
0.20	0.04475	0.01492	0.05274
0.30	0.05953	0.01984	0.07015
0.40	0.06737	0.02412	0.08529
0.50	0.08402	0.02801	0.09900
0.60	0.09408	0.03136	0.01108
0.70	0.10269	0.03423	0.12101
0.80	0.11007	0.03669	0.12970
0.90	0.11547	0.03849	0.13607
0.94	0.11695	0.03899	0.13782
0.96	0.11757	0.03919	0.13855
0.98	0.11807	0.03936	0.13914
1.00	0.11834	0.03945	0.13946

* Lower Surface Semiwidth
**Upper Surface Semiwidth

Table 2-2. Wing Ordinates

x/c	y_u/c	y_L/c
0.013	0.038	-0.027
0.025	0.052	-0.034
0.050	0.074	-0.040
0.075	0.091	-0.044
0.100	0.105	-0.044
0.150	0.127	-0.038
0.200	0.144	-0.030
0.300	0.163	-0.014
0.400	0.166	0.001
0.500	0.160	0.018
0.600	0.144	0.030
0.700	0.116	0.032
0.800	0.083	0.030
0.900	0.045	0.018
0.950	0.026	0.010
1.000	0	0

Dorsal fins are located on the sides of the body and are at 45 degrees dihedral angle as measured from the horizontal reference plane. The dorsal fins are geometrically identical to the horizontal stabilizers in planform. Rudders are located at the trailing edge for yaw control.

The sizing of the spacecraft concept being considered was performed in a study entitled Weight and Performance Characteristics of Variable-Geometry Spacecraft, which was conducted at Convair under contract NAS1-7675. The results of that study indicate that the spacecraft inertia characteristics with wing stowed should be:

Weight	20,000 lb
c.g.	0.65 ℓ
I_{xx}	9,840 slug-ft^2
I_{yy}	118,100 slug-ft^2
I_{zz}	117,146 slug-ft^2
I_{xz}	500 slug-ft^2

Reference dimensional data for reducing the aerodynamic characteristics to coefficient form are:

Length (ℓ)	50 feet
Span (b)	12 feet
Area (s) S	367 feet^2

All of the above data is used throughout the analysis and simulation.

SECTION 3

AERODYNAMIC DATA WITHOUT WING ($\Lambda = 90°$)

This section is a discussion of the aerodynamic characteristics with the wing fully stowed ($\Lambda = 90°$). Since the wing is only deployed at subsonic speed the only aerodynamic data which is influenced by Mach number is that without the wing. Static wind tunnel aerodynamic data were used in the form of linear tables with Mach number as the independent variable. In order to include the angle of attack non-linearities, first and second order partials of each aerodynamic derivative were derived from the measured wind tunnel data. A major effort was expended in the development of the aerodynamic data because any stability and control analysis or simulation of an aerodynamic vehicle is only as good as the aerodynamic data used.

The wind tunnel measured data consisted of static aerodynamic coefficients for the complete configuration, body alone, horizontal stabilizer-body and horizontal stabilizer-dorsal fins-body. With this type of breakdown the influence of each component could be derived. Since this study depended upon dynamic derivatives, a method was developed whereby dynamic derivatives could be obtained from the static component aerodynamic data and geometric considerations.

The wind tunnel test data were available at Mach numbers of 0.3, 0.5, 0.80, 0.90, 0.95, 1.00, 1.20, 2.30, 2.96, 3.96, 4.63, and 10.0. At each Mach number C_D, C_L, C_m, C_{Y_β}, C_{n_β} and C_{ℓ_β} were available as a function of angle of attack and several elevon deflections. The angle of attack range generally was from about -2 degrees to 18 degrees. Data was taken at 0°, -10°, -20° of elevon deflection.

Figures 3-1 through 3-37 present all of the reduced aerodynamic data as a function of Mach number. A brief discussion is given below on each coefficient presented. All moment coefficients are referenced to 62.8 percent of the longitudinal length (ℓ) and 0.0329ℓ below the spacecraft centerline. All forces and moments were transferred to the vehicle center of gravity located at 65 percent of the length for all computations of handling qualities parameters and flight characteristics. All static wind tunnel moment coefficients received from the NASA were presented about a moment reference point located at 62.8 percent of ℓ.

C_{D_0}

is the drag coefficient (C_D) at zero angle of attack and zero elevon deflection. It is obtained directly from the wind tunnel data.

$\frac{\partial C_D}{\partial \alpha^2}$

is the part of the overall drag coefficient which is a function of angle of attack squared. This coefficient was obtained by best fitting the equation

$$C_D = a_0 + a_2 \alpha^2 \tag{1}$$

through the wind tunnel drag data for zero elevon deflection. Then $\frac{\partial C_D}{\partial \alpha^2}$ is equal to the value of a_2 and C_{D_0} is equal to a_0. The $\frac{\partial C_D}{\partial \alpha^2}$ is in a sense a curve fit to simulate drag due to lift.

$\frac{\partial C_D}{\partial \delta_e^2}$

is the part of the overall drag coefficient which is a function of elevon deflection squared. The incremental drag due to elevon deflection was cross plotted versus elevon deflection at constant angle of attack and the equation

$$C_D = K\delta_e^2 \tag{2}$$

was best fitted to the points. It was found that K was relatively constant with angle of attack and, therefore, no variation of K with angle of attack was considered.

C_{L_0}

is the lift coefficient at zero angle of attack and zero elevon deflection. It is obtained directly from wind tunnel data.

C_{L_α}

is the linear portion of the lift versus angle of attack curve for zero elevon deflection. It is obtained by best fitting the equation

$$C_L = b_1 + b_2\alpha + b_3\alpha^2 \tag{3}$$

to the lift coefficient wind tunnel data. b_1 is set equal to C_{L_0}. Then b_2 equals C_{L_α} and b_3 equals $\frac{\partial C_L}{\partial \alpha^2}$.

$\frac{\partial C_L}{\partial \alpha^2}$

is the coefficient obtained from Equation 3, where b_3 equals $\frac{\partial C_L}{\partial \alpha^2}$. This coefficient is primarily the result of the body lift that is influenced by cross-flow at the higher angles of attack.

$C_{L_{\delta_e}}, \frac{\partial C_{L_{\delta_e}}}{\partial \alpha}$

is incremental lift due to elevon deflection. It is obtained by plotting the incremental elevon lift versus angle of attack and best fitting this wind tunnel data by the equation

$$\Delta C_{L_{\delta_e}} = C_0 + C_1 \alpha \tag{4}$$

Then C_0 is equal to $C_{L_{\delta_e}}$ and C_1 is equal to $\frac{\partial C_{L_{\delta_e}}}{\partial \alpha}$. From the data obtained the indication was that $C_{L_{\delta_e}}$ and $\frac{\partial C_{L_{\delta_e}}}{\partial \alpha}$ are constant to elevon deflections of 20° and were assumed constant to 25°. Beyond 25°, estimated surface effectiveness drops off rapidly. However, no attempt was made to include this effect into the program.

C_{L_q}

is the lift due to pitching velocity. This coefficient was obtained from the lift curve slope of the horizontal stabilizer, the body, and twin vertical fins. Figure 3-38 presents the incremental lift and moment for the horizontal stabilizer versus angle of attack for low speed. The data were obtained from the body alone lift and the body-horizontal stabilizer lift. The body damping was obtained from slender body theory with cross-flow.[2] The body angle of attack distribution was obtained from a unit pitch rotation velocity about the spacecraft center of gravity. Then C_{L_q} was obtained from the equation

$$C_{L_q} = -2\, C_{M_{HT}} + C_{L_{q_{BODY}}} \tag{5}$$

C_{m_q}

is pitching moment due to pitching velocity. This coefficient was computed in a manner similar to C_{L_q}. The equation used to compute the tail contribution was

$$C_{m_{q_{TAIL}}} = 2 \frac{\left(C_{M_{HT}}\right)^2}{C_{L_{HT}}} \tag{6}$$

Then

$$C_{m_q} = \left(C_{m_q}\right)_{TAIL} + \left(C_{m_q}\right)_{BODY} \tag{7}$$

C_{m_0}, C_{m_α}, $\frac{\partial C_{m_\alpha}}{\partial \alpha}$

are components of the pitching moment coefficient at zero elevon deflection. They are obtained by best fitting the equation

$$C_m = d_0 + d_1\alpha + d_2\alpha^2 \tag{8}$$

to wind tunnel data. Then C_{m_0} is equal to d_0, C_{m_α} is equal to d_1, and $\frac{\partial C_{m_\alpha}}{\partial \alpha}$ is equal to d_2. The non-linear term is composed mostly of body cross flow moment.

$C_{m_{\delta_e}}$, $\frac{\partial C_{m_{\delta_e}}}{\partial \alpha}$

are components of the pitching moment coefficient proportional to elevon deflection. They are obtained by best fitting the equation

$$C_m = e_0 + e_1\alpha \tag{9}$$

to wind tunnel data. Then $C_{m_{\delta_e}}$ is equal to e_0 and $\frac{\partial C_{m_{\delta_e}}}{\partial \alpha}$ is equal to e_1.

$C_{y_\beta}, \frac{\partial C_{y_\beta}}{\partial \alpha}$

is side force per side slip angle. It is obtained by best fitting the equation

$$C_{Y_\beta} = f_0 + f_1 \alpha \tag{10}$$

to wind tunnel data. Then f_0 equals C_{Y_β} and f_1 equals $\frac{\partial C_{Y_\beta}}{\partial \alpha}$.

C_{Y_P}

is the side force due to rolling velocity. The only aerodynamic components contributing to this coefficient are the dorsal fins. The incremental $(C_{Y_B})_{VT}$ side force from the dorsal fins was computed from wind tunnel data. Then

$$C_{Y_P} = +2 \left(C_{Y_\beta}\right)_{VT} (C_P)_{VT_Z} \tag{11}$$

where $(C_P)_{VT_Z}$ is the distance from the center of gravity to the center of pressure (see sketch).

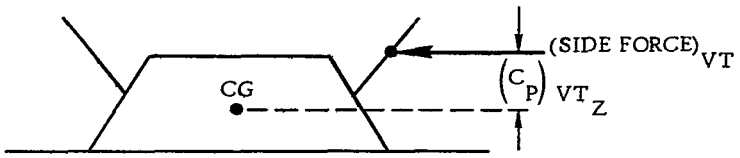

From wind tunnel data $(C_P)_{VT_Z}$ was computed to be approximately 0.46.

C_{Y_r}

is the side force due to yawing velocity. Contributors to this coefficient are the body and the dorsal fins. From the dorsal fins contribution, a computation similar to that for C_{Y_P} was made:

$$\left(C_{Y_r}\right)_{VT} = -2 (C_Y)_{VT} \times (C_P)_{VT_X} \tag{12}$$

From wind tunnel data $(C_{P'})_{VT_X}$ was computed to be approximately 1.25b. The body contribution was computed from slender body theory.[2] The side slip angle distribution used was for a unit yawing velocity. Then

$$C_{Y_r} = \left(C_{Y_r}\right)_{VT} + \left(C_{Y_r}\right)_{BODY} \tag{13}$$

$C_{Y_{\delta_r}}, \dfrac{\partial C_{Y_{\delta_r}}}{\partial \alpha}$

is the rudder side force coefficient. No wind tunnel measurements of this coefficient were made. Estimates of this coefficient were made by assuming the normal force coefficient of the rudder was equal to the elevon normal force coefficient. Geometrically the dorsal fins are identical to the two horizontal stabilizers. The rudder normal force was then resolved to a side force. The term $\dfrac{\partial C_{Y_{\delta_r}}}{\partial \alpha}$ was obtained from the elevon term $\dfrac{\partial C_{L_{\delta_e}}}{\partial \alpha}$.

$C_{n_\beta}, \dfrac{\partial C_{n_\beta}}{\partial \alpha}$

is yawing moment due to side slip angle. A best fit of

$$C_n = g_0 + g_1 \alpha \tag{14}$$

to wind tunnel data and C_{n_β} equals g_0 and $\dfrac{\partial C_{n_\beta}}{\partial \alpha}$ equals g_1.

C_{n_r}

is yawing moment due to yawing velocity. Contributors to this coefficient are the dorsal fins and the body. The dorsal fins contribution was determined from

$$\left(C_{n_r}\right)_{VT} = 2(C_{Y_\beta})_{VT} \times (CP)^2_{VT_X} \tag{15}$$

The body contribution was computed using slender body theory. Then

$$C_{n_r} = \left(C_{n_r}\right)_{VT} + \left(C_{n_r}\right)_{BODY} \tag{16}$$

C_{n_p}, $\dfrac{\partial C_{n_p}}{\partial \alpha}$

is yawing moment due to rolling velocity. The dorsal fins and the horizontal stabilizer contribute to this coefficient. The dorsal fins contribution was computed by the equation

$$C_{n_p} = \left(C_{n_p}\right)_{VT} = -2(C_{y_\beta})_{VT} \times (C_p)_{VT_X} \times (C_P)_{VT_Z} \tag{17}$$

where the center of pressures $(C_P)_{VT_X}$ and $(C_P)_{VT_Z}$ were computed from wind tunnel data. The horizontal stabilizer contribution is associated with the fore-and-aft inclination of the lift vector which depends on the leading-edge suction. For a supersonic leading-edge, the lift is normal to the surface and no horizontal stabilizer C_{n_p} is present (the incidence angle is zero). For the 65-degree leading-edge sweep of the horizontal stabilizer the leading-edge is subsonic for Mach numbers below 2.37. Then for Mach numbers less than 2.37

$$\frac{\partial C_{n_P}}{\partial \alpha} = \left(C_{n_P}\right)_{HT} = -2\left(C_{L_\alpha}\right)_{HT} \tag{18}$$

$C_{n_{\delta_a}}$

is yawing moment due to differential elevon deflection. It is obtained from wind tunnel data.

$C_{n_{\delta_r}}$, $\dfrac{\partial C_{n_{\delta_r}}}{\partial \alpha}$

are rudder yawing moment coefficients. They are obtained in the same manner that $C_{Y_{\delta_r}}$ and $\frac{\partial C_{Y_{\delta_r}}}{\partial \alpha}$ were obtained.

C_{ℓ_β}, $\frac{\partial C_{\ell_\beta}}{\partial \alpha}$

is rolling moment due to side slip. Obtained by best fitting

$$C_\ell = h_0 + h_1 \alpha \tag{19}$$

to wind tunnel data. Then C_{ℓ_β} equals h_0 and $\frac{\partial C_{\ell_\beta}}{\partial \alpha}$ equals h_1.

C_{ℓ_r}

is rolling moment due to yawing velocity. It is computed by the equation

$$C_{\ell_r} = \left(2\, C_{Y_\beta}\right)_{VT} \times (C_P)_{VT_X} \times (C_P)_{VT_Z} \tag{20}$$

where $\left(C_{Y_\beta}\right)_{VT}$, $(C_P)_{VT_X}$, and $(C_P)_{VT_Z}$ were obtained from wind tunnel data. The dorsal fins were considered to be the only contributor to this coefficient.

C_{ℓ_P}

is rolling moment due to rolling velocity. Both the horizontal stabilizer and the dorsal fins contribute to this coefficient. If an elliptical spanwise loading distribution is assumed, an expression for roll damping is

$$\left(C_{\ell_P}\right)_{HT} = 0.1 \left(C_{L_\alpha}\right)_{HT} \tag{21}$$

Then

$$C_{\ell_P} = 0.1\left[\left(C_{L_\alpha}\right)_{HT} + \left(C_{L_\alpha}\right)_{VT}\right] \tag{22}$$

Wind tunnel data were used to compute $\left(C_{L_\alpha}\right)_{HT}$ and $\left(C_{L_\alpha}\right)_{VT}$.

$C_{\ell_{\delta_a}}$, $\dfrac{\partial C_{\ell_{\delta_a}}}{\partial \alpha}$

are rolling moment coefficients due to differential elevon deflection. They are obtained from best fitting the equation

$$C_{\ell_{\delta_a}} = k_0 + k_1 \alpha \tag{23}$$

to wind tunnel data. Then $C_{\ell_{\delta_a}}$ is equal to k_0 and $\dfrac{\partial C_{\ell_{\delta_a}}}{\partial \alpha}$ is equal to k_1.

$C_{\ell_{\delta_r}}$, $\dfrac{\partial C_{\ell_{\delta_r}}}{\partial \alpha}$

are rolling moment coefficients due to rudder deflection. They are obtained from the computed $C_{Y_{\delta_r}}$ and $\dfrac{\partial C_{Y_{\delta_r}}}{\partial \alpha}$ coefficients by the following equation.

$$C_{\ell_{\delta_r}} = C_{Y_{\delta_r}} \times \left(C_{P_{\delta_r}}\right)_Z \tag{24}$$

The value of $\left(C_{P_{\delta_r}}\right)_Z$ was assumed to be equal to 0.4b for all Mach numbers.

At a given Mach number all of the above discussed non-dimensionalized coefficients are evaluated. Since what is needed for the six-degree-of-freedom equations of

motion are six non-dimensionalized coefficients, the following equations present the combining equations.

$$C_D = C_{D_0} + \frac{\partial C_D}{\partial \alpha^2} \alpha^2 + \frac{\partial C_D}{\partial \delta_e^2} \delta_e^2 \tag{25}$$

$$C_L = C_{L_0} + C_{L_\alpha} \alpha + \frac{\partial C_{L_\alpha}}{\partial \alpha} \alpha^2 + C_{L_{\delta_e}} \delta_e + \frac{\partial C_{L_{\delta_e}}}{\partial \alpha} \alpha \delta_e + C_{L_q} \frac{\ell}{2V} q \tag{26}$$

$$C_m = C_{m_0} + C_{m_\alpha} \alpha + \frac{\partial C_{m_\alpha}}{\partial \alpha} \alpha^2 + C_{m_{\delta_e}} \delta_e + \frac{\partial C_{m_{\delta_e}}}{\partial \alpha} \alpha \delta_e + C_{m_q} \frac{\ell}{2V} q \tag{27}$$

$$C_Y = C_{Y_\beta} \beta + \frac{\partial C_{Y_\beta}}{\partial \alpha} \alpha \beta + C_{Y_r} \frac{b}{2V} r + C_{Y_p} \frac{b}{2V} p + C_{Y_{\delta_r}} \delta_r + \frac{\partial C_{Y_{\delta_r}}}{\partial \alpha} \alpha \delta_r \tag{28}$$

$$C_n = C_{n_\beta} \beta + \frac{\partial C_{n_\beta}}{\partial \alpha} \alpha \beta + C_{n_r} \frac{b}{2V} r + C_{n_p} \frac{b}{2V} p + \frac{\partial C_{n_p}}{\partial \alpha} \alpha \frac{b}{2V} p + C_{n_{\delta_r}} \delta_r$$

$$+ \frac{\partial C_{n_{\delta_r}}}{\partial \alpha} \alpha \delta_r + C_{n_{\delta_a}} \delta_a \tag{29}$$

$$C_\ell = C_{\ell_\beta} \beta + \frac{\partial C_{\ell_\beta}}{\partial \alpha} \alpha \beta + C_{\ell_r} \frac{b}{2V} r + C_{\ell_p} \frac{b}{2V} p + C_{\ell_{\delta_a}} \delta_a + \frac{\partial C_{\ell_{\delta_a}}}{\partial \alpha} \alpha \delta_a$$

$$+ C_{\ell_{\delta_r}} \delta_r + \frac{\partial C_{\ell_{\delta_r}}}{\partial \alpha} \alpha \delta_r \tag{30}$$

SECTION 4

AERODYNAMIC EFFECTS OF THE WING

In order to improve the subsonic characteristic of the spacecraft concept, a single pivot skewed wing is deployed at low speeds. The altitude and Mach number for deployment are to be determined in this study. Low speed wind tunnel tests were conducted at a Mach number of 0.30. Since tests were made with and without the wing, downwash on the tail surfaces induced by the wing was determined directly from wind tunnel data.

The wind tunnel aerodynamic data were reduced in a manner which allows the wing effects to be considered as increments which, when the wing is deployed, are algebraically added to the spacecraft without wing data. With regard to the simulator, this method of data handling simplifies the generation of the aerodynamic coefficients during wing deployment and thereafter.

Figures 4-1 through 4-11 present the wing incremental aerodynamic data as a function of angle of attack and wing sweep angle. Wind tunnel tests were conducted at 0°, 15°, 30°, 45°, 60°, and 75° of wing sweep.

ΔC_L, ΔC_D, ΔC_m

are the incremental lift, drag, and pitching moment coefficients for the spacecraft with the wing at the indicated sweep position obtained by subtracting the body-alone lift. The wing flaps are stowed.

$C_{L_{\dot{\alpha}}}$, $C_{m_{\dot{\alpha}}}$

are the lift and pitching moments due to pitching velocity. These coefficients are computed from the equations

$$C_{L_q} = -2\left(C_{L_\alpha}\right)_{HT} \times \frac{\partial \epsilon}{\partial \alpha} \times \left(C_p\right)_{HT_X} \tag{31}$$

$$C_{m_{\dot{\alpha}}} = C_{L_{\dot{\alpha}}} \times \left(C_p\right)_{HT_X} \tag{32}$$

Figure 4-12 presents the downwash (ϵ) as a function of angle of attack and wing sweep position. These coefficients are based on the concept of the lag of the downwash. Since the vorticity is convected with the stream, a change in the circulation at the wing will not be felt as a change in downwash at the tail until a time

$$\Delta t = \frac{(CP)_{HT_X}}{V} \tag{33}$$

has elapsed.

ΔC_{Y_β}, ΔC_{n_β}, ΔC_{ℓ_β}

are incremental side force, yawing moment, and rolling moment due to side slip for the wing. They are obtained directly from wind tunnel data for tests conducted at $\beta = 0$, and $\pm 5° \beta$.

ΔC_{ℓ_p}

is wing rolling moment due to rolling velocity. It is computed by assuming an elliptical spanwise loading on the wing. Then

$$\Delta C_{\ell_p} = -0.10\ C_{L_\alpha} \tag{34}$$

based on wing span.

From wind tunnel data the wing lift curve slope C_{L_α} is equal to 0.013 1/deg. Then for 0° C_{ℓ_p} equals -0.435 based on spacecraft area and span. From Reference 3 C_{ℓ_p} equals -0.64 correct to spacecraft area and span.

This same reference predicts a lift-curve slope C_L equal to 0.0205 (corrected to spacecraft area and span) which is a factor of 1.57 higher than the measure C_{L_α}.

ΔC_{ℓ_r}

is wing rolling moment due to yawing velocity. From Reference 3 $\frac{C_{\ell_r}}{C_L}$ equals 0.26 based on wing area and span. From wind tunnel data for wing at zero sweep angle

$$C_L = 0.17 + 0.013\alpha \tag{35}$$

Therefore correcting C_{ℓ_r}/C_L to spacecraft area and span

$$\Delta C_{\ell_r} = 0.06 + 0.0046\,\alpha \tag{36}$$

ΔC_{n_p}

is wing yawing moment due to rolling velocity. The wing contribution is in two parts. The first comes from the change in profile drag associated with the change in wing angle of attack. The increase in drag on the right wing accompanied by a decrease on the left wing produces a positive yawing moment equal to

$$\Delta C_{n_p}^{(1)} = \Delta C_D \left(\frac{Y}{b}\right) \tag{37}$$

From the below sketch, Y is the effective drag center of action and is equal to approximately 0.45b.

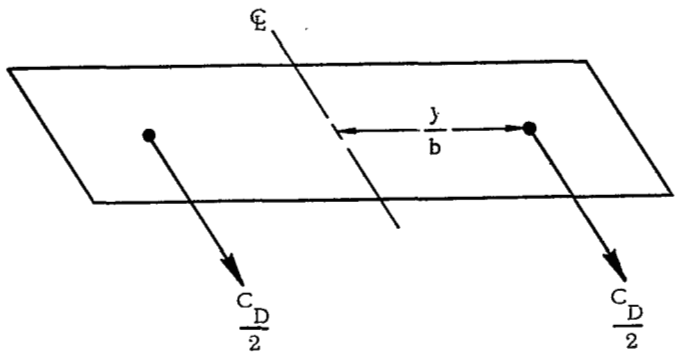

From test data at 0° half chord sweep angle

$$\Delta C_{D_W} = 0.0021\alpha \tag{38}$$

Then

$$\Delta C_{n_p}^{(1)} = 0.01\alpha \tag{39}$$

The second contribution to wing C_{n_p} is associated with the fore-and-aft inclination of the lift vector which depends on the leading edge suction. From the above sketch

$$\Delta C_{n_p}^{(2)} = -\left(\frac{Y}{b}\right)^2 C_L \tag{40}$$

Substituting Equation 36 and the value of y into Equation 40 leads to

$$\Delta C_{n_p}^{(2)} = -(0.82 + 0.063\alpha) \tag{41}$$

For zero degree sweep angle

$$\Delta C_{n_p} = C_{n_p}^{(1)} + C_{n_p}^{(2)} \tag{42}$$

The total coefficients for the spacecraft plus wing are

$$\begin{aligned}
C_D &= C_D + \Delta C_{D_w} \\
C_L &= C_L + \Delta C_{L_w} \\
C_m &= C_m + \Delta C_{m_w} \\
C_y &= C_y + \Delta C_{y_w} \\
C_n &= C_n + \Delta C_{n_w} + \Delta C_{n_{p_w}} p \\
C_\ell &= C_\ell + \Delta C_{\ell_\beta} \beta + \Delta C_{\ell_{r_w}} r + \Delta C_{\ell_{p_w}} p
\end{aligned} \tag{43}$$

The spacecraft concept being investigated has been also considered with wing trailing-edge flaps which can be deployed to 0°, 12°, and 20°. Figure 4-13 presents the wing-flap configuration, and deflections investigated. The incremental ΔC_L, ΔC_D, and ΔC_m obtained from wind tunnel data as a function of angle of attack for the flap deployed configuration is presented in Figures 4-14, 4-15, and 4-16 respectively. The flap increments are added to the flaps-off data.

SECTION 5

SIMULATION EQUATIONS

The following equations represent six degree-of-freedom equations of motion about a system of body oriented axes. The aerodynamic coefficients used in the equations are those described in Section 4 of this report. The force equations are wind-axis oriented and the moment equations are body-axis oriented.

The velocity equation is

$$\dot{V} = X_s \cos\beta + Y_s \sin\beta \tag{44}$$

The angle of attack equation is

$$\dot{\alpha} = Q + \frac{\left(\frac{Z_S}{V} - P_s \sin\beta\right)}{\cos\beta} \tag{45}$$

where

$$P_s = P \cos\alpha + R \sin\alpha \tag{46}$$

The side-slip angle equation is

$$\dot{\beta} = \frac{(Y_s \cos\beta - X_s \sin\beta)}{V} - R_s \tag{47}$$

where

$$R_s = R \cos\alpha - P \sin\alpha \tag{48}$$

The force equations are

$$X_s = g_{x_B} \cos\alpha + g_{z_B} \sin\alpha - C_D \bar{Q} \left(\frac{S}{m}\right) \tag{49}$$

$$Y_s = g_{y_B} + C_Y \bar{Q} \frac{S}{m} \tag{50}$$

$$Z_s = g_{z_B} \cos\alpha - g_{x_B} \sin\alpha - C_L \bar{Q} \left(\frac{S}{m}\right) \tag{51}$$

The body gravity components are

$$g_{x_B} = -g \sin\theta \tag{52}$$

$$g_{y_B} = g \cos\theta \sin\phi \tag{53}$$

$$g_{z_B} = g \cos\theta \cos\phi \tag{54}$$

Altitude and ground track computations are made by resolving the total velocity V into body-axis components by the equations

$$U_B = V \cos\alpha \cos\beta \tag{55}$$

$$W_B = V \cos\beta \sin\alpha \tag{56}$$

$$V_B = V \sin\beta \tag{57}$$

Then the body-axis velocities are resolved to the inertial axes by the Euler angles as

$$\dot{H} = U_B \sin\theta - V_B \sin\phi \cos\theta - W_B \cos\phi \cos\theta \tag{58}$$

$$\dot{X} = U_B \cos\theta \cos\psi + V_B (\sin\phi \sin\theta \cos\psi - \cos\phi \sin\psi) + W_B (\cos\phi \sin\theta \cos\psi + \sin\phi \sin\psi) \tag{59}$$

$$\dot{Y} = U_B \cos\theta \sin\psi + V_B (\sin\phi \sin\theta \sin\psi + \cos\phi \cos\psi) + W_B (\cos\phi \sin\theta \sin\psi - \sin\phi \cos\psi) \tag{60}$$

The dynamic pressure equation is

$$\bar{Q} = \frac{1}{2} \rho V^2 \tag{61}$$

where the density (ρ) is a direct table look-up from Reference 4 data.

The rotational equations of motion are written in the body axis system.

The pitch equation is

$$\dot{Q} = \frac{\Sigma M}{I_{yy}} + \frac{I_{xz}}{I_{yy}} (R^2 - P^2) - \frac{(I_{zz} - I_{xx})}{I_{yy}} P R \tag{62}$$

The roll equation is

$$\dot{P} = \frac{\Sigma L}{I_{xx}} + \frac{I_{xz}}{I_{xx}} \dot{R} - \frac{(I_{zz} - I_{yy})}{I_{xx}} QR + \frac{I_{xz}}{I_{xx}} PQ \tag{63}$$

The yaw equation is

$$\dot{R} = \frac{\Sigma N}{I_{zz}} + \frac{I_{xz}}{I_{zz}} \dot{P} - \frac{(I_{yy} - I_{xx})}{I_{zz}} PQ - \frac{I_{xz}}{I_{zz}} QR \tag{64}$$

The body rates are used to compute the Euler angles by the equations

$$\dot{\theta} = Q \cos \phi - R \sin \phi \tag{65}$$

$$\dot{\phi} = P + \dot{\psi} \sin \theta \tag{66}$$

$$\dot{\psi} = \frac{(R \cos \phi + Q \sin \phi)}{\cos \theta} \tag{67}$$

Control of the spacecraft is accomplished by the deflection of elevons and rudders. Roll control is achieved by differentially deflecting the elevons. The roll controller ailerons) is computed by

$$\delta_a = \delta_{e_{left}} - \delta_{e_{right}} \tag{68}$$

he total surface deflections are

$$\delta_e = \delta_{e_P} + K_Q Q \tag{69}$$

$$\delta_r = \delta_{r_P} + K_R R + K_{\delta_a} \delta_a \tag{70}$$

$$\delta_a = \delta_{a_p} + K_p p \tag{71}$$

The limits placed on the surface deflections are

$$|\delta_e| \leq 25° \tag{72}$$

$$|\delta_a| \leq 10° \tag{73}$$

$$|\delta_r| \leq 25° \tag{74}$$

The moment equations are

$$\Sigma L = C_\ell \bar{Q} S b \tag{75}$$

$$\Sigma M = C_m \bar{Q} S \ell \tag{76}$$

$$\Sigma N = C_n \bar{Q} S b \tag{77}$$

The expansion for C_ℓ, C_m, and C_n is presented on page 16.

SECTION 6

HYBRID SIMULATION

A hybrid simulation of the spacecraft concept was programmed using the equations and data discussed in Sections 4 and 5. The hybrid simulation provides a computational tool for application that lies somewhere between a pure digital and a pure analog simulation. The diagram presented below is a schematic of the overall simulation. The digital computer portion of the hybrid computer provided a function generator and storage device for all of the detailed aerodynamic data.

Equations 44 through 60 and 75 through 77 were programmed on the digital computer in Fortran II. These equations were numerically integrated and the integration scheme included terms to compensate for phase-lag due to the sampling time. The overall digital computer cycle time was 0.06 second, which not only included the solution to the indicated differential equations but also the generation of the aerodynamic data for the analog computer.

Equations 62 through 74 were programmed on the analog computer. The analog computer was the device used to link the visual display and the cockpit to the overall simulation. Approximately three-quarters of the available equipment on a Comcor CI-5000 analog computer was used.

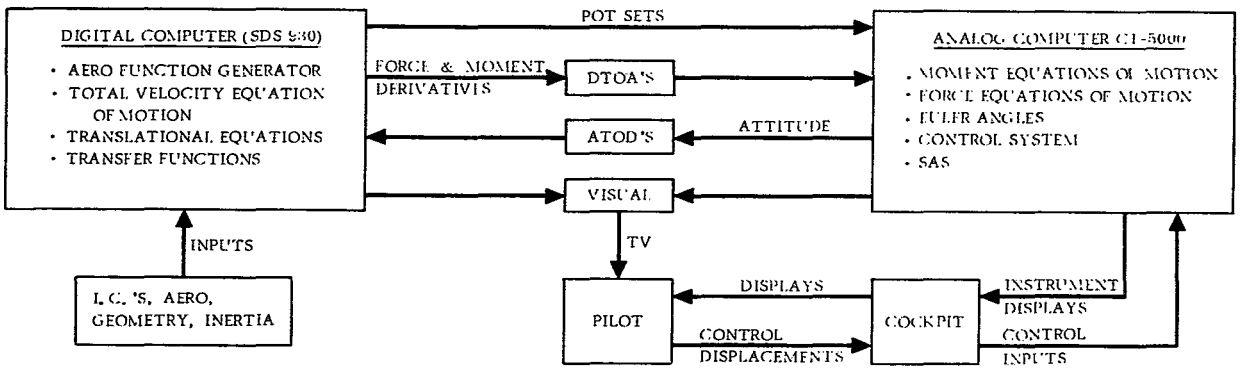

Schematic of Hybrid Computer Simulation

SECTION 7

RESULTS

7.1 OVERALL TRAJECTORIES

Early trajectories were flown on the simulator starting at an altitude of 100,000 feet and initial Mach numbers of 3, 4, and 5. The piloting task was to fly a given flight path angle profile. The profiles consisted of a constant flight path angle to wing deployment and then transition to a new flight path angle which was held to landing site acquisition. Figure 7-1 presents spacial histories for the various simulated flights. All of the flights were flown with the stability augmentation system that is discussed later in this section.

With an initial Mach number of 5 at 100,000 feet, this spacecraft is capable of flying constant flight paths of from 5 to 7 degrees. At flight paths below 5 degrees, the velocity dropoff was too large and the trim angle of attack required was beyond the trim capability of the vehicle control system. For flight path angles greater than 7 degrees, the speed dropoff is not great enough and therefore the vehicle's velocity between 25,000 and 30,000 feet was well above the subsonic value desired for wing deployment. The flight path range for an initial Mach number of 4 was 6 to 8 degrees; for an initial Mach number of 3 it was 10 to 12 degrees.

Figures 7-2 through 7-4 present the time histories of various parameters for flight with initial Mach numbers of 5, 4, and 3, respectively. Summaries of the trim angle of attack and elevator requirements for the range of altitudes and velocities of interest are presented in Figures 7-5 and 7-6.

7.2 WING DEPLOYMENT

Since this spacecraft concept employs a single pivot, two-position skewed wing, it is felt that to minimize wing deployment transients which would be produced by transonic shocks and aerodynamic flow, the wing should be deployed below the transonic speed regime. However, the wing deployment should occur at an altitude and distance from the landing sufficient enough to allow cross-range and down range errors to be nulled out by the high maneuverability allowed with wing deployed L/D. Results of the present study indicate that for the single pivot, two position wing concept, the best speed for wing deployment is at a Mach number of approximately 0.60.

At this Mach number shock effects and flow interference are minimum and, therefore, a minimum of dynamic transient will occur. This Mach number occurs at approximately 30,000 feet in altitude for the flight path profiles presented earlier. This speed and altitude allows sufficient time and maneuvering capability for landing site acquisition.

During wing deployment, the vehicle experiences a pitch-up due to a forward shift of the center of pressure and an increase in the overall lift coefficient. To reduce the lift and to add a nose-down moment, the pilot does a push-over maneuver. The piloting objective during wing deployment is to maintain a constant flight path angle. Figure 7-7 along with Table 7-1 present the wing deployment sequence for the pilot performing a push-over maneuver. The wing was swept at 10 degrees per second. Figure 7-8 presents the same data for a flight during which the pilot does not perform a push-over maneuver.

Without a push-over maneuver, the sink rate reduces to zero and the vehicle begins to climb due to the increase in lift. As the vehicle climbs, the velocity drops off in the exchange of kinetic energy for potential energy. The flight path oscillation, being only lightly damped, persists for several minutes. If the oscillation were uncontrolled it would be intolerable to the spacecraft crew.

Wing deployment rates of 2, 5, 10, 15, 20, 25, 30, and 40 degrees per second were simulated. For each case the pilot did a push-over maneuver. Figures 7-9, 7-10 and 7-11 present time histories for 2, 20, and 40 degree per second deployment rates

Table 7-1. Wing Deployment Sequence

Wing Deployment Rate	To γ = 8 deg				To γ = 10 deg			
	ΔV (ft/sec)	Δt (sec)	$\dot{\delta}_e$ (deg/sec)	Δh (ft)	ΔV (ft/sec)	Δt (sec)	Δh (ft)	Max γ Excursion (deg)
2 deg/sec	90	45	0.7	4500	Λ at 10° before end of wing deployment			0
5 deg/sec	65	18	2	1500	70	32	2700	1.5
10 deg/sec±	40	9	4	1000	48	18	1700	3
15 deg/sec	35	6	7	1000	40	16	1500	1.5
20 deg/sec	30	4.5	8	700	38	7	1000	1
25 deg/sec	15	3.6	10	500	30	12	1000	2.5
30 deg/sec	7	3	70	200	40	14	1500	5.5
40 deg/sec	7	2.25	10	200	30	14	1000	6.5

Note: Deployment starts at 30,000 feet
M = 0.65

respectively. Figure 7-12 presents a summary of average elevator deflection rates required during wing deployment and flight path deviations versus wing deployment rates. As wing deployment rates increase, elevator deflection rates increase to compensate for the trim and angle of attack changes, but beyond 30 deg/sec wing rate the response of the vehicle is slow enough that elevator rates of greater than 10 to 11 deg/sec are not required. Much more precise flight path control can be obtained by programming the elevator to wing sweep position. A possible elevon program is:

If

$$|\dot{\Lambda}| > 0$$

then

$$\dot{\delta}_e = 0.4\,\dot{\Lambda}$$

7.3 LANDING CHARACTERISTICS

The landing characteristics of this spacecraft concept were analyzed by flying piloted simulated landings with the hybrid computer and visual display. A time history of a landing without flaps is presented in Figure 7-13. An approach speed of 190 knots and 10-degree flight path angle was flown and an average incremental load factor of 0.2 g was maintained throughout flare. The landing speed without flaps is approximately 165 knots, and the flare initiation altitude is approximately 275 feet. At this speed, sufficient elevon deflection is available for roll control or additional pitch maneuvering. Figure 7-14 summarizes the landing characteristics without flaps by presenting flare load factor, flare initiation altitude and end of flare speeds versus approach speed for a 10-degree flight path angle. A 10-degree flight path angle was chosen because it is the approximate equilibrium glide angle for speeds of from 170 to 200 knots. Figure 7-15 presents the equilibrium glide angle versus speed for no flaps and various flap deflections. Figures 7-16 and 7-17 present trim angle of attack and elevon deflection versus speed for spacecraft configurations with and without flaps.

A piloted simulated landing with a flap deflection of 12 degrees is presented in Figure 7-18. An approach speed of 190 knots at the minimum flight path angle of 11.3 degrees was flown and an average incremental load factor of 0.4 g was maintained throughout flare. The end of flare speed was 165 knots. The flare was initiated at 230 feet altitude. A summary of the landing characteristics with 12-degree flaps is presented in Figure 7-19. Little improvement in landing characteristics was obtained with the addition of wing trailing-edge flaps. With flaps the flare initiation altitude decreases, the approach glide flight path angle increases, and the flare load factor is increased by a factor of two. It appears that the performance gains of wing trailing-edge flaps are small compared to the added system weight and complexities.

7.4 HANDLING QUALITIES - UNAUGMENTED

7.4.1 LONGITUDINAL. The handling qualities of this spacecraft concept have been analyzed in terms of existing military specifications for handling qualities of piloted airplanes, although it is realized that in some areas these criteria may not be directly applicable to piloted entry vehicles. For comparison purposes, some of the results of the investigation have also been analyzed in terms of several proposed criteria for piloted entry vehicles[5].

The results of the three-degree-of-freedom small perturbation calculation for wing stowed and wing deployed configurations are presented in Figures 7-20 and 7-21 respectively. These calculations were made at various speeds and altitudes. The damping results are presented in terms of the time factor $t_{1/2}$ since decreasing values of $t_{1/2}$ correspond to increasing values of damping. The data show that the configuration was stable for all conditions investigated. As expected, increasing altitude reduced the damping because such changes increased the relative density factor.

Presented in Figures 7-22 and 7-23 are the damping results for wing stowed and wing deployed together with the military specification of flying qualities for piloted airplanes, respectively[6]. The boundary shown in this figure specifies the minimum value of inverse cyclic damping ($1/C_{\frac{1}{2}}$) required for satisfactory damping of the short period mode of motion. The calculated data points for the basic (unaugmented) vehicle are below this boundary, an indication that the vehicle would have unsatisfactory longitudinal handling qualities. However, with the addition of artificial damping in pitch as shown in Section 7.5, the damping is easily increased enough to move all the calculated points above the specified boundary.

For the past few years, considerable effort has been directed toward more specific longitudinal handling qualities requirements than those given in Reference 5. Extensive work has been done with variable stability airplanes wherein the stick force characteristics were kept unaltered and the aerodynamics were artifically varied. The studies gave qualitative information in the form of pilot opinion and quantitative information in the form of time histories. An example of the handling qualities information derived in these studies is given in Figure 7-24[6]. Presented in this figure is a plot of undamped natural frequency f_n as a function of the short period damping ratio, ζ, together with flying qualities boundaries specified by the solid lines. Note that the results of this figure are in agreement with those of Figure 7-22 in that the basic vehicle is deficient in damping. Also, the addition of artificial damping in pitch (see Section 7.5) yields acceptable handling qualities.

Another dynamic characteristic which appears to play a role in the evaluation of the handling qualities and land characteristics is $1/T_{\theta_2}$. The smaller the value of $1/T_{\theta_2}$, the greater the accident rate. Figure 7-25 presents the accumulated accident data

and the value of $1/T_{\theta_2}$ for this spacecraft concept versus speed. The lower the value of $1/T_{\theta_2}$, the greater the overshoot following a change in elevator position. Thus, there is more difficulty in performing landing site acquisition or constant load factor flare.

Figure 7-26 presents the motion following an abrupt change in elevator position for several points along the flight corridor. The motion is oscillatory, which is apparently due to the low damping of the short-period mode previously discussed. Results of the simulator studies indicate that this type of oscillatory response to elevator control is very objectionable to the pilot.

7.4.2 LATERAL – DIRECTIONAL. Figures 7-27 and 7-28 present the period and damping characteristics of the lateral modes of motion for wing stowed and wing deployed, respectively. These computations are for several altitudes and speeds. Increasing altitude decreases Dutch roll damping, and increasing speed increases Dutch roll damping. The spiral mode is slightly unstable at the high dynamic pressures. The spiral mode motion may be thought of as a banked turn of gradually increasing radius. When this mode is unstable then with increasing time the flight of the airplane is in a banked turn of ever-decreasing radius. For the instabilities encountered in this vehicle the pilot has no problem in maintaining the proper heading.

Figure 7-29 presents the damping characteristics of the vehicle for wing stowed and deployed in terms of the military specification for flying qualities of piloted airplanes[6]. This figure presents a plot of the inverse cyclic damping ($1/C_{\frac{1}{2}}$) as a function of the roll-side velocity ratio $|\phi| / |V_e|$. The upper boundary in this plot specifies the value of $1/C_{\frac{1}{2}}$ required for satisfactory Dutch roll damping. The results show unsatisfactory Dutch roll characteristics at all points in the flight envelope. However, these characteristics can be improved to an acceptable level by increasing the roll damping and yaw damping artificially. The artificially damped condition will be presented in a later section.

The results of time-history motion studies to determine the lateral damping characteristics of the vehicle are presented in Figures 7-30 through 7-32. A step aileron deflection of 10 degrees was used to start a lateral oscillation and to obtain steady-state roll rates. The results substantiated the period and damping characteristics presented earlier.

At low speeds the vehicle has positive side slip (adverse) due to the low negative side force and low positive yawing moment produced by the rolling velocity and the relatively larger positive side force produced by bank angle. At high speeds, both with wings-in and wings-out, the side slip is negative (favorable) due to the high negative side force and high positive yawing moment produced by the rolling velocity. Positive values of side slip produce rolling moments which oppose the rolling motion through the effective dihedral parameter, C_{ℓ_β}.

For evaluating the roll performance of airplanes, the nondimensional rolling parameter, pb/2 V, is conventionally used. Figure 7-33 presents this parameter for various altitude and speeds throughout the vehicle's flight corridor. The roll requirements for fighter type aircraft (pb/2 V = 0.07) are based on present military handling qualities requirements. The data shows this spacecraft concept to have values of pb/2 V which are considerably below the required value for satisfactory roll response. Although the vehicle is deficient in roll response with regard to this parameter, recent flight tests of the M2/F2 and HL-10, both of which are deficient in this parameter, have shown that pilot ratings and military specifications do not appear compatible. Pilots that flew the simulation of this vehicle rate the rolling performance of this spacecraft concept as adequate. Recent work by NASA which uses a ground simulator appears to agree with the pilots who have flown the simulation of this spacecraft concept.[6] A proposed revision to the pb/2 V criterion specifies that in the landing approach condition the vehicle shall be capable of 30° of roll in 1 second after an initiation of an abrupt aileron deflection. In addition, the time required for the rolling velocity to reach 63 percent of the steady-state rolling velocity shall not be greater than 2 seconds. This spacecraft concept meets both of these requirements.

The roll performance of the vehicle in terms of the revised interim can be seen in Figure 7-30. The vehicle reached 63 percent of the steady-state rolling velocity in 0.7 second and a bank angle of 33° in 1 second. At faster approach speeds there is an improvement in this parameter due to the low trim angle of attack. This low angle reduces the adverse side-slip produced by rolling velocity at the lowest approach speeds that might be flown in this spacecraft concept. This parameter deteriorates to 1 second to reach 63 percent steady-state roll rate and a bank angle of 25° in 1 second. However, pilots on the simulator still considered this to be adequate.

The calculated lateral response of the vehicle following a step rudder input is presented in Figures 7-34 and 7-35. In summary, side-slip angle, bank angle, rolling velocity, and yawing rate reached in 1 second following a step rudder are: 0.5 degree, 1.0 degree, 1.2 degree per second, 0.6 degree per second, respectively. The initial roll rates and roll angles produced by rudder deflection are adverse. This is due to the positive $C_{\ell_{\delta_r}}$ and the high value of the parameter I_z/I_x. Rolling motions such as these result in a time lag between the pilot control input and the desired rolling motion which might lead to pilot-induced oscillation. However, throughout the flight corridor of this spacecraft concept, if the pilot flew with no rudder control input no pilot induced oscillations were produced.

Proposed revisions to the lateral handling qualities requirements include the parameter $(\omega_\phi/\omega_d)^2$. A value of $(\omega_\phi/\omega_d)^2$ of 1.0 corresponds to a steady-state rolling velocity equivalent to that given by a one-degree-of-freedom rolling analysis. Values of (ω_ϕ/ω_d) less than 1.0 indicate a steady-state rolling velocity less than that of the simplified analysis. Such a condition is generally associated with aileron adverse yaw.

Values of $(\omega_\phi/\omega_d)^2$ less than 0 indicate rolling reversal; that is, the vehicle will reach a steady-state rolling velocity opposite in direction to that desired. In order to have satisfactory flight ratings (pilot ratings of 3 or less) the (ω_ϕ/ω_d) parameter should be in the range of from about 0.8 to 1.1. Figure 7-36 presents values of (ω_ϕ/ω_d) versus Mach number and altitude. The results indicate that this spacecraft concept will have adequate lateral characteristics.

7.5 STABILITY AUGMENTATION SYSTEM

The need for a stability augmentation system is evident from the low short-period longitudinal damping and the low Dutch roll damping. This type of deficiency suggests that a simple rate feedback system, possibly gain scheduled with Mach number, would provide improvements to the handling qualities of this spacecraft concept which would render them adequate throughout the entire flight envelope.

A system of this type can be built with a high degree of reliability by using current state-of-the-art fail operational techniques. High speed modern flight aircraft employ gained scheduled damper systems in both longitudinal and lateral modes. These systems must cope with a large center of gravity variation which is not present in this spacecraft concept.

The improvements that are gained by feeding back 1 degree of elevon to 1 deg/sec of pitch rate are presented in Figure 7-37. Without pitch rate feedback all points in the flight envelope fell in the unacceptable region. However, with pitch rate feedback (constant gain) all points in the flight envelope fell either in the acceptable or the desired region of the Cornell[6] short-period handling qualities requirements for entry vehicles.

By feeding back 0.5 degree of rudder to 1 deg/sec of yaw rate the Dutch roll characteristics were improved to the point where all points in the flight envelope, when compared to the military requirements of $1/C_{\frac{1}{2}}$ and $|\phi|/|V_e|$, fell in the satisfactory region.

Figure 7-38 presents the lateral damping characteristics of this spacecraft concept in terms of military specification for flying qualities of piloted airplanes. The yaw rate feedback is equivalent to that of increasing C_{n_r}.

Another effective way for increasing the lateral damping is to feed back roll rate. An increased C_{ℓ_p} negatively (equivalent to roll rate feedback) gives increased Dutch roll damping and roll subsidence. However, it reduced the steady-state roll rate and the time to reach 30° bank angle. From a pilot's standpoint, yaw rate feedback is better than roll rate feedback.

SECTION 8

CONCLUSIONS

This study was conducted to determine the flight characteristics of a high L/D spacecraft concept with a single pivot, two-position skewed wing which is deployed at subsonic speeds from the stowed position ($\Lambda = 90°$) to the fully deployed position ($\Lambda = 0°$). The results of the analysis have been presented in terms of time histories, landing characteristic parameters, existing military specifications, and proposed entry vehicle specifications. The following conclusions are drawn:

a. The vehicle with center of gravity located at 65 percent of the body length was dynamically stable longitudinally for all points in the flight envelope, but artificial damping in pitch is required for all conditions to achieve a satisfactory degree of longitudinal stability based on handling qualities specification for entry vehicles.

b. The vehicle was dynamically stable in the Dutch roll mode for all points in the flight envelope, but artificial damping in yaw is required for all conditions to achieve a satisfactory degree of Dutch roll stability based on handling qualities specification for piloted airplanes.

c. The lateral control provided by the ailerons gave satisfactory roll response in terms of a proposal criterion for piloted entry vehicles which require that the aileron produce a bank angle of at least 30° in 1 second; the evaluation of the response in roll control in terms of ω_ϕ/ω_d indicated that the lateral control characteristics of this spacecraft concept are adequate.

d. The stability augmentation system needed for this spacecraft concept is within the state-of-the-art fail operational type. Simple rate feedback with possible gain scheduling with Mach number is the type of system proposed.

e. The best speed for wing deployment is approximately Mach 0.6 at an altitude of 30,000 feet. The dynamic transients produced are minimum because the angles of attack at wing deployment are below those values where the skewed wing produces severe lateral cross coupling.

f. The vehicle has good landing characteristics with a no flap approach speed of 165 knots at a flight path angle of 10°. The flare initiation altitude is 275 feet and a flare load factor of 0.2 g. It does not appear that wing flaps improve the landing characteristics enough to warrant the added weight and complexity.

g. More control power for trimming the vehicle would reduce the elevon deflection which borders the 25° point. The control effectiveness drops off rapidly at about 25°.

SECTION 9

REFERENCES

1. Spencer, Bernard, Jr., and Charles H. Fox, Jr., Hypersonic Aerodynamic Performance of Minimum Wave-Drag Bodies, NASA TR-R-250, 1966.

2. Kelly, H. R., "The Estimation of Normal-Force, Drag, and Pitching-Moment Coefficients for Blunt-Based Bodies of Revolution at Large Angles of Attack," Journal of the Aeronautical Sciences, August 1954.

3. Toll, T. A., Approximate Relations and Charts for Low-Speed Stability Derivatives of Swept Wings, NACA TN 1581, May 1948.

4. U. S. Standard Atmosphere, 1962.

5. Breuhaus, W. O., P. A. Reynolds, and F. A. Kidd, Handling Qualities Requirements for Hyper-Velocity Aircraft, Report No. TC-1332-F-1 (Contract No. AF33(616)-6240), Cornell Aeron. Lab., Inc. 30 September 1959 (Rev. 28 January 1960). (Available from ASTIA as AD 323 250.)

6. Flying Qualities of Piloted Airplane, MIL Specification MIL-F-8785 (AS6), September 1954.

7. Dynamics of the Airframe, Navy Report BUAR AE-61-4, Vol. II, February 1953.

APPENDIX A

SMALL PERTURBATION EQUATIONS

Since most handling qualities requirements are specified in terms of modes, frequencies, and damping, it is important to have a method which can readily evaluate these parameters. A digital computer program was designed to proceed from a description of the vehicle in terms of its mass properties and aerodynamic characteristics to the various transfer function. The program trims the vehicle to one of four possible conditions: (1) maximum L/D, (2) maximum lift, (3) flight path angle, and (4) load factor.

From the trim condition, dimensionalized stability coefficients are computed by perturbing in sequence all of the independent variables and noting the resulting change in the forces and moments. The resulting perturbation quantities, which are normalized to units of angular and linear acceleration, are the first partial derivative terms of the Taylor's series expansion about the trim point.

Equations A-1 and A-2 are the linearized small perturbation equations of motion for the longitudinal and lateral modes of motion respectively. These equations are the conventional set used in aircraft analysis and can be found in Reference 7.

	U	W	q/s	N_z		δ_e
Axial Force	$-X_u$ $+s$	$Q_o - X_w$	$g\cos\theta$ $+W_o s$	0		X_{δ_e}
Normal Force	$-Q_o - Z_u$	$-Z_w$ $+(1-Z_{\dot{w}})\,s$	$+g\sin\theta$ $-(U_o + Z_q)\,s$	0		Z_{δ_e}
					=	
Pitch Moment	$-M_u$	$-M_w$ $-M_{\dot{w}}\,s$	0 $-Mq\,s$ $+s^2$	0		M_{δ_e}
Normal Acceleration	Q_o	0 $-s$	$-g\sin\theta$ $+U_o s$	1.		0

(A-1)

	β	p/s	R/s	N_y	δ_α	δ_r
Lateral Force	$\dot{V}_o - Y_\beta$ Vs	$-g\cos\theta$ $-(W_o + Y_p)s$	$-g\sin\theta$ $+(U_o - Y_R)s$	0	Y_{δ_α}	Y_{δ_r}
Roll Moment	0 $-L_\beta$	0 $-(L_p + Q_o I_{xz}/I_{xx})s$ $+s^2$	0 $-[L_R - Q_o(I_{zz} - I_{yy})I_{xx}]s$ $-(I_{xz}/I_{xx})s^2$	0	L_{δ_α}	L_{δ_r}
Yaw Moment	0 $-N_\beta$	0 $-[N_p - Q_o(I_{yy} - I_{xx})/I_{zz}]s$ $-(I_{xz}/I_{zz})s^2$	0 $-[N_R - Q_o I_{xz}/I_{zz}]s$ $+s^2$	0	N_{δ_α}	N_{δ_r}
Lateral Acceleration	$-\dot{V}_o$ $-Vs$	$+g\cos\theta$ $W_o s$	$g\sin\theta$ $-U_o$	1.	0	0

=

(A-2)

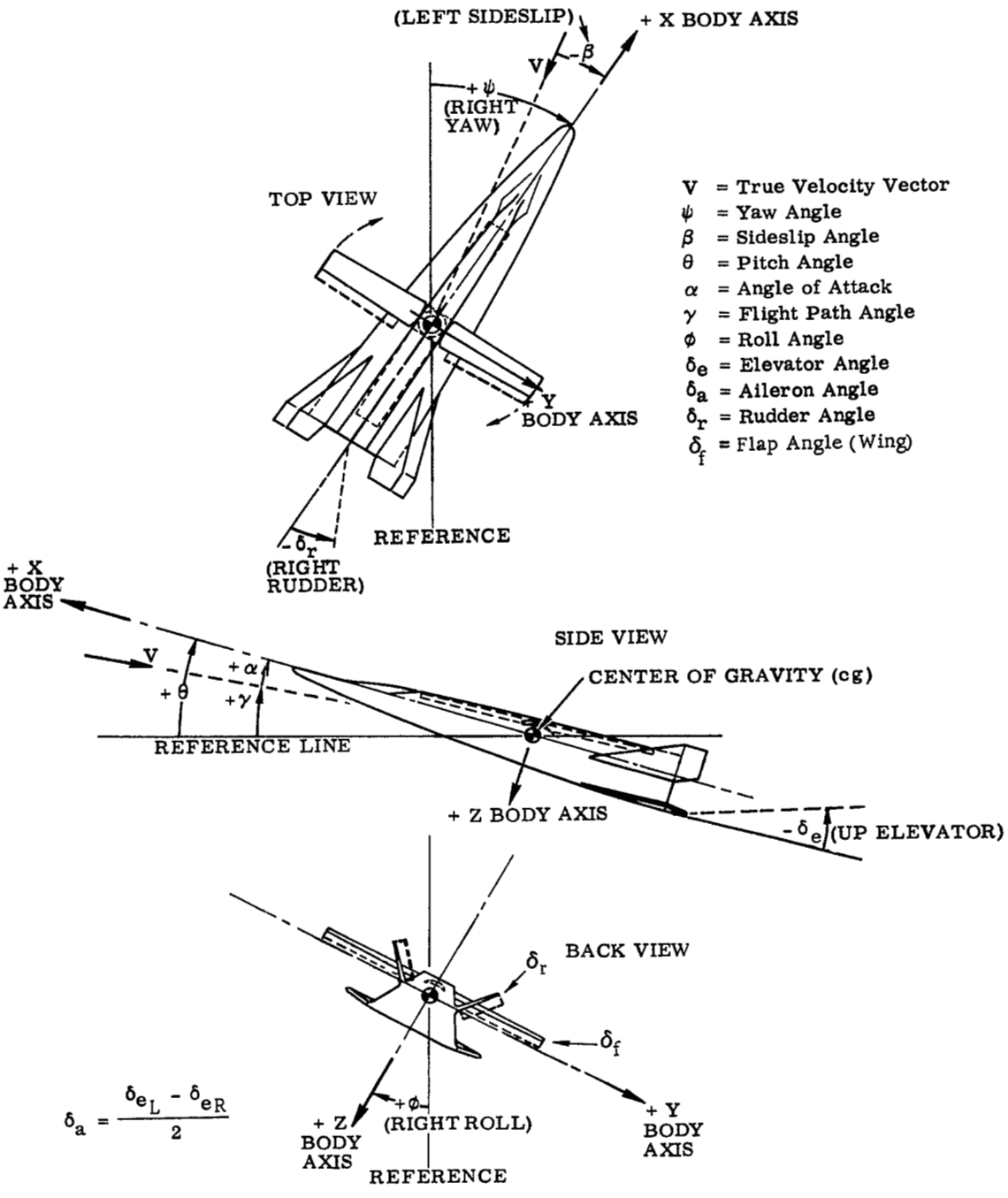

Figure 1-1. Sign Convention

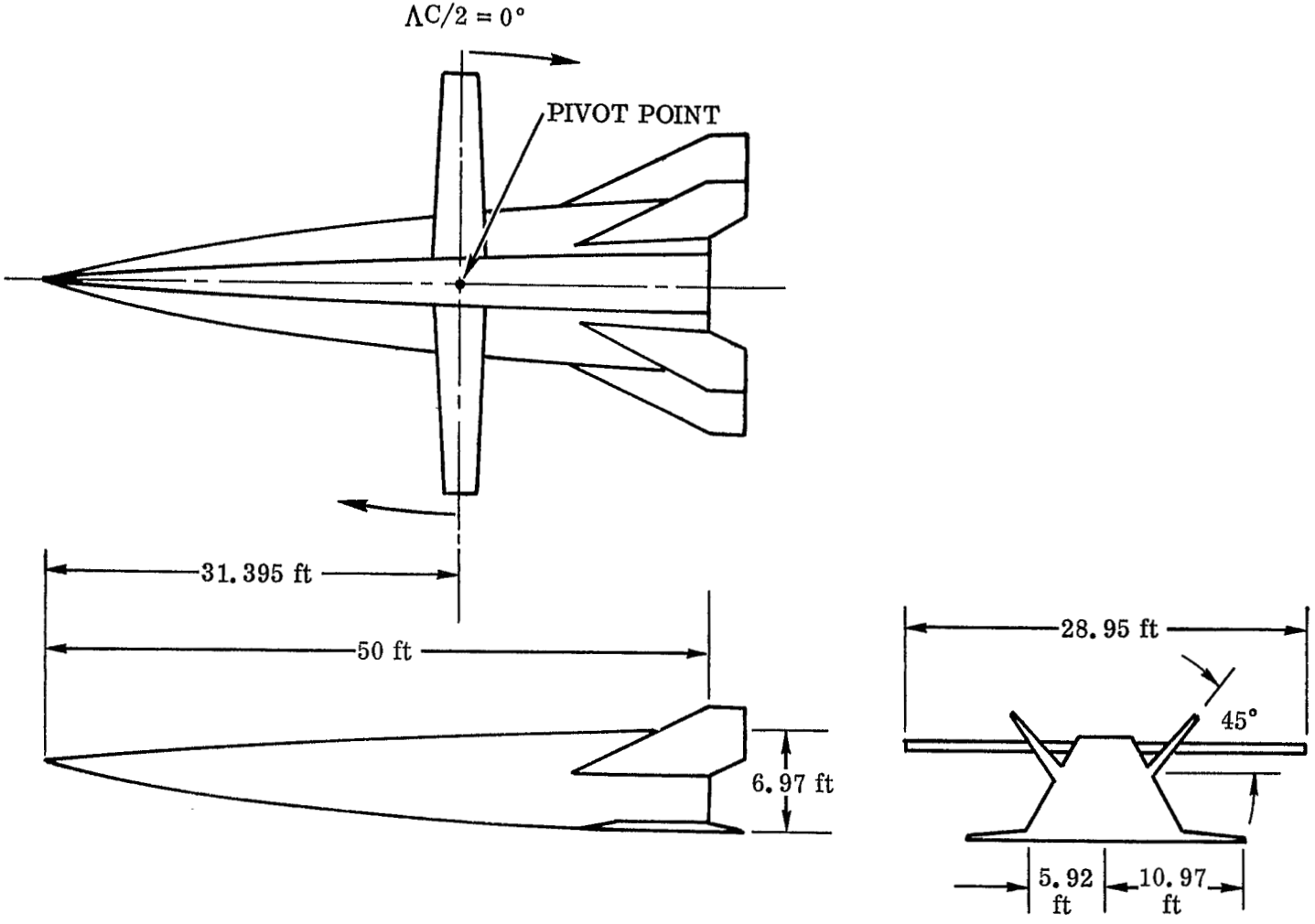

Figure 2-1. Spacecraft Concept

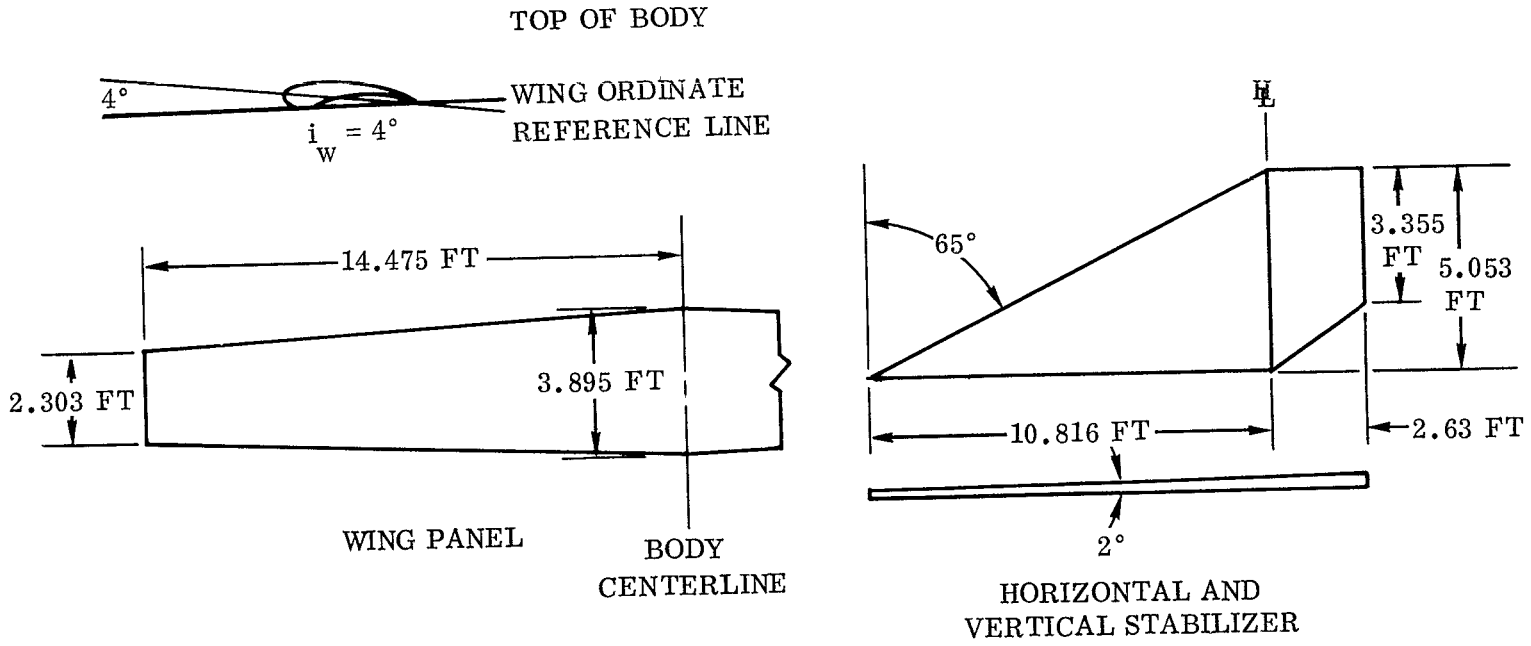

Figure 2-2. Spacecraft Wing and Tails

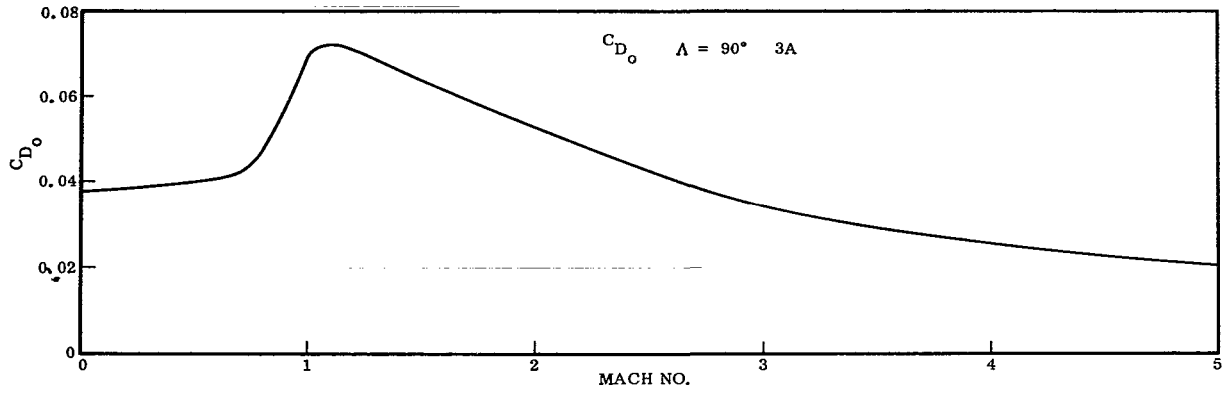

Figure 3-1. Drag Coefficient at Zero Angle of Attack

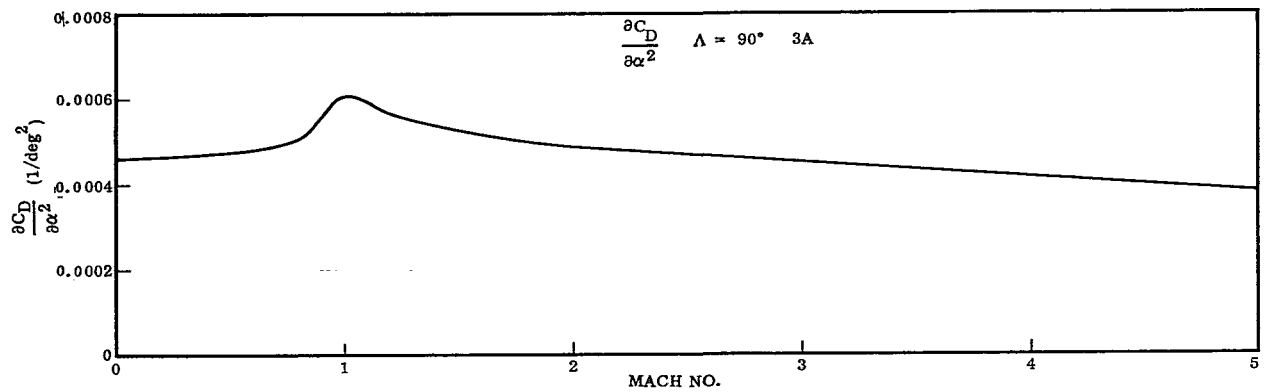

Figure 3-2. Partial Derivative of the Drag Coefficient with Angle of Attack Squared

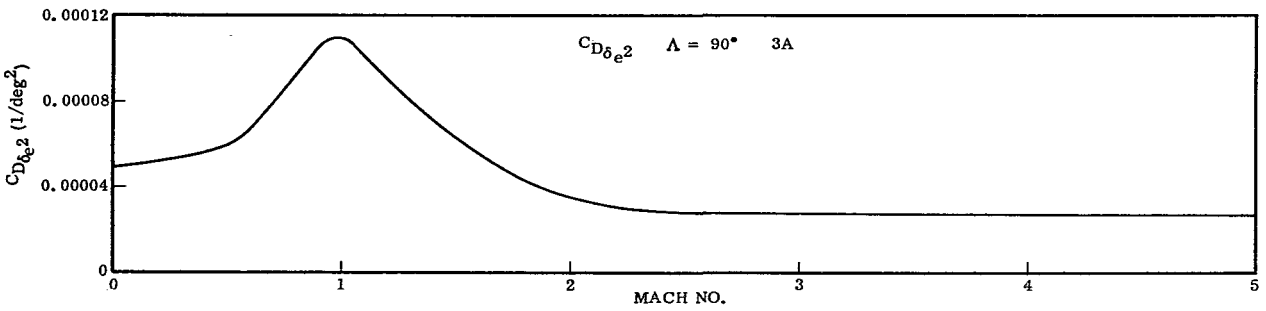

Figure 3-3. Partial Derivative of the Drag Coefficient with Elevator Deflection Squared

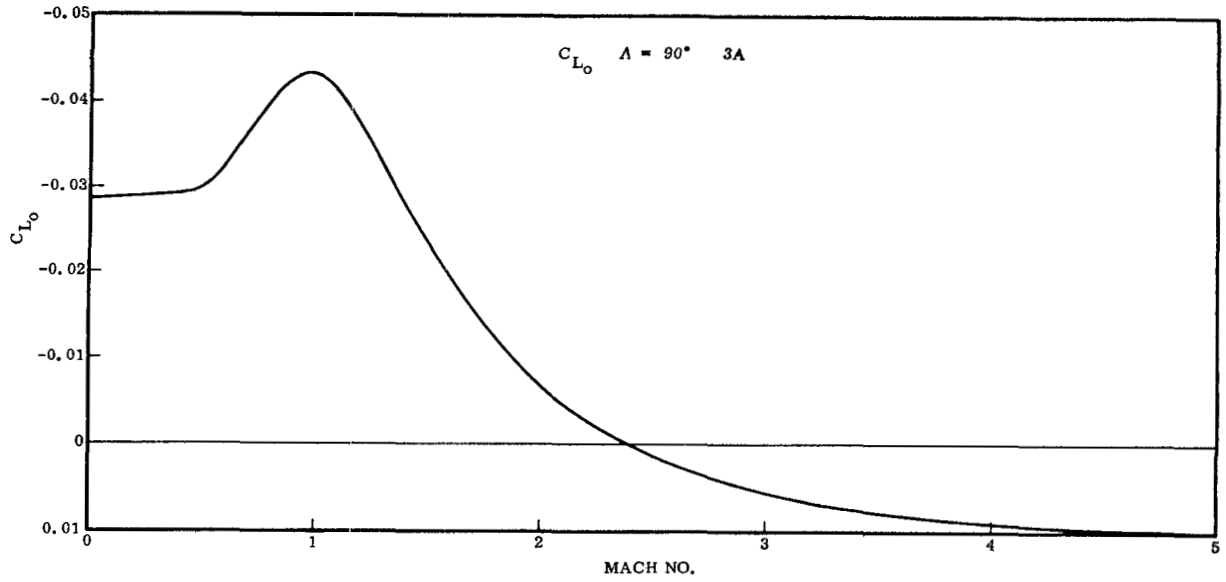

Figure 3-4. Lift Coefficient at Zero Angle of Attack

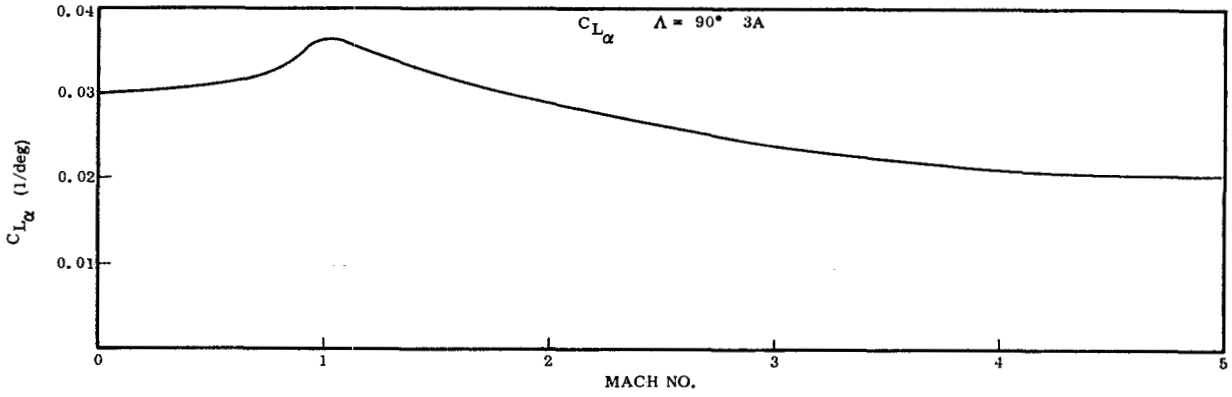

Figure 3-5. Lift Curve Slope

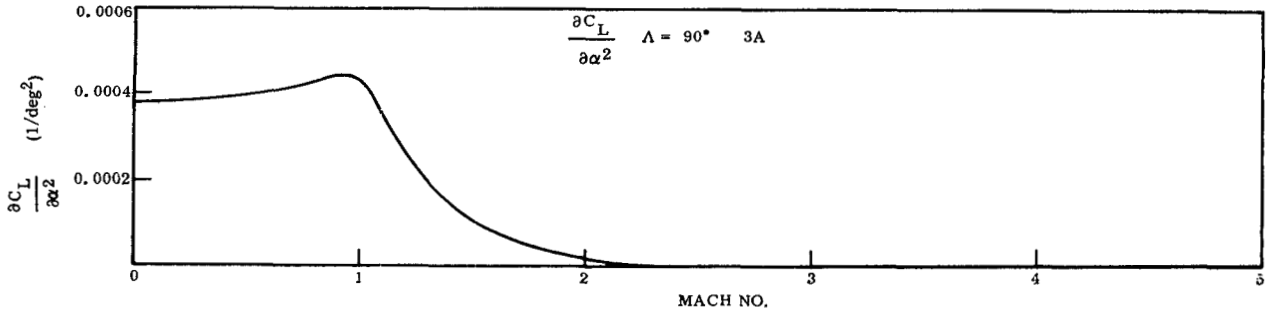

Figure 3-6. Partial Derivative of the Lift Coefficient with Angle of Attack Squared

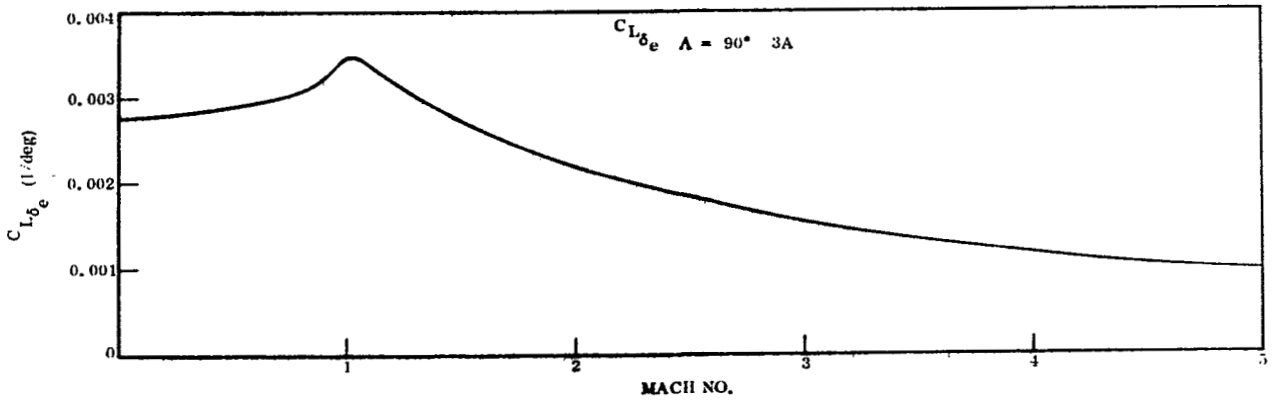

Figure 3-7. Partial Derivative of the Lift Coefficient with Elevator Deflection

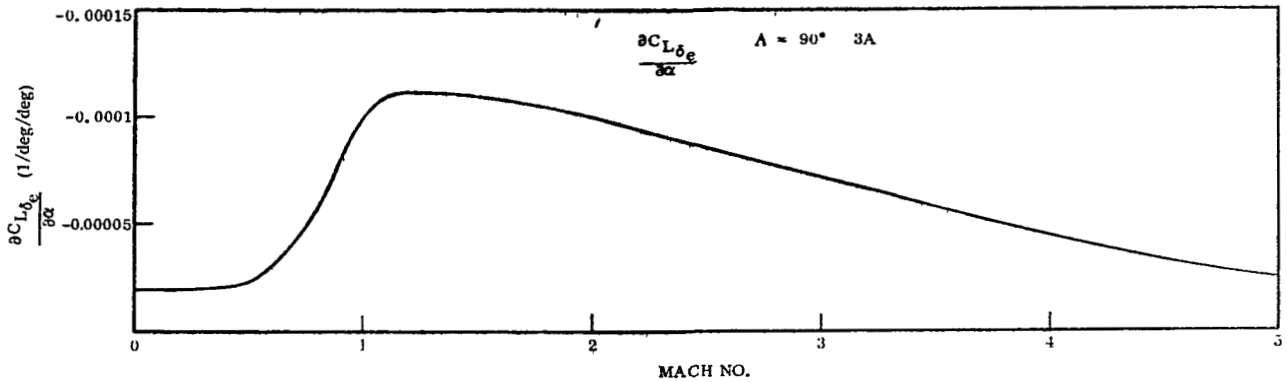

Figure 3-8. Partial of Elevator Lift Curve Slope Coefficient with Angle of Attack

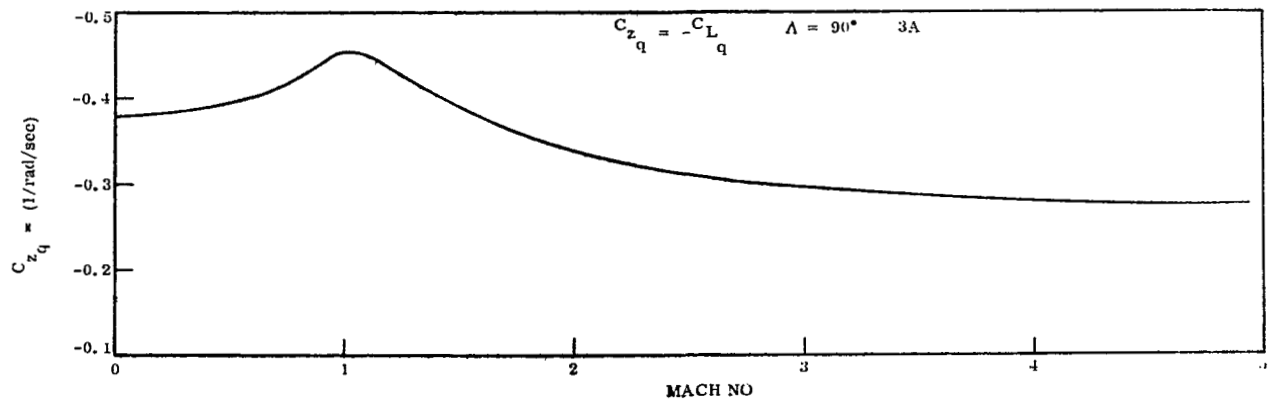

Figure 3-9. Lift Coefficient Due to Pitching Velocity

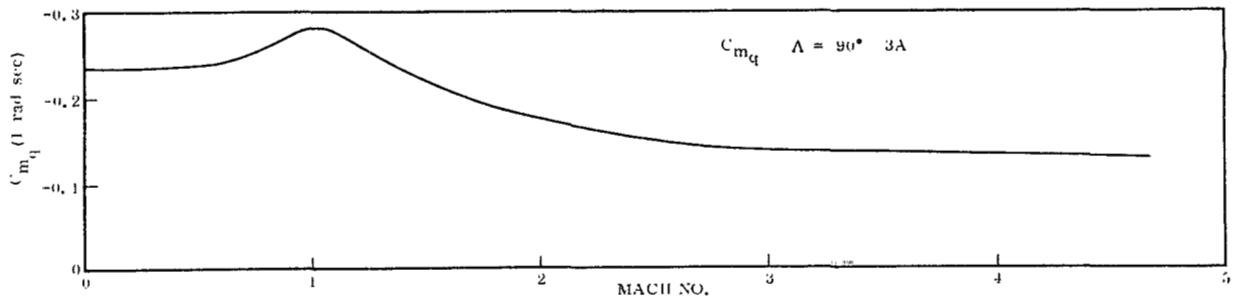

Figure 3-10. Pitching Moment Coefficient Due to Pitching Velocity

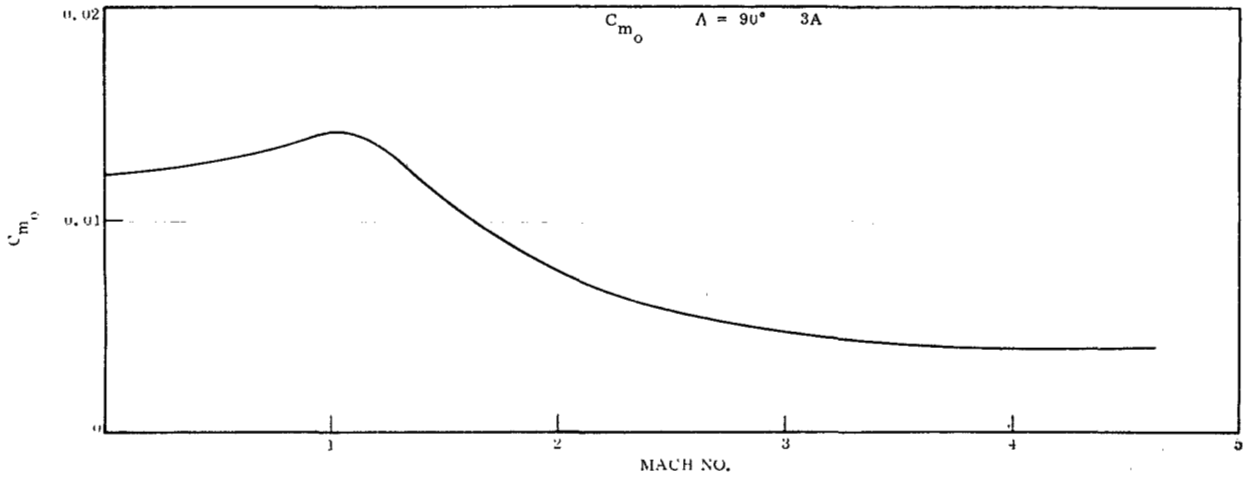

Figure 3-11. Pitching Moment Coefficient at Zero Angle of Attack

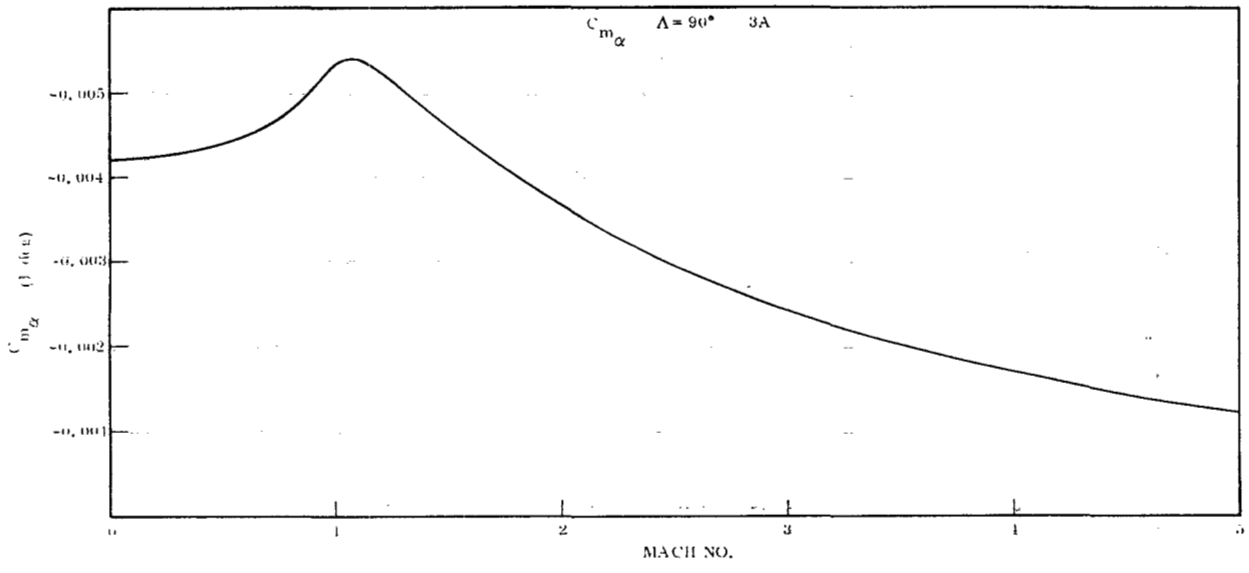

Figure 3-12. Partial of Pitching Moment Coefficient with Angle of Attack

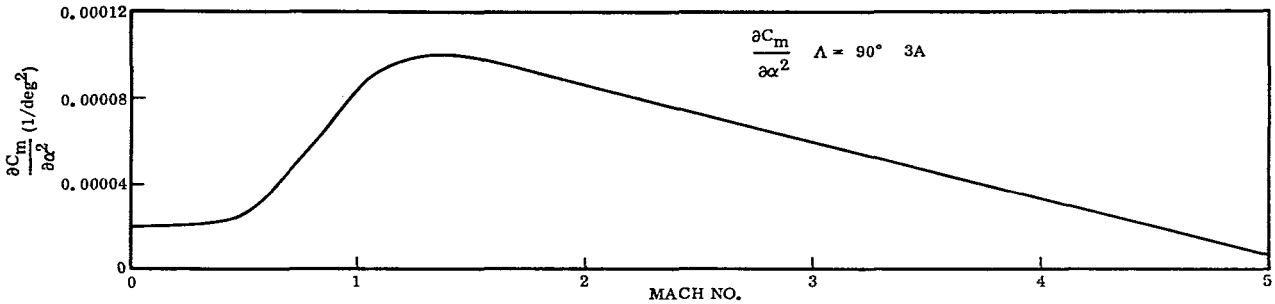

Figure 3-13. Partial of Pitching Moment Coefficient with Angle of Attack Squared

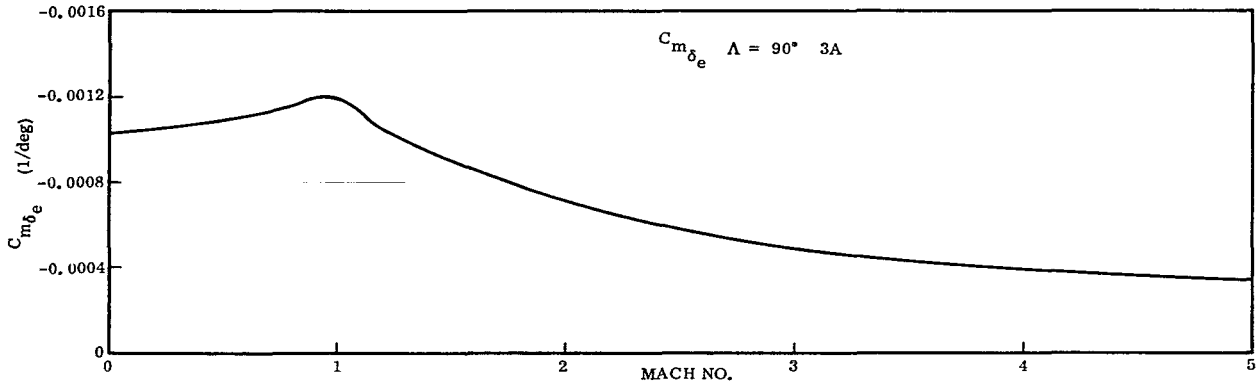

Figure 3-14. Pitching Moment Coefficient Due to Elevator Deflection

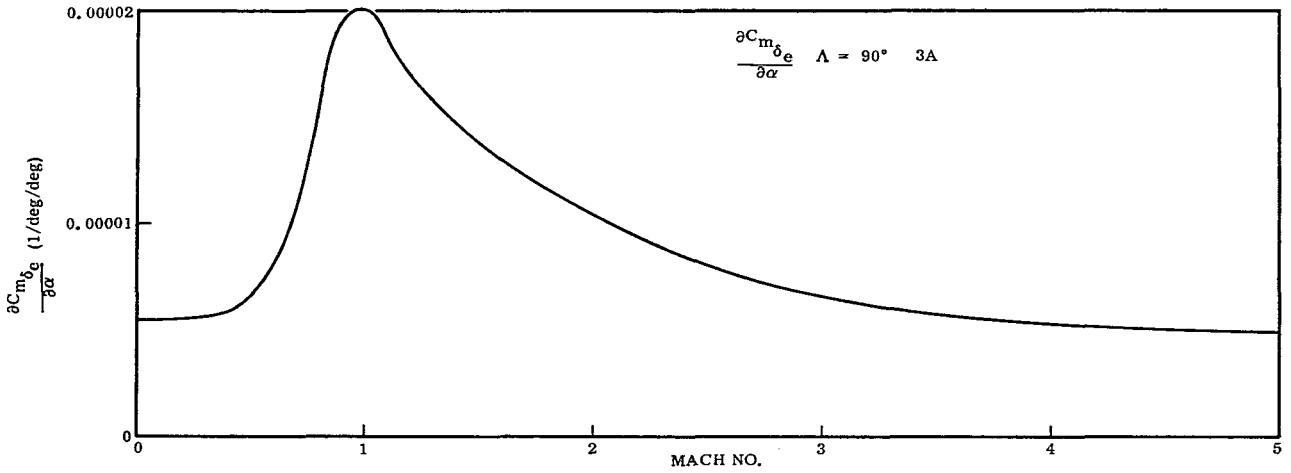

Figure 3-15. Partial of Pitching Moment Coefficient Due to Elevator Deflection with Angle of Attack

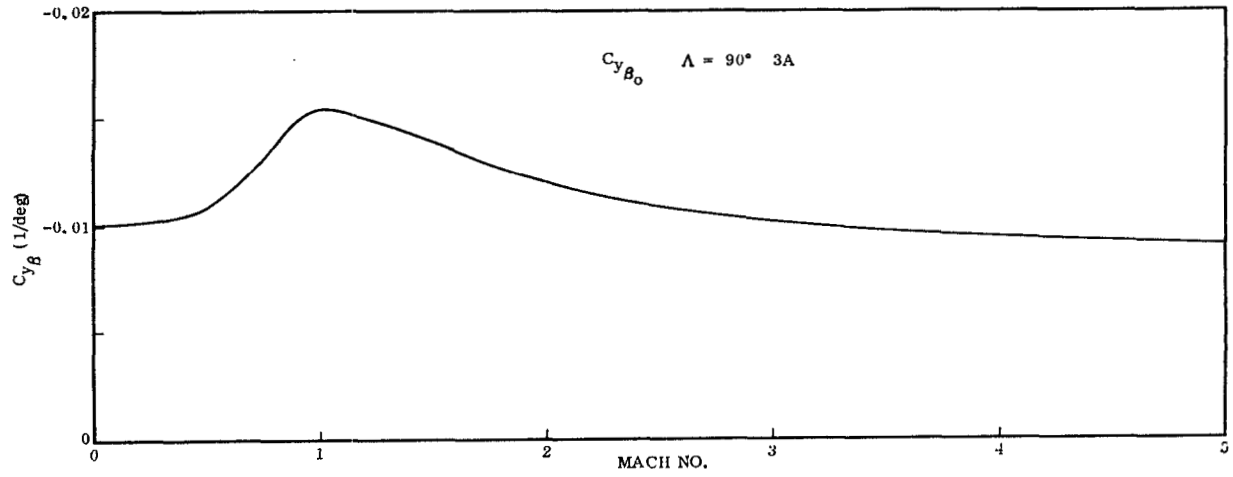

Figure 3-16. Side Force Stability Parameter

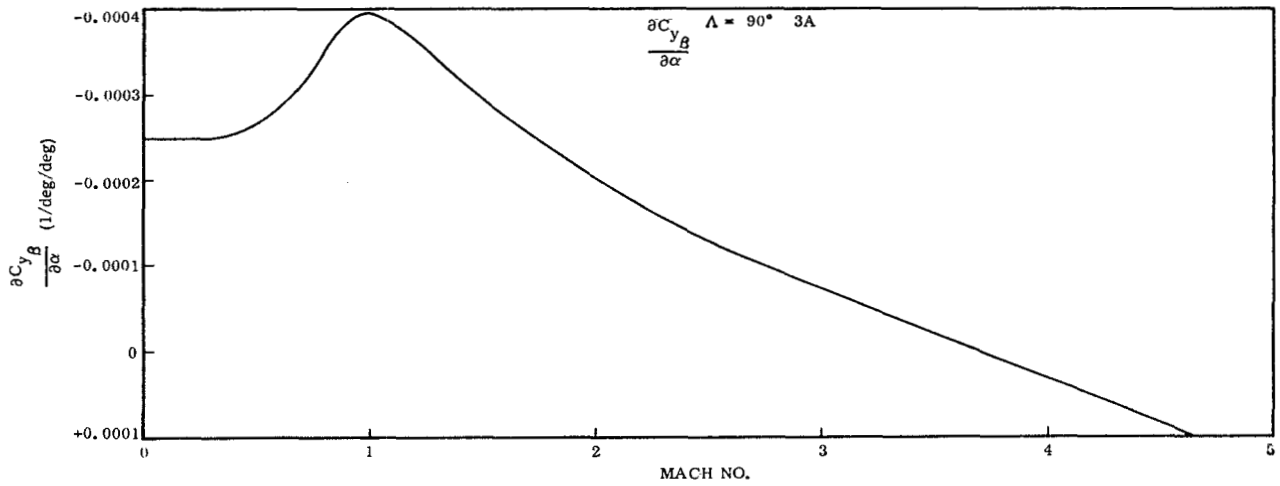

Figure 3-17. Partial of Side Force Stability Parameter with Angle of Attack

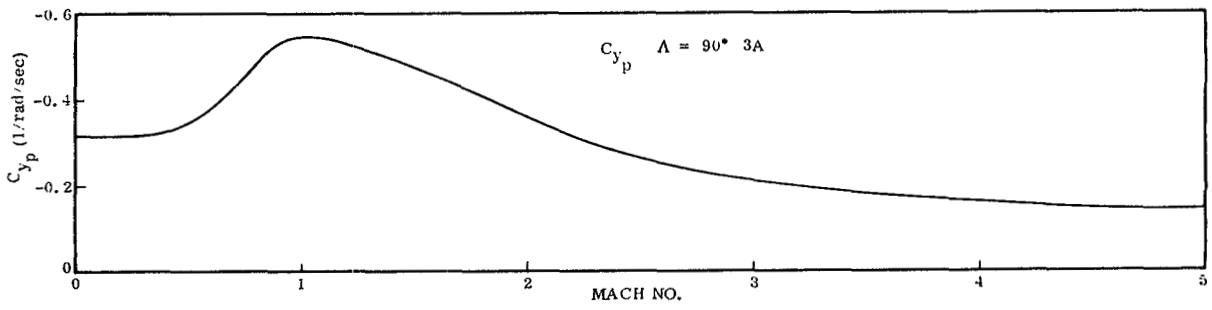

Figure 3-18. Side Slip Side Force Coefficient Due to Rolling Velocity

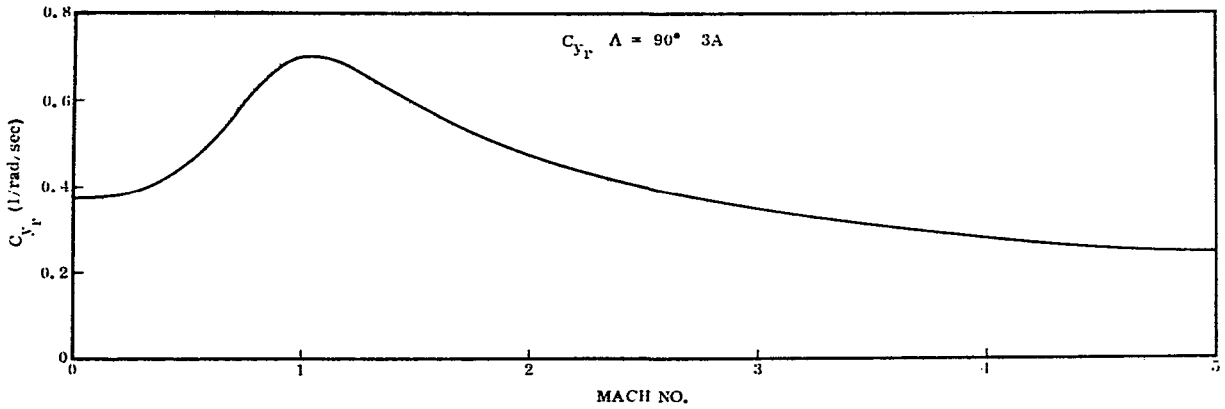

Figure 3-19. Side Slip Side Force Coefficient Due to Yawing Velocity

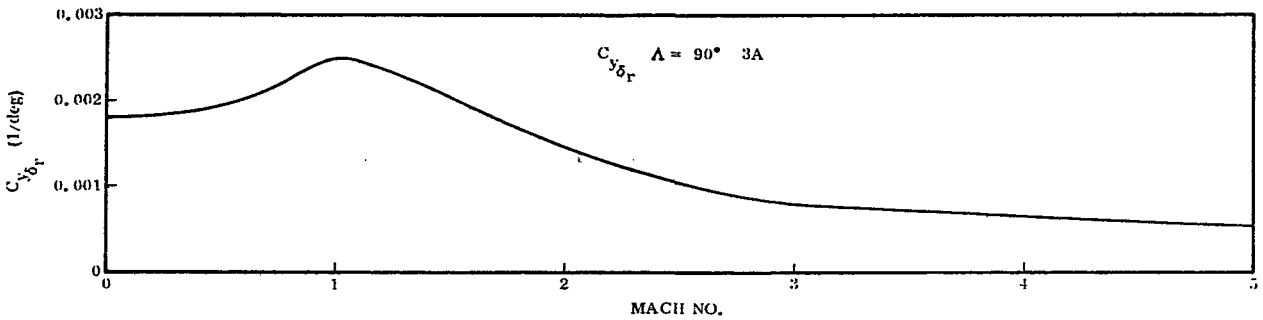

Figure 3-20. Rudder Side Force Coefficient

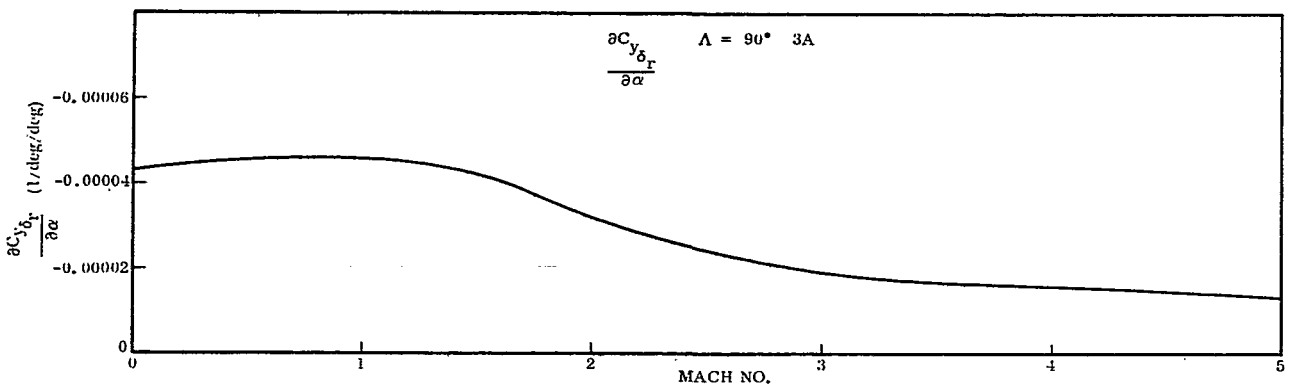

Figure 3-21. Partial of Rudder Side Force Coefficient with Angle of Attack

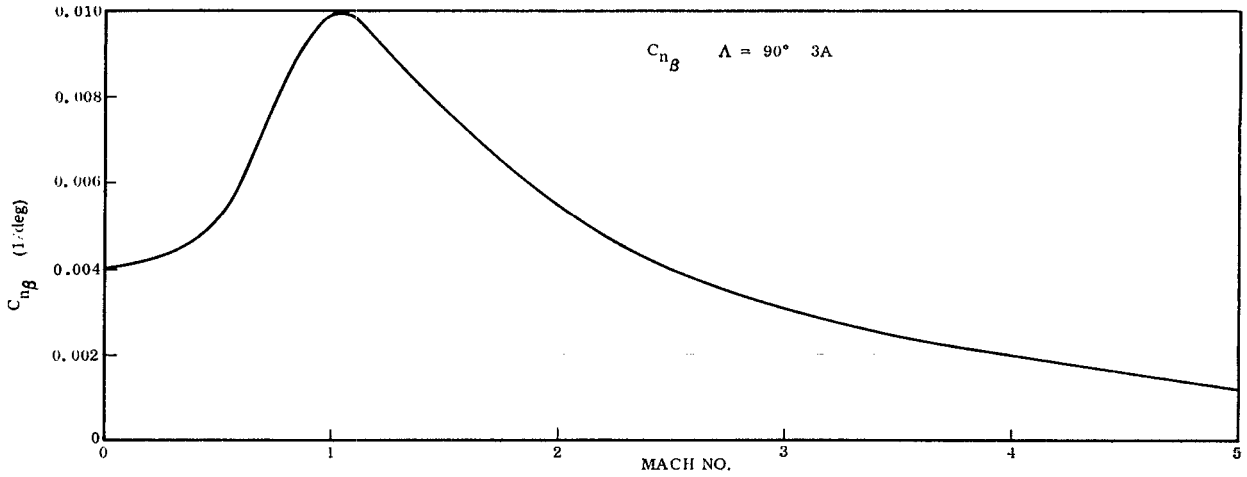

Figure 3-22. Side Slip Directional Stability Parameter

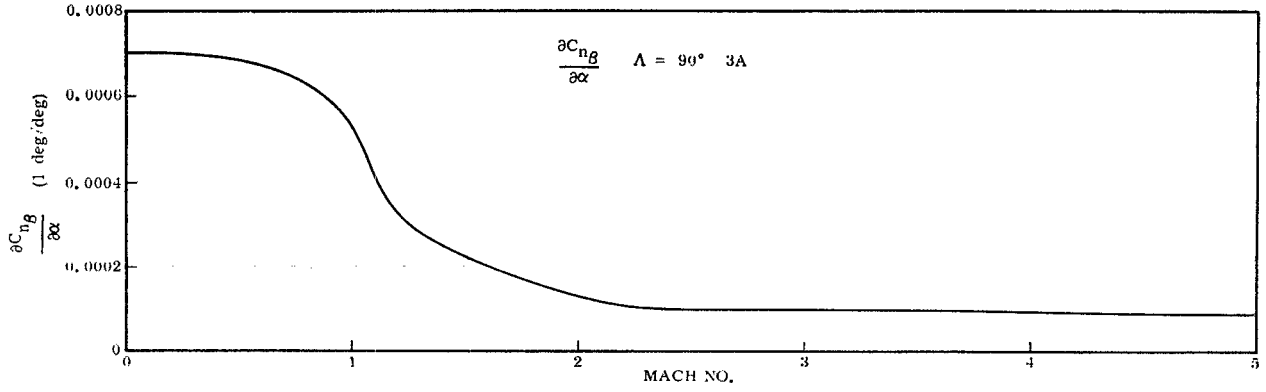

Figure 3-23. Partial of Side Slip Directional Stability Parameter with Angle of Attack

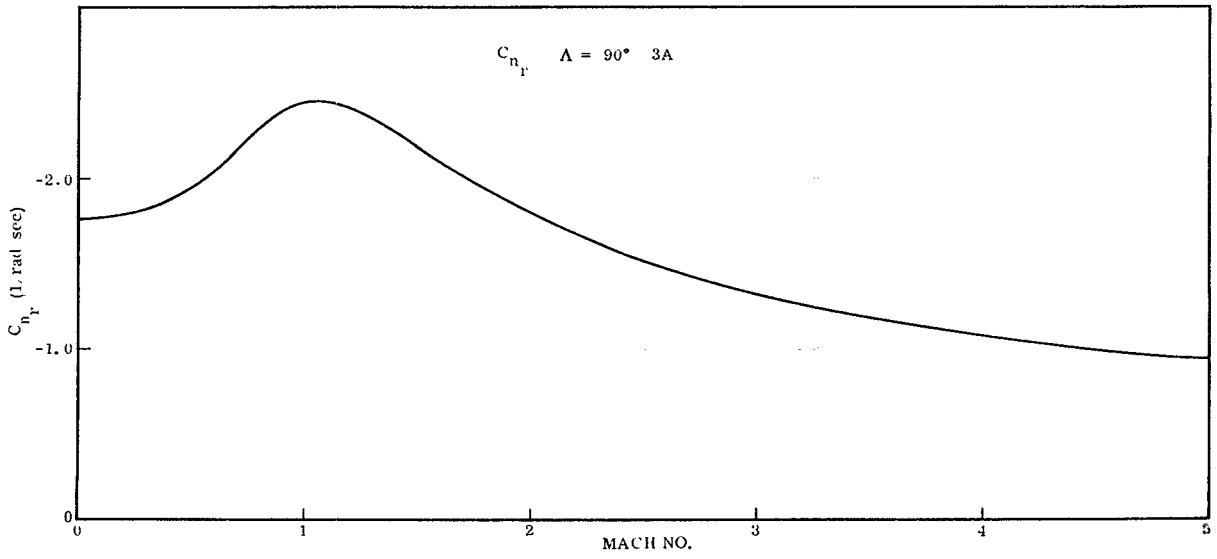

Figure 3-24. Yawing Moment Coefficient Due to Yawing Velocity

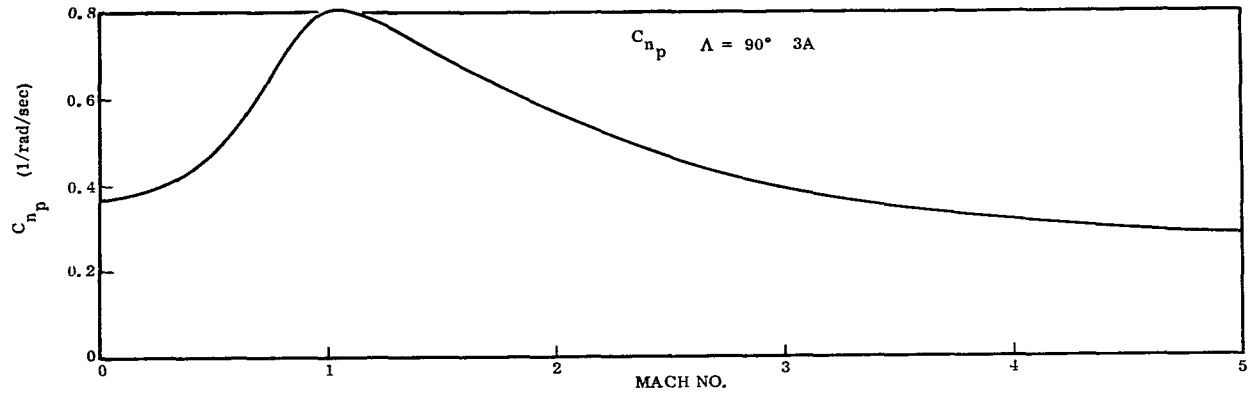

Figure 3-25. Yawing Moment Coefficient Due to Rolling Velocity

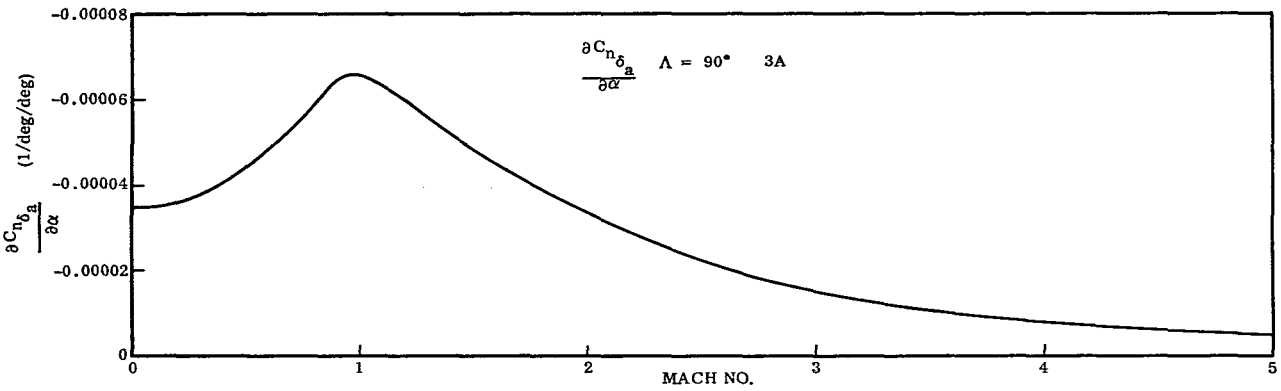

Figure 3-26. Partial of Yawing Moment Coefficient Due to Aileron Deflection with Angle of Attack

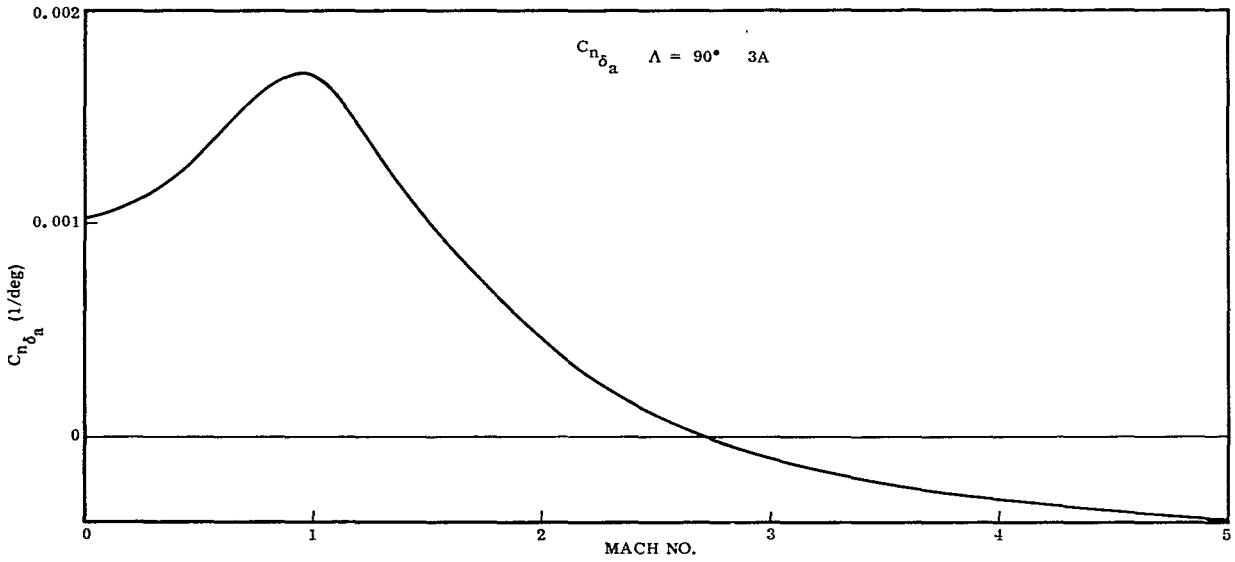

Figure 3-27. Yawing Moment Coefficient Due to Aileron Deflection

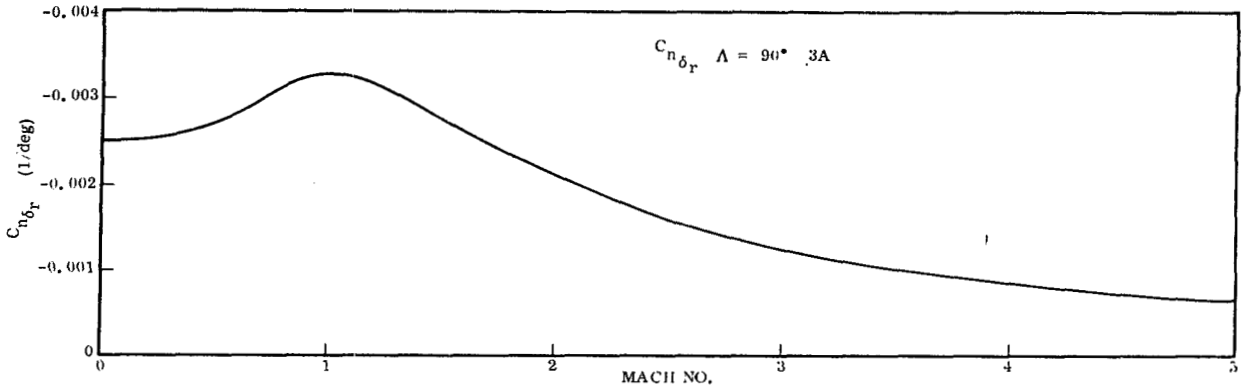

Figure 3-28. Yawing Moment Coefficient Due to Rudder Deflection

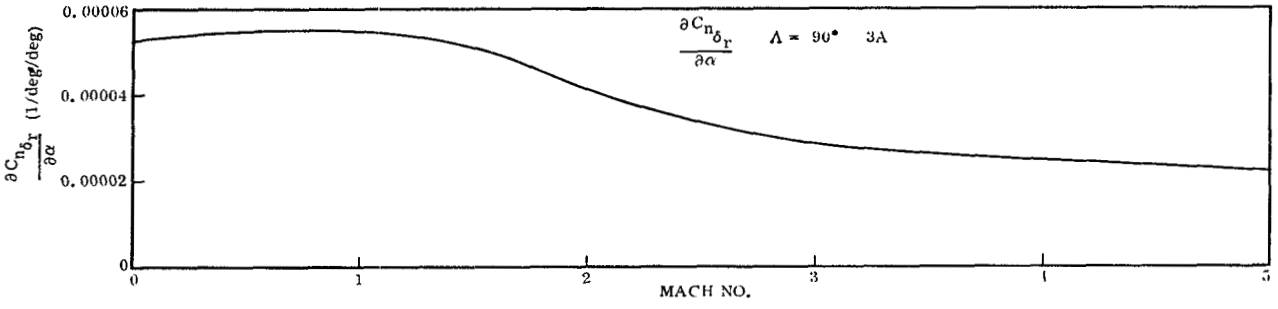

Figure 3-29. Partial of Yawing Moment Coefficient Due to Rudder Deflection with Angle of Attack

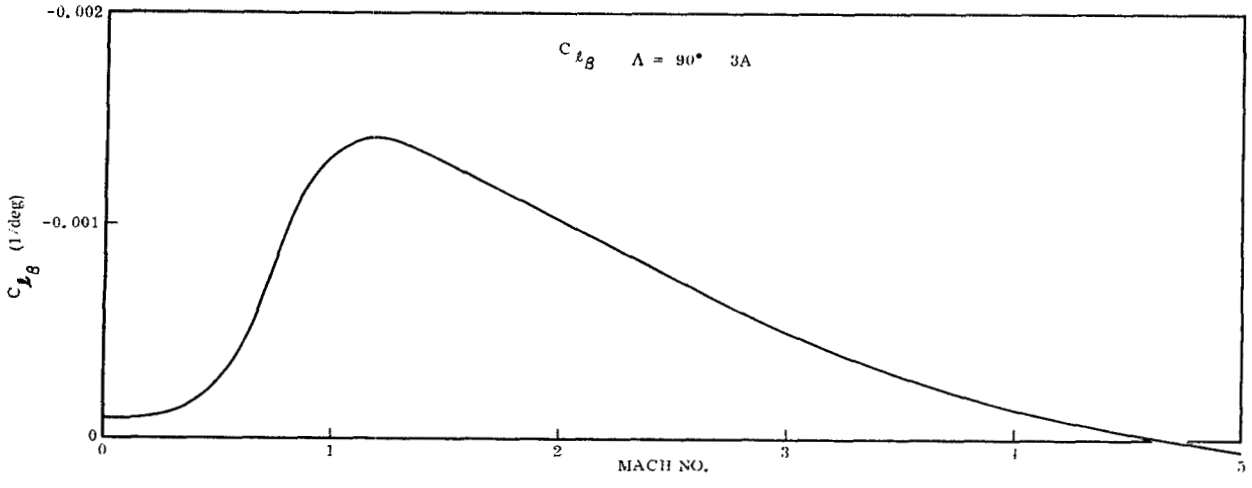

Figure 3-30. Lateral Stability Parameter Due to Side Slip

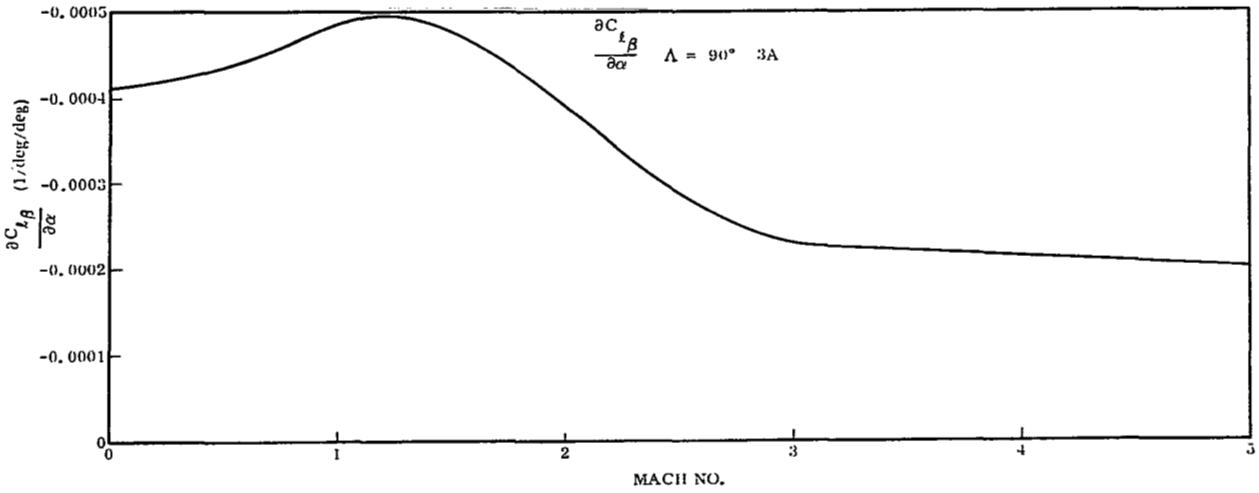

Figure 3-31. Partial of Lateral Stability Parameter Due to Side Slip with Angle of Attack

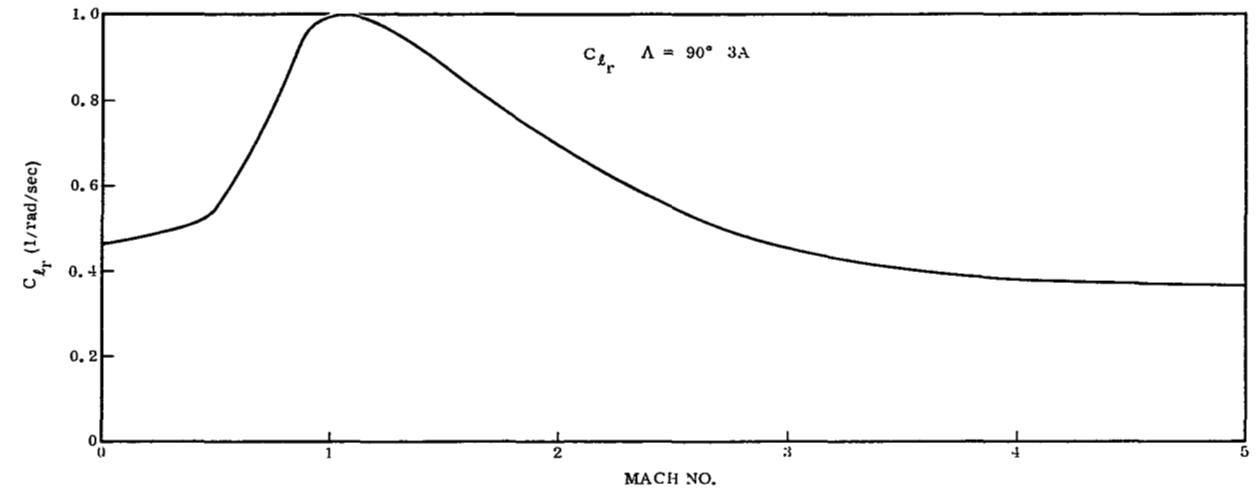

Figure 3-32. Rolling Moment Coefficient Due to Yawing Velocity

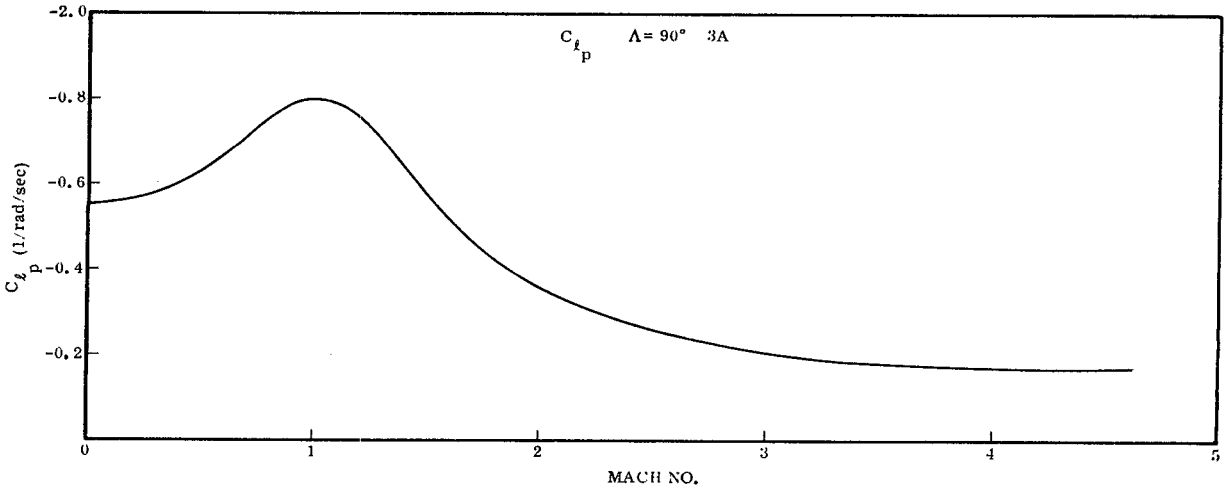

Figure 3-33. Rolling Moment Coefficient Due to Rolling Velocity

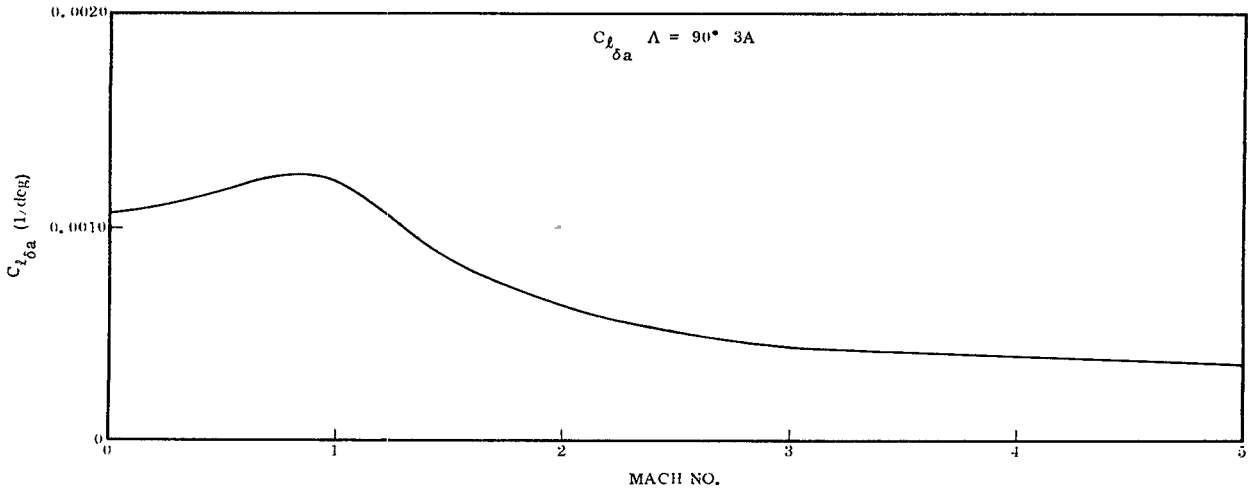

Figure 3-34. Rolling Moment Coefficient Due to Aileron Deflection

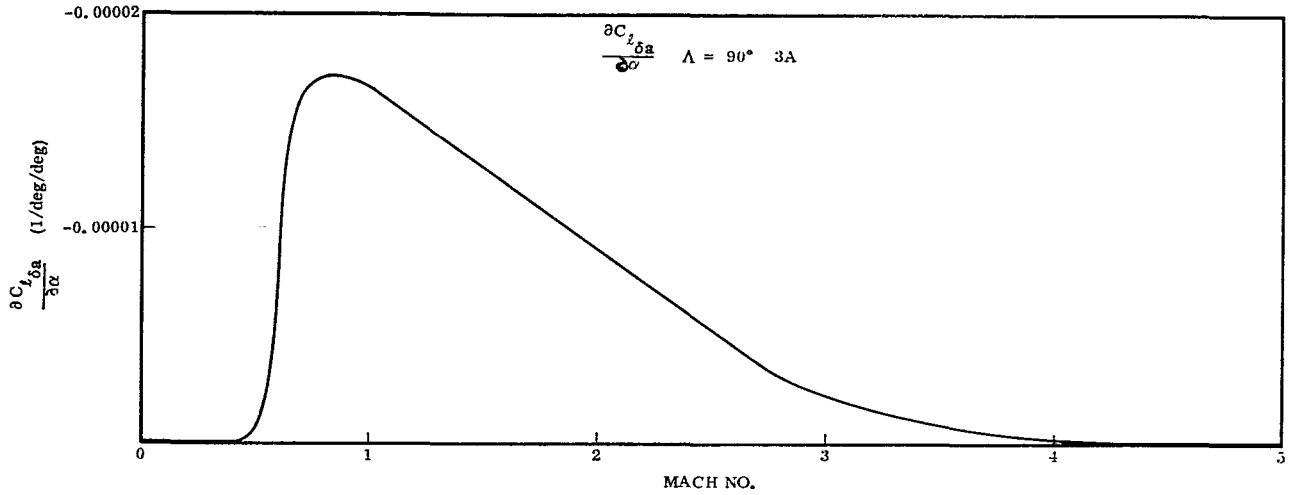

Figure 3-35. Partial of Rolling Moment Coefficient Due to Aileron Deflection with Angle of Attack

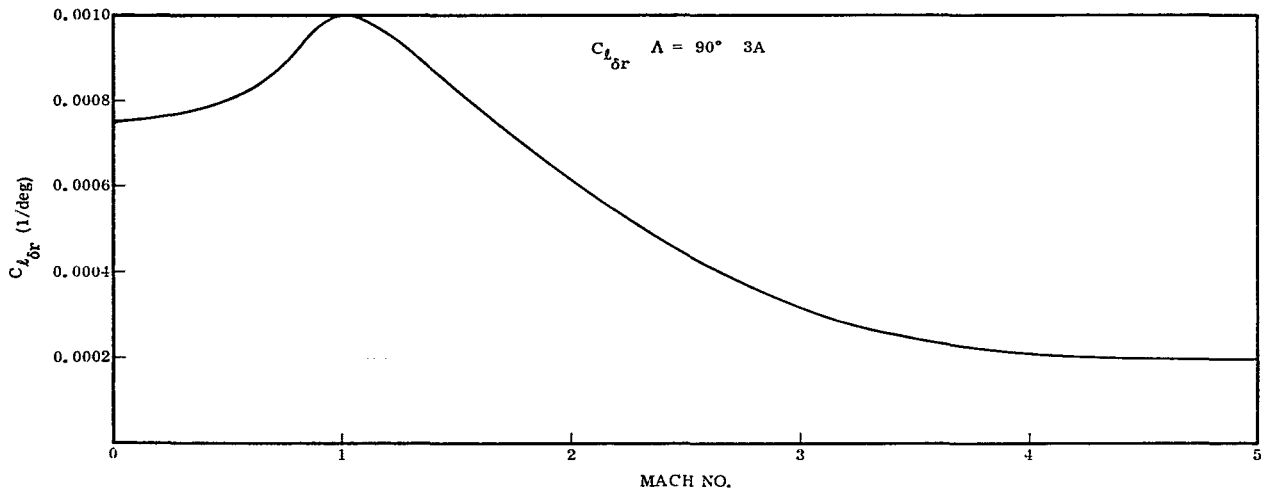

Figure 3-36. Rolling Moment Coefficient Due to Rudder Deflection

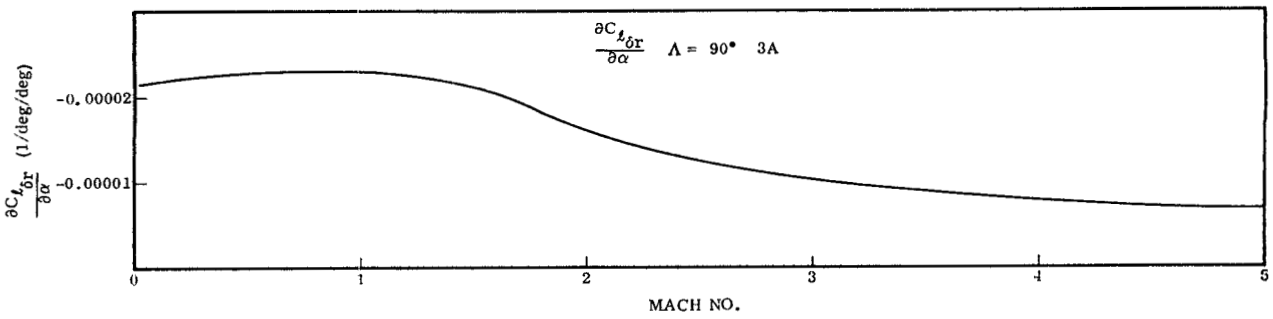

Figure 3-37. Partial of Rolling Moment Coefficient Due to Rudder Deflection with Angle of Attack

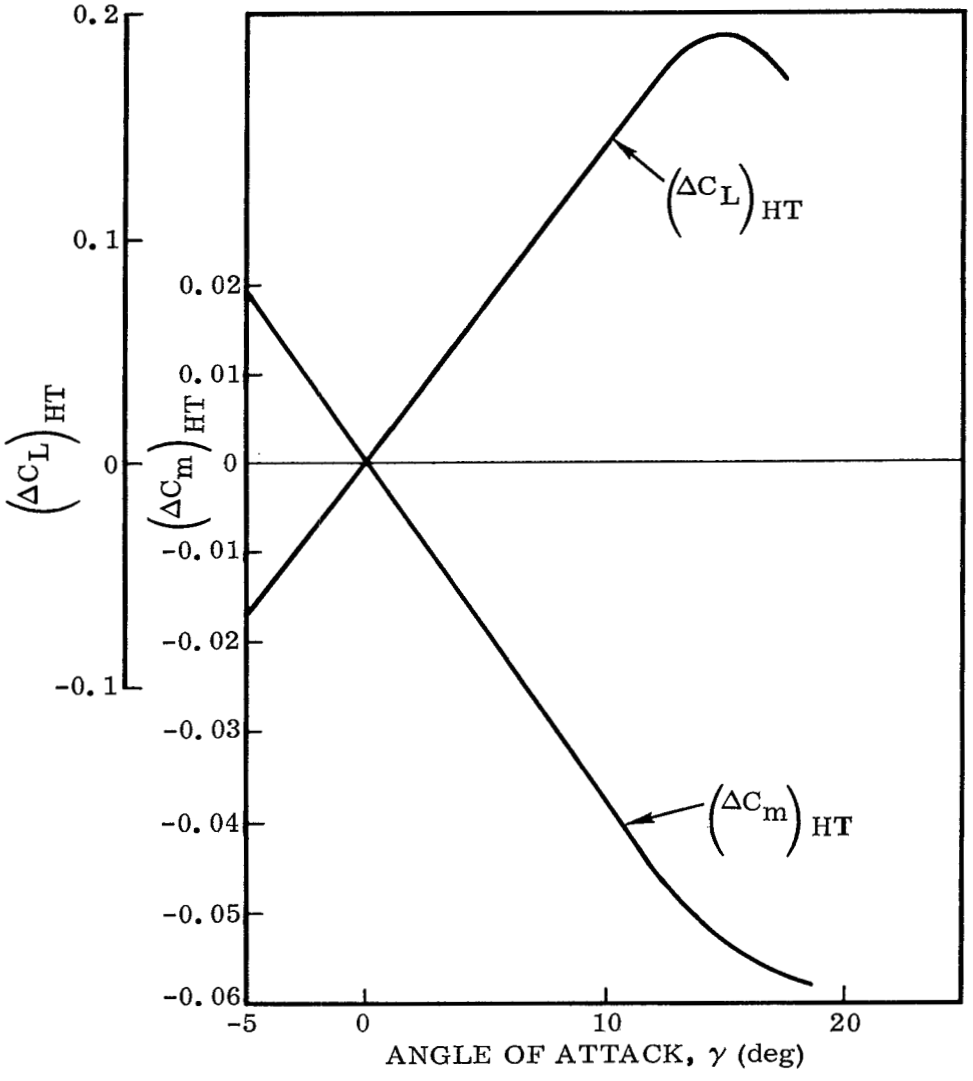

Figure 3-38. Horizontal Tail Incremental Lift and Moment at Low Speed

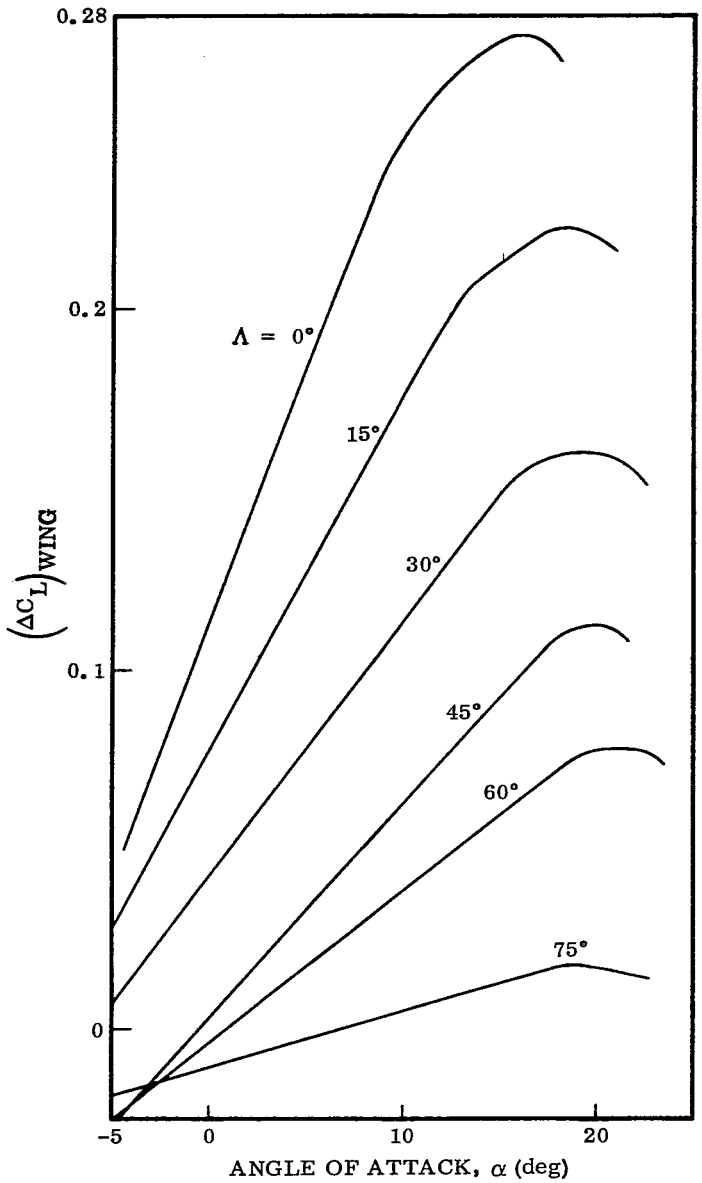

Figure 4-1. Incremental Wing Lift

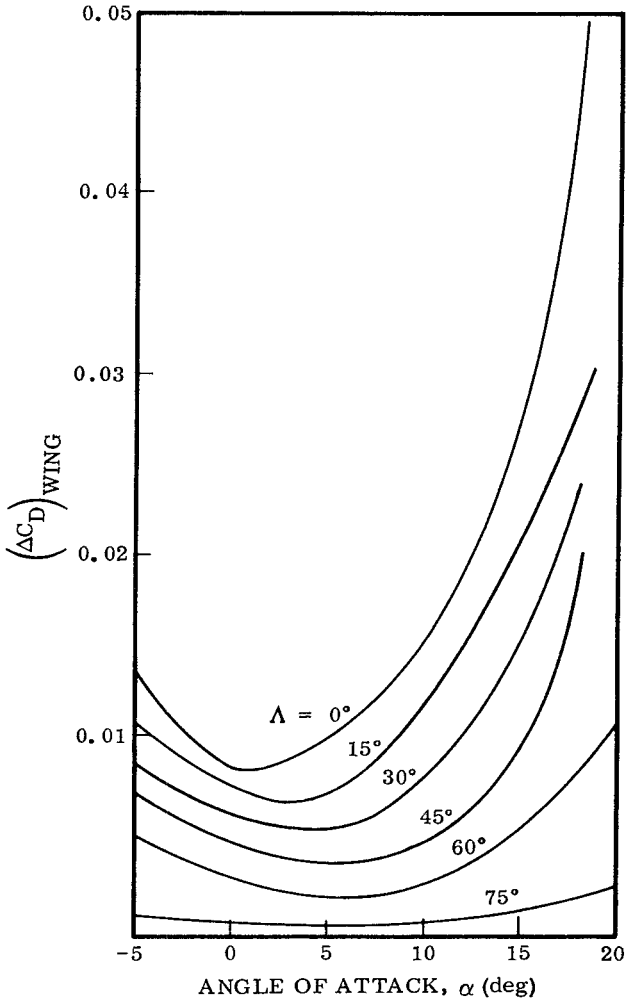

Figure 4-2. Incremental Wing Drag

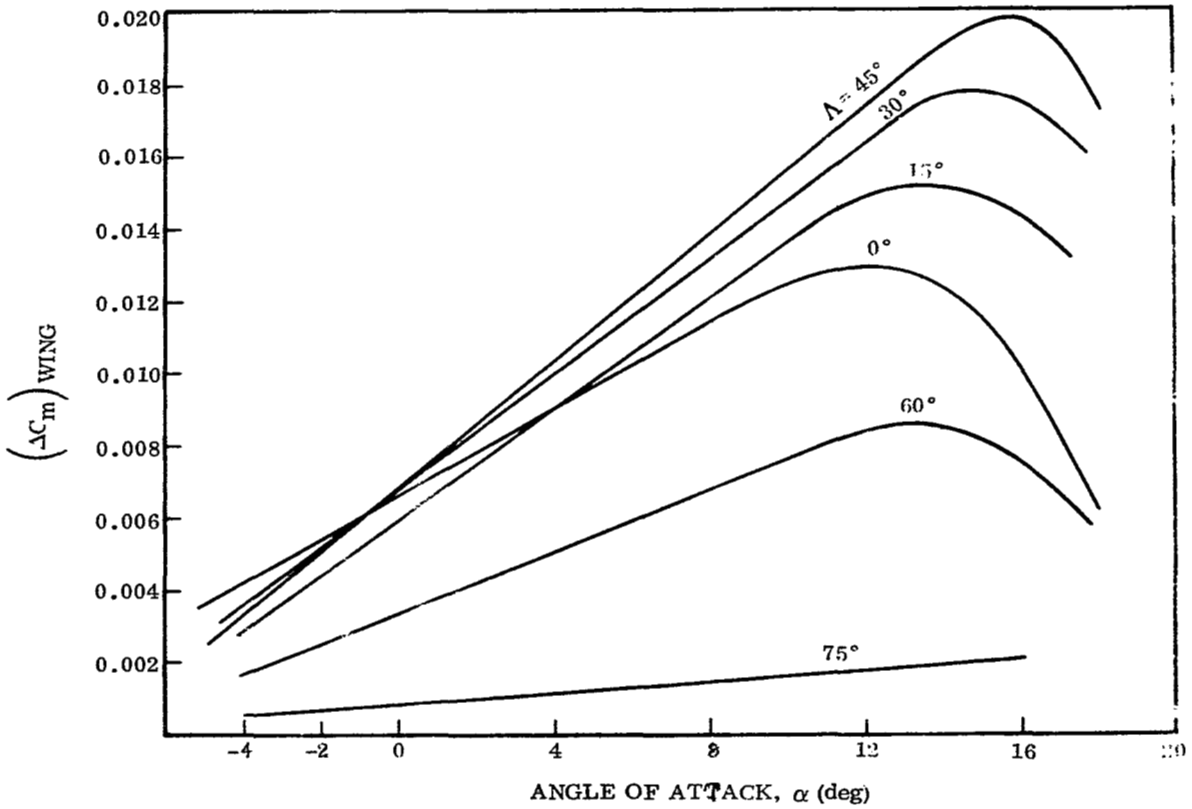

Figure 4-3. Incremental Wing Pitching Moment

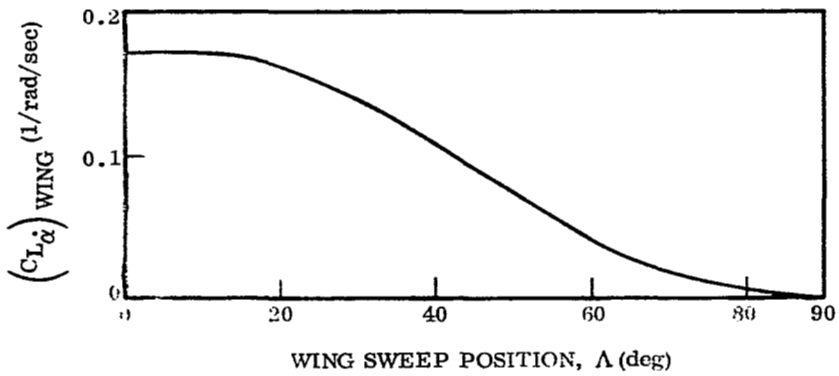

Figure 4-4. Lift Coefficient Due to Angle of Attack Rate

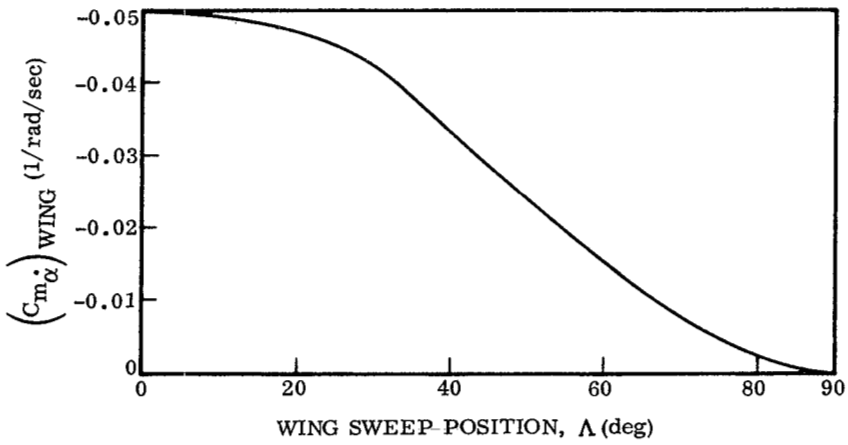

Figure 4-5. Pitching Moment Coefficient Due to Angle of Attack Rate

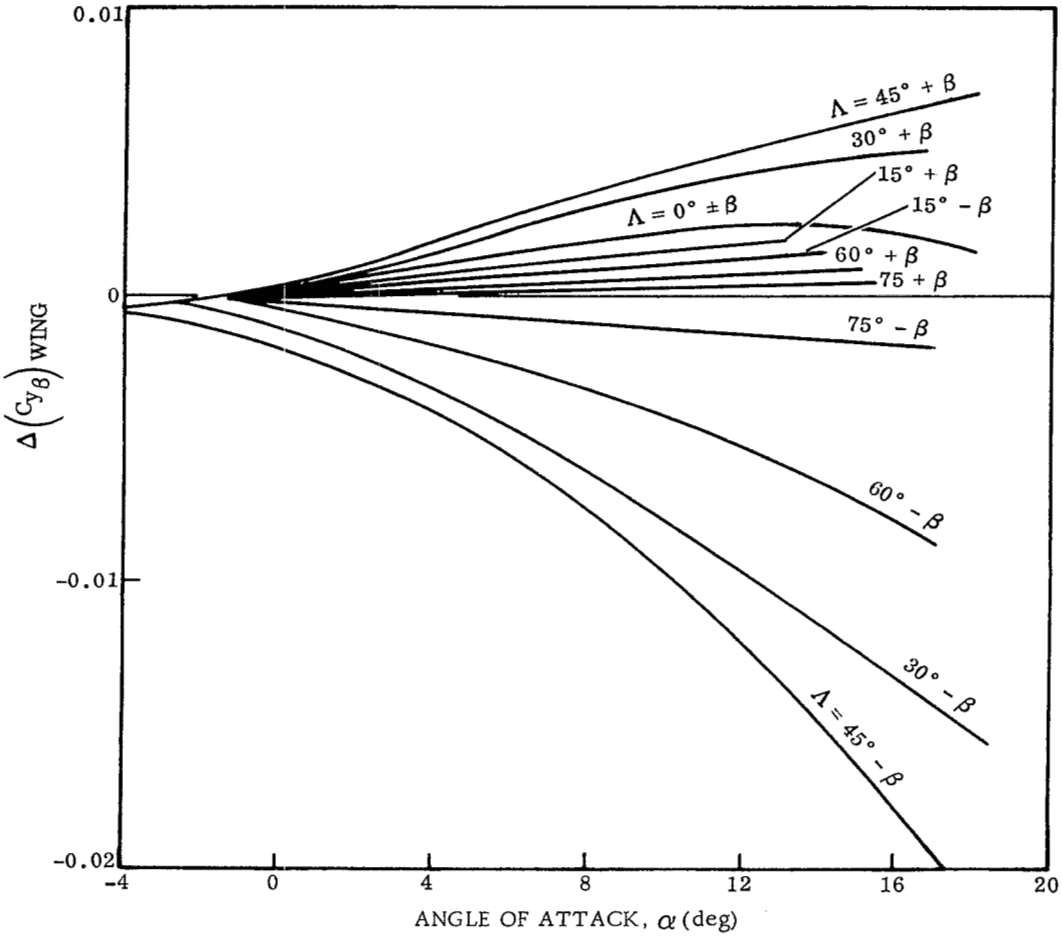

Figure 4-6. Wing Incremental Side Force Parameter Due to Side Slip

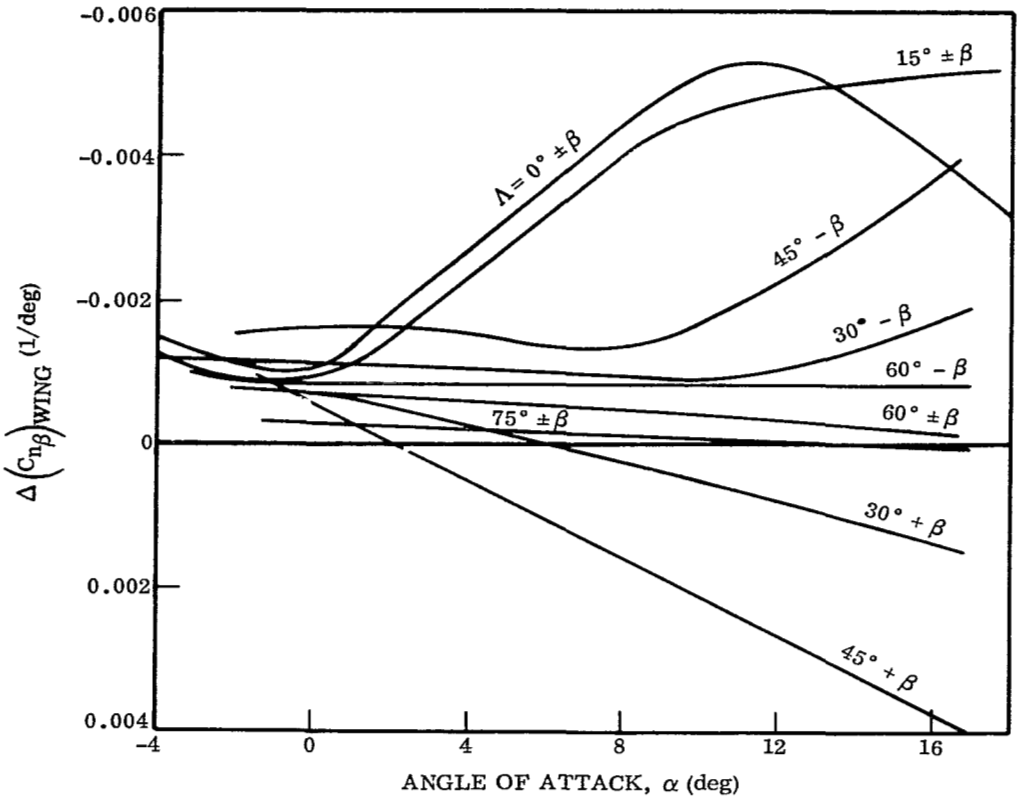

Figure 4-7. Wing Incremental Directional Stability Parameter Due to Side Slip

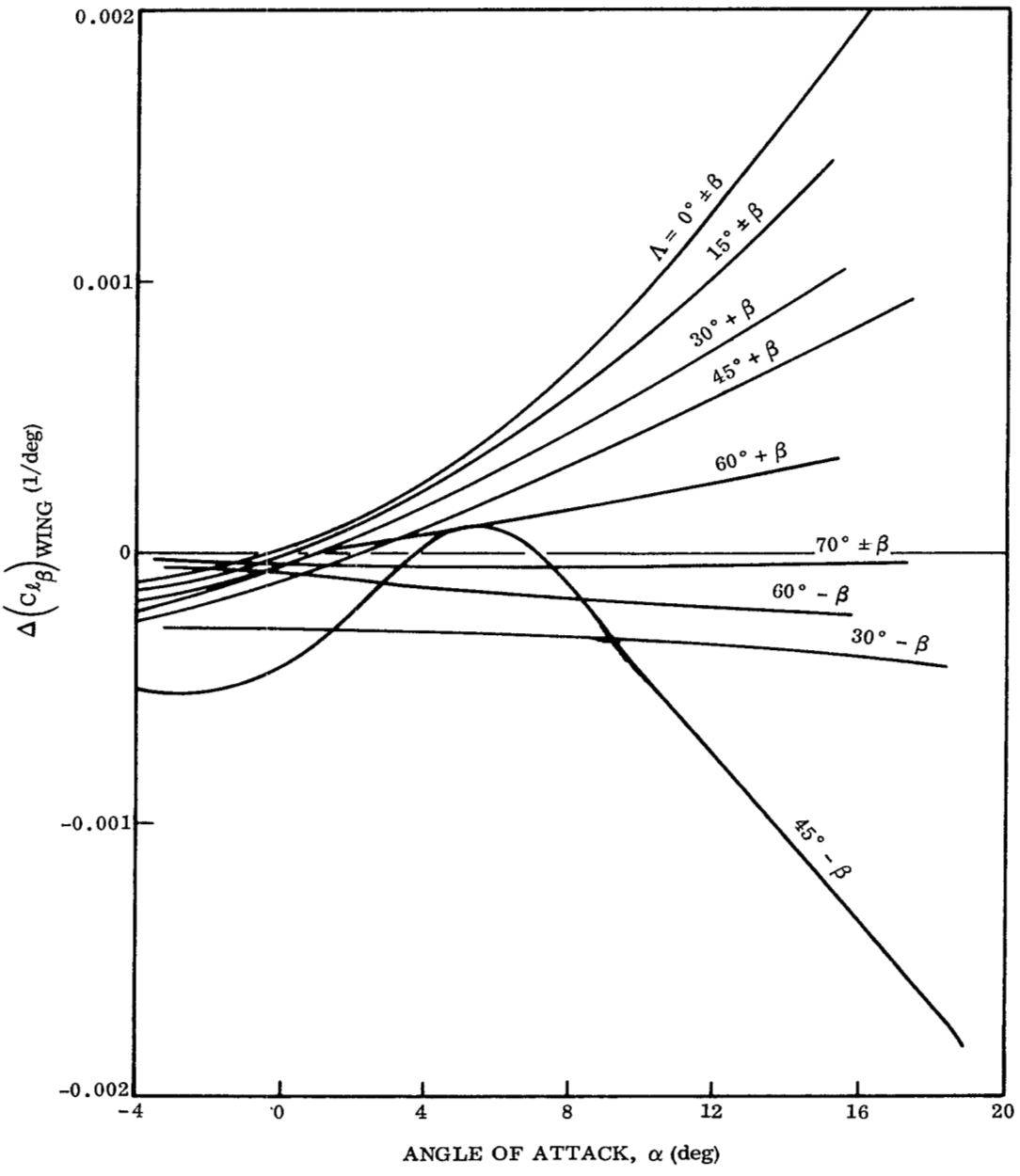

Figure 4-8. Wing Incremental Lateral Stability Parameter Due to Side Slip

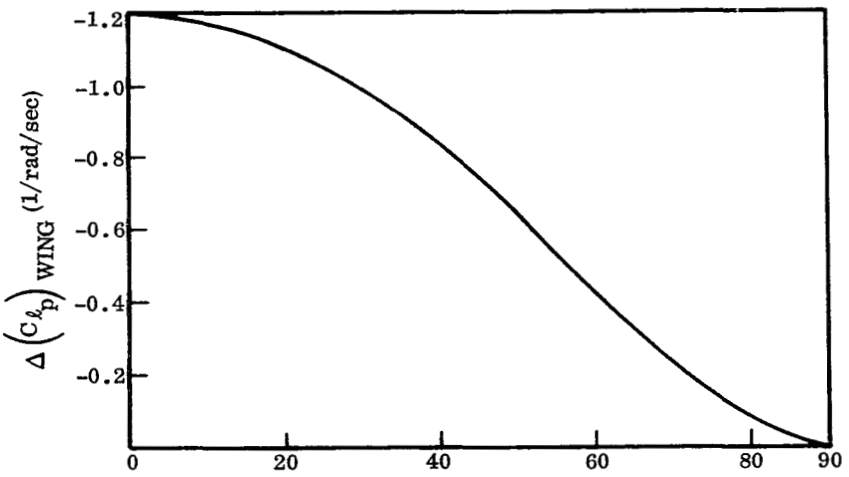

Figure 4-9. Wing Incremental Rolling Moment Coefficient Due to Rolling Velocity

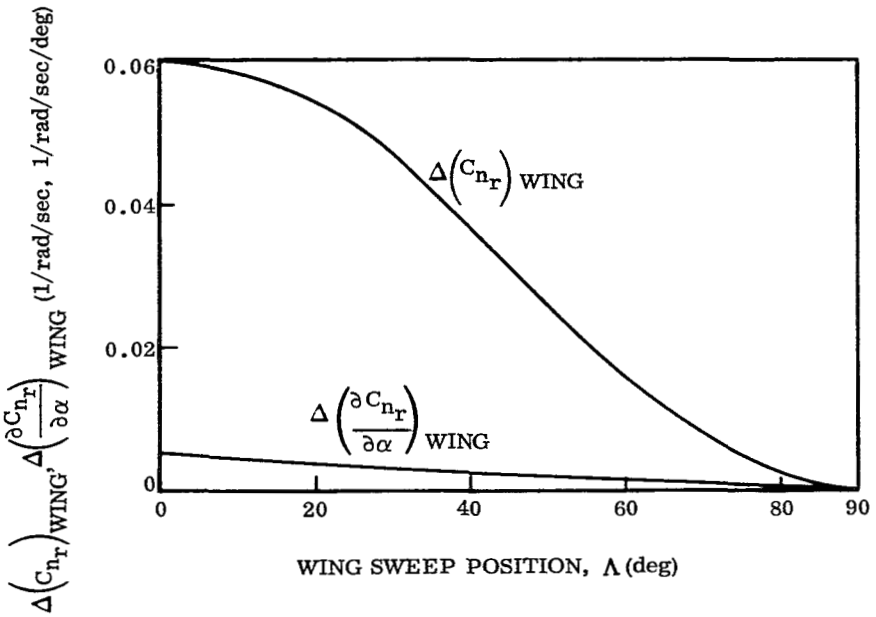

Figure 4-10. Wing Incremental Rolling Moment Coefficient Due to Yawing Velocity

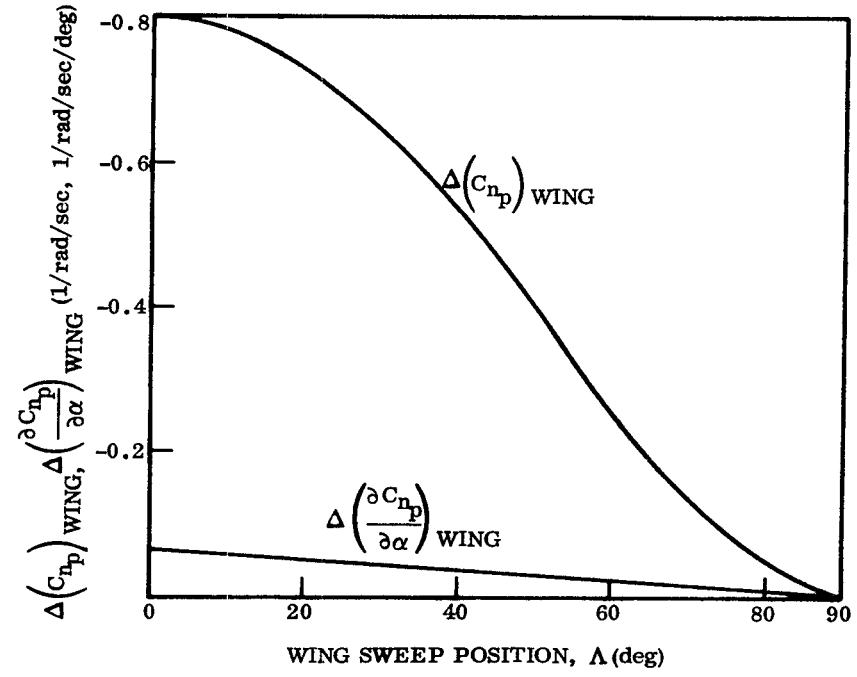

Figure 4-11. Wing Incremental Yawing Moment Coefficient Due to Rolling Velocity

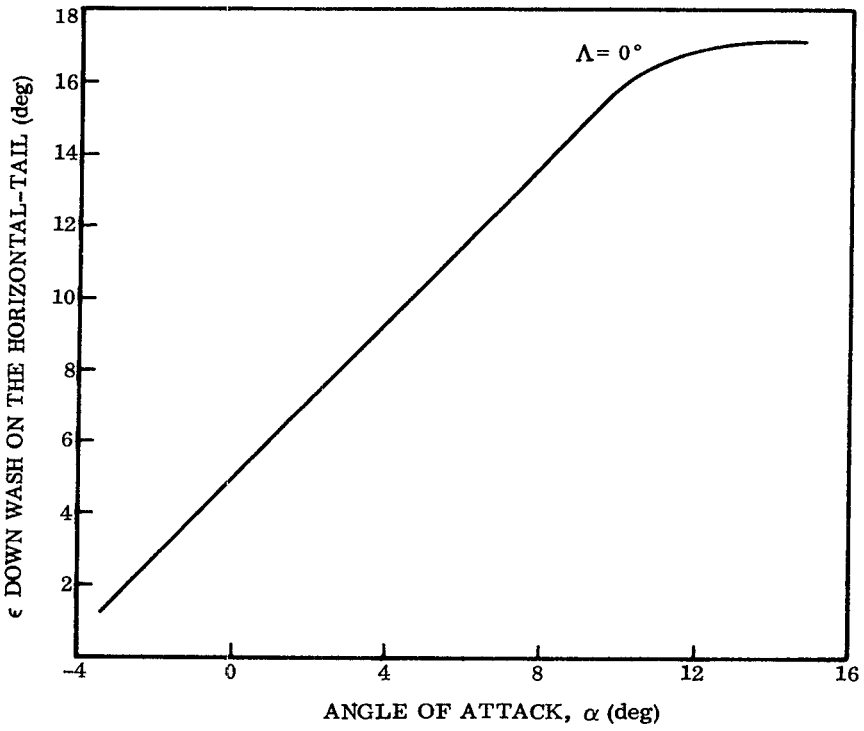

Figure 4-12. Downwash on the Horizontal Tail

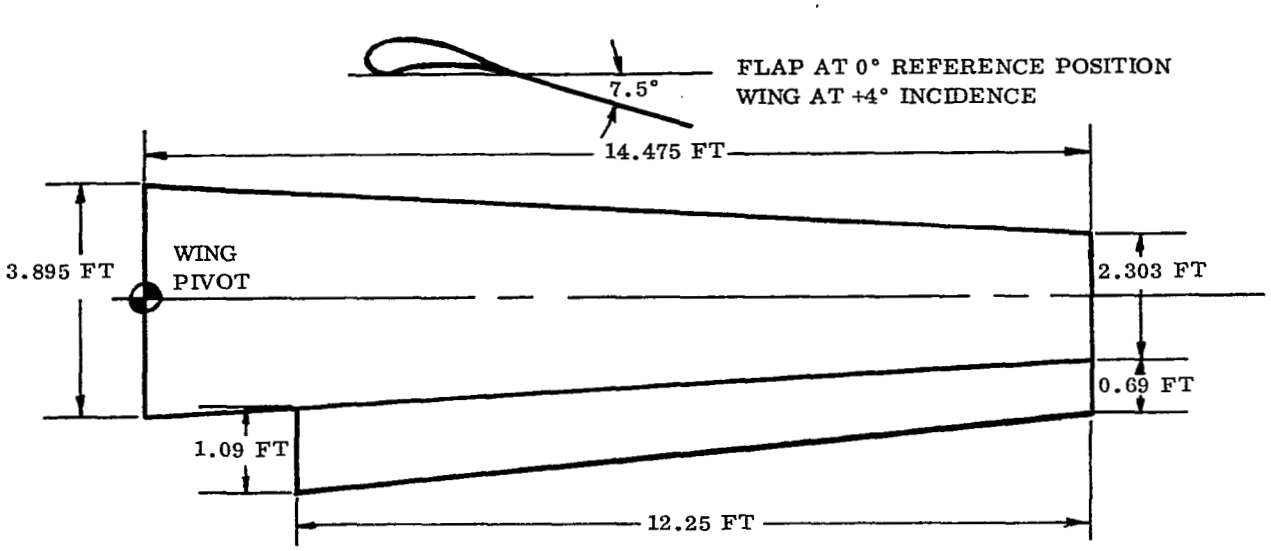

Figure 4-13. Wing Trailing-Edge Flap Configuration

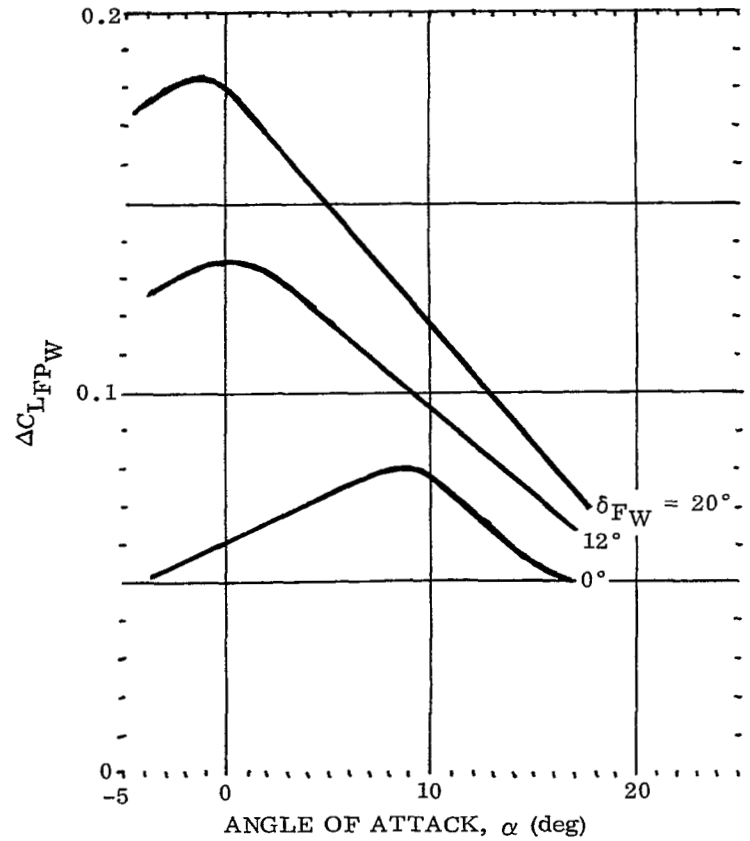

Figure 4-14. Flap Incremental Lift Coefficient

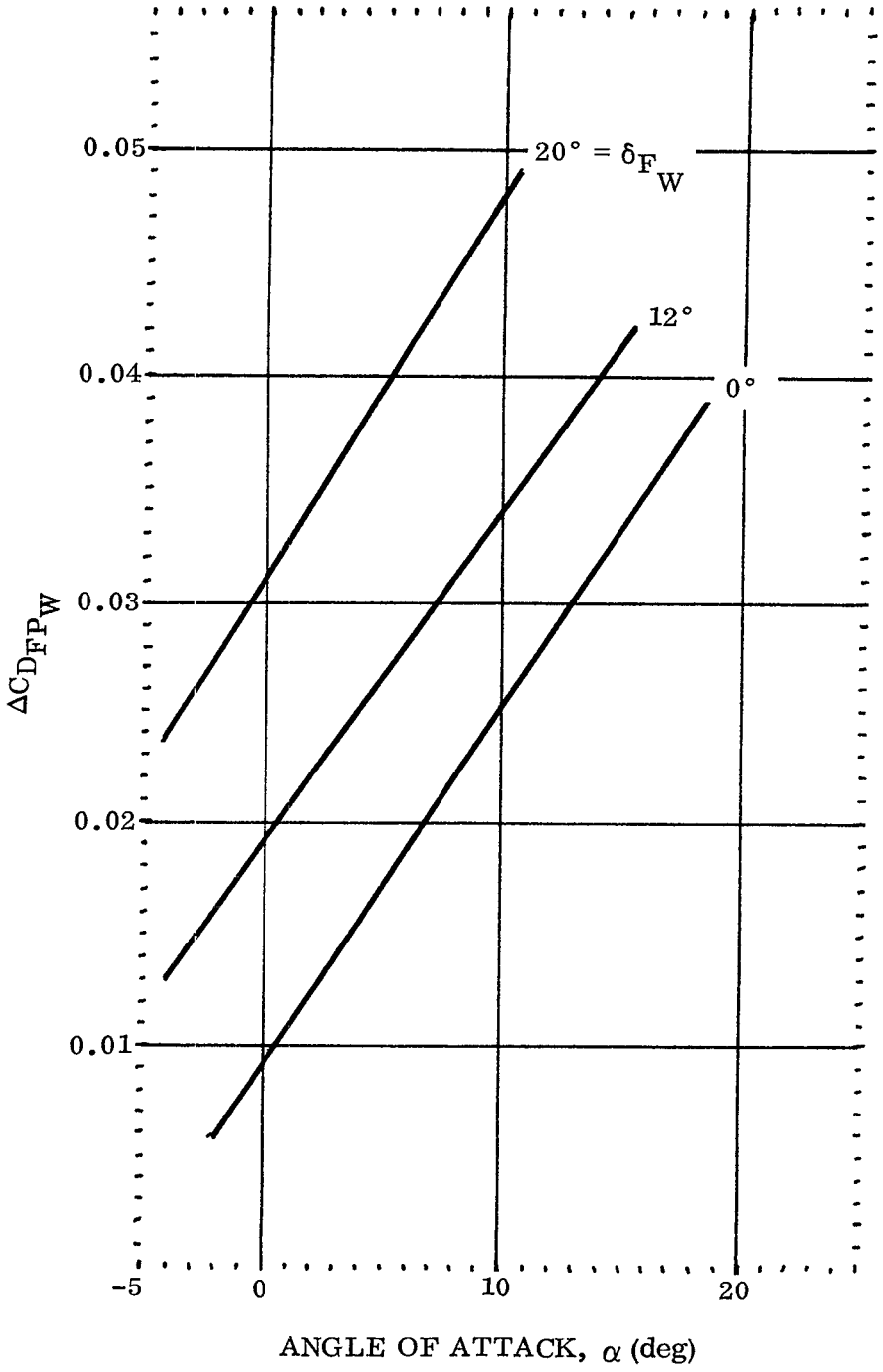

Figure 4-15. Flap Incremental Drag Coefficient

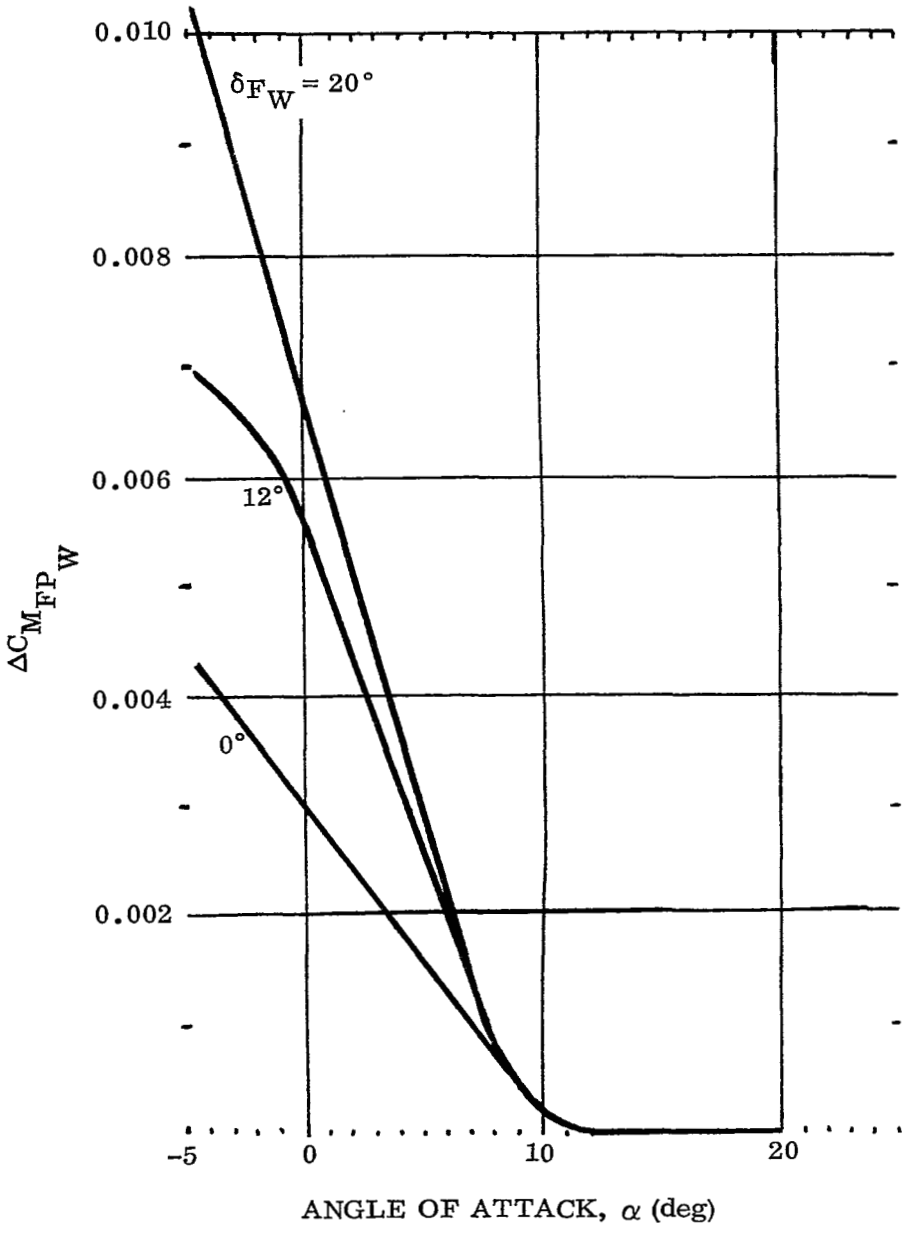

Figure 4-16. Flap Incremental Pitching Moment Coefficient

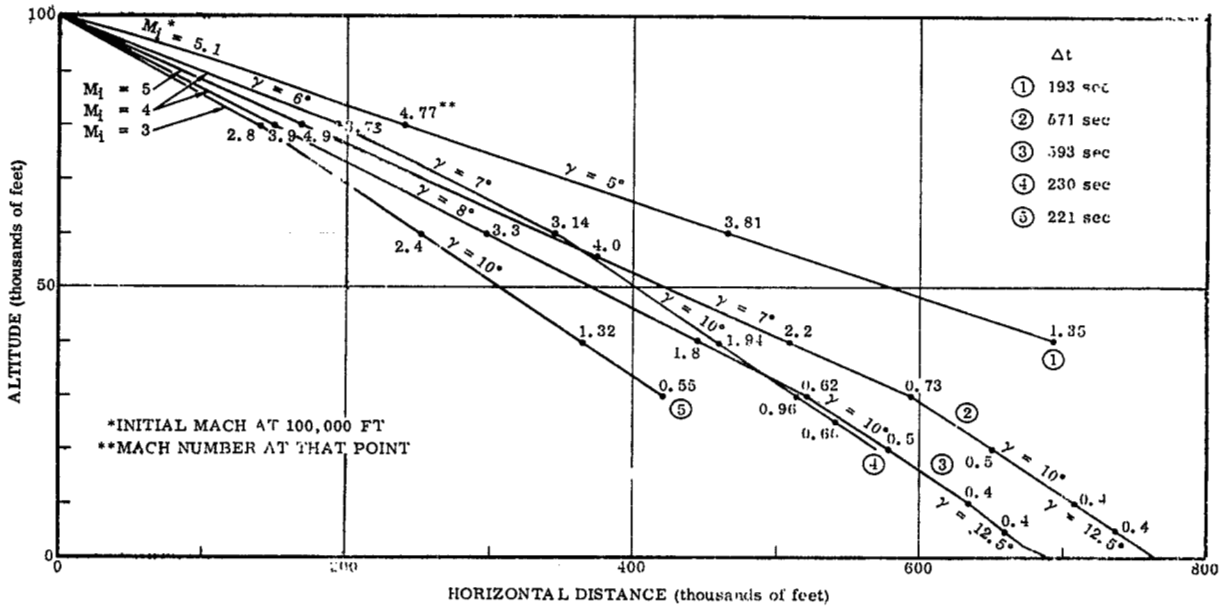

Figure 7-1. Spacial Histories of Simulated Flights

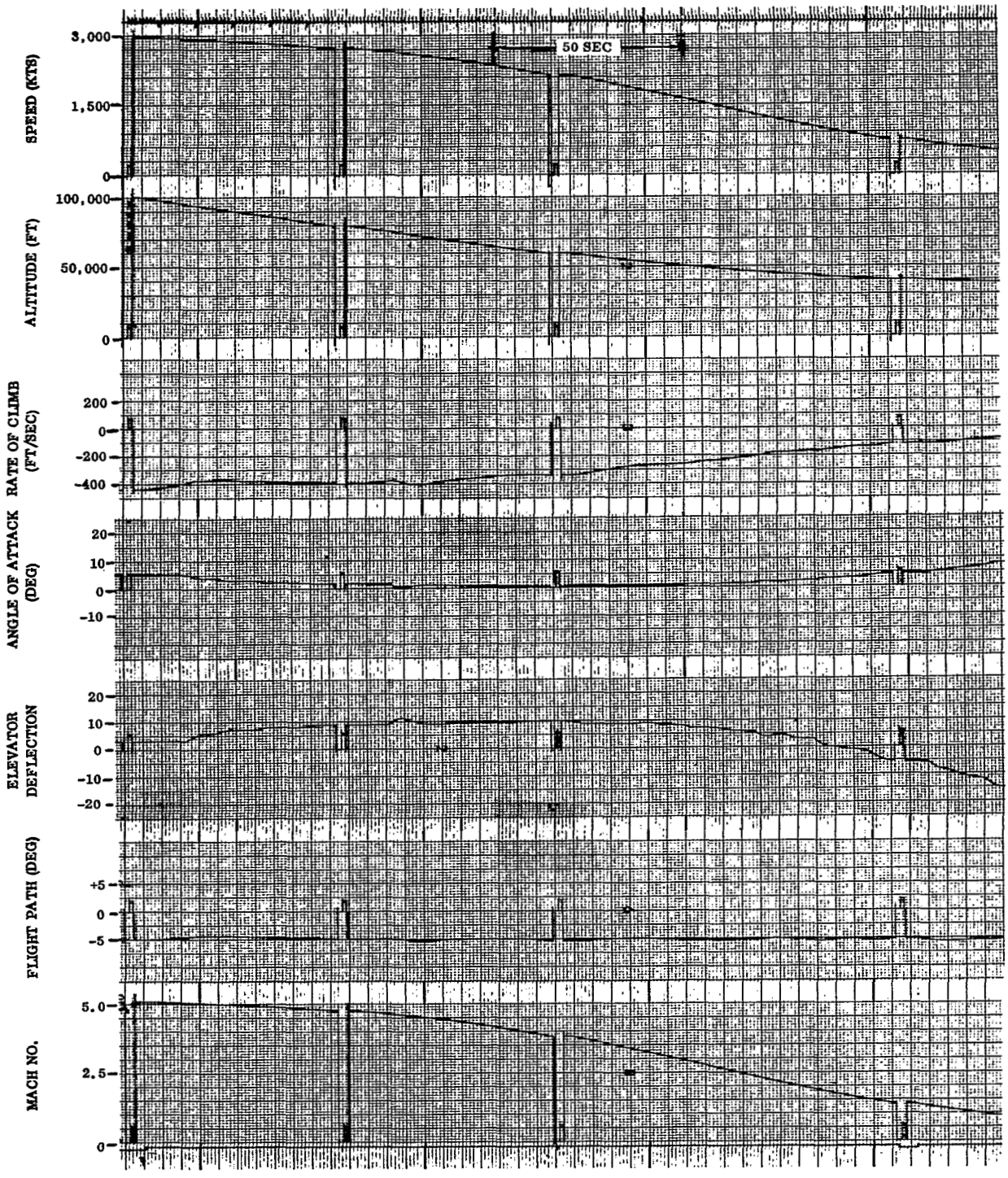

Figure 7-2. Time Histories of Dynamic Parameter for an Initial Mach of 5

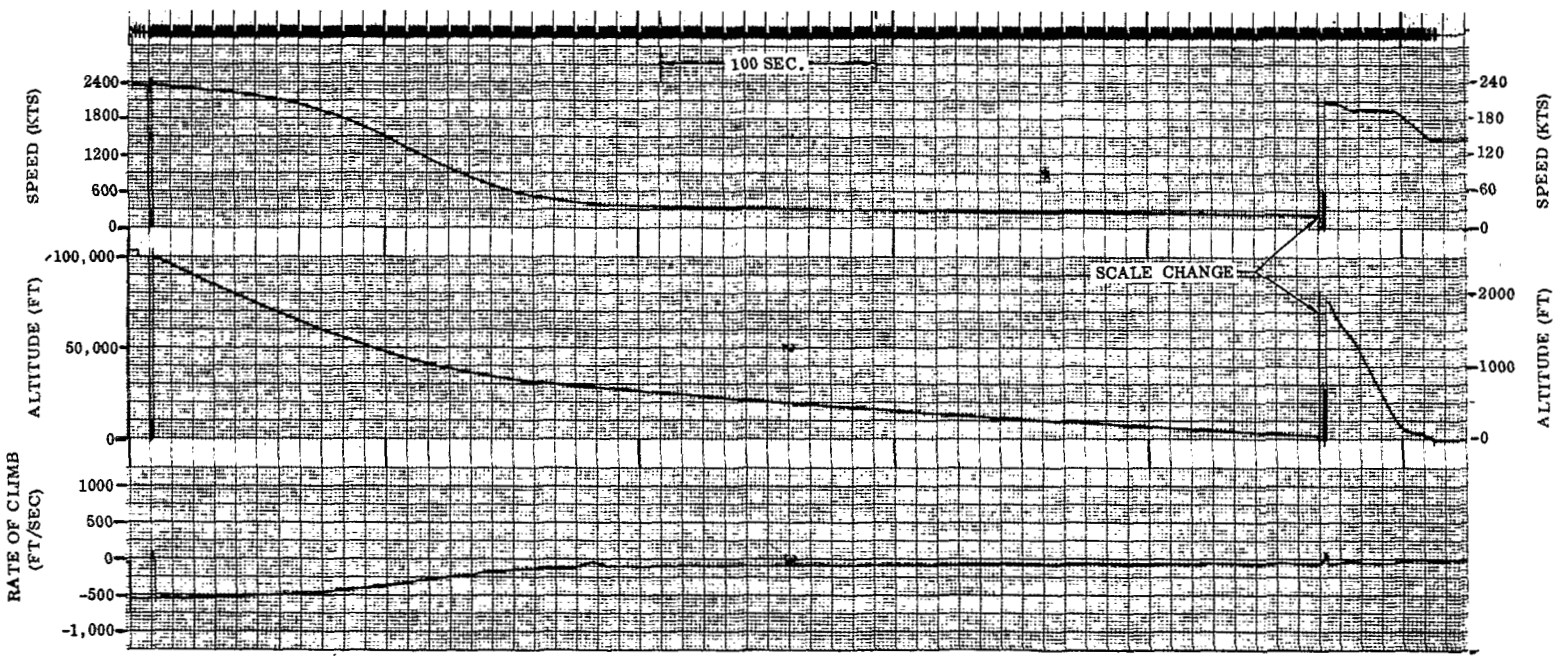

Figure 7-3. Time Histories of Dynamic Parameter for an Initial Mach of 4 (Sheet 1 of 2)

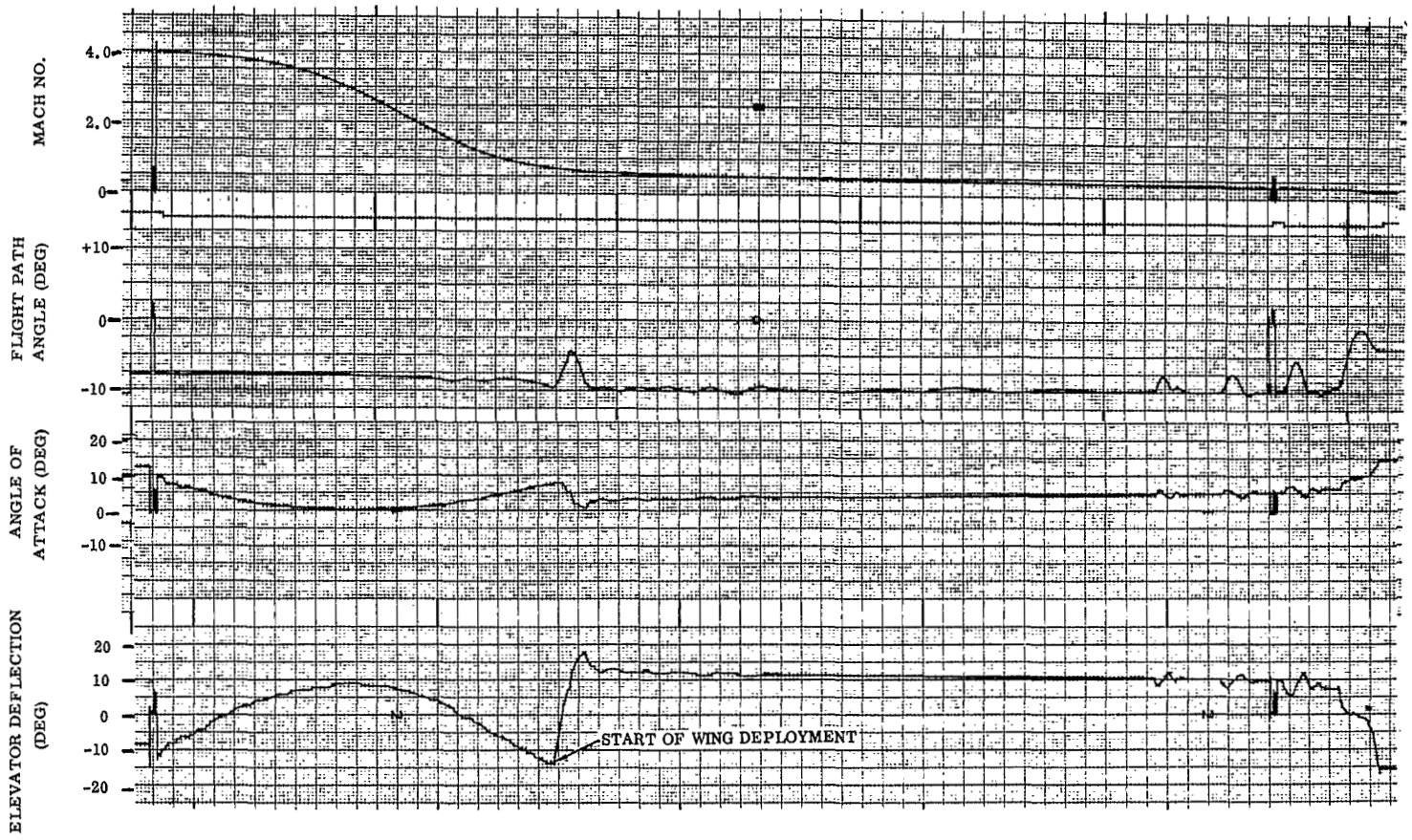

Figure 7-3. Time Histories of Dynamic Parameter for an Initial Mach of 4 (Sheet 2 of 2)

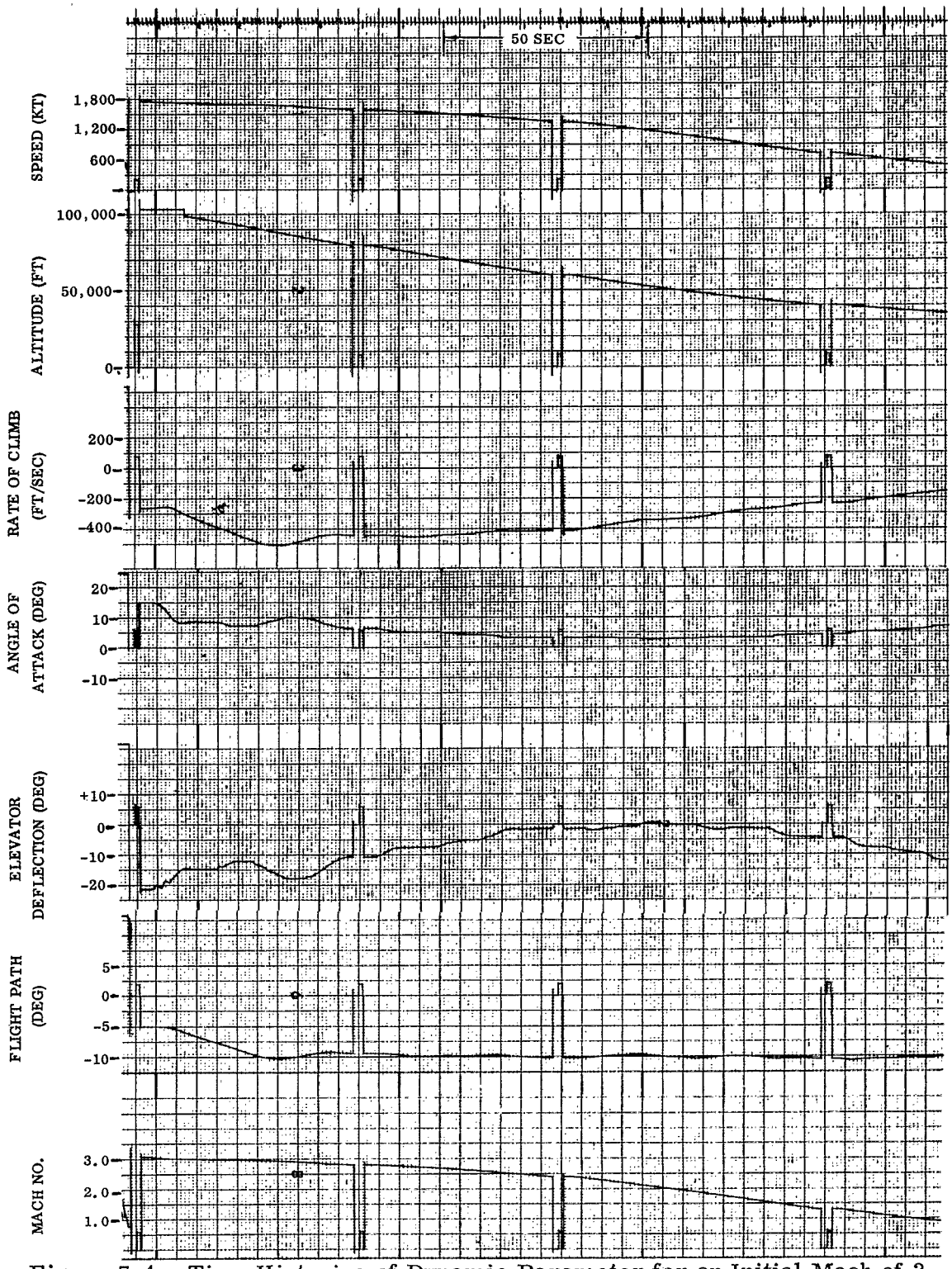

Figure 7-4. Time Histories of Dynamic Parameter for an Initial Mach of 3

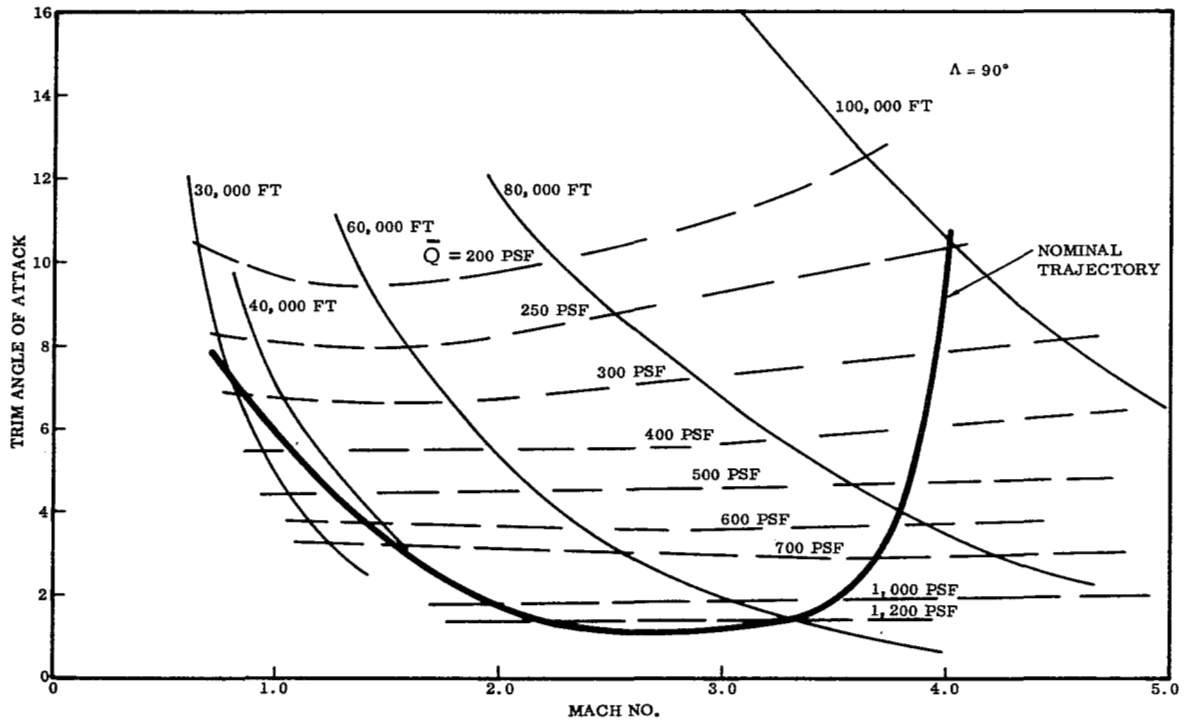

Figure 7-5. Trim Angle of Attack Requirements $\Lambda = 90°$

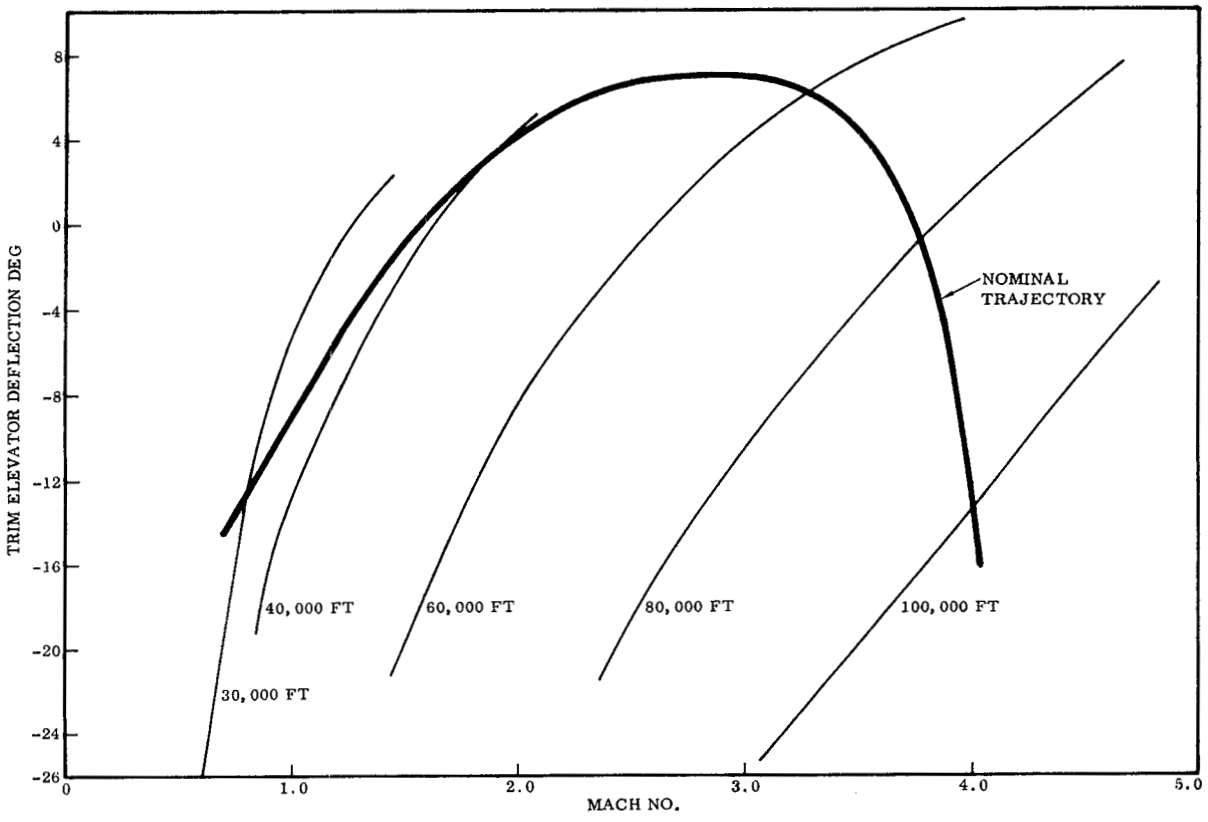

Figure 7-6. Trim Elevator Deflection Requirements $\Lambda = 90°$

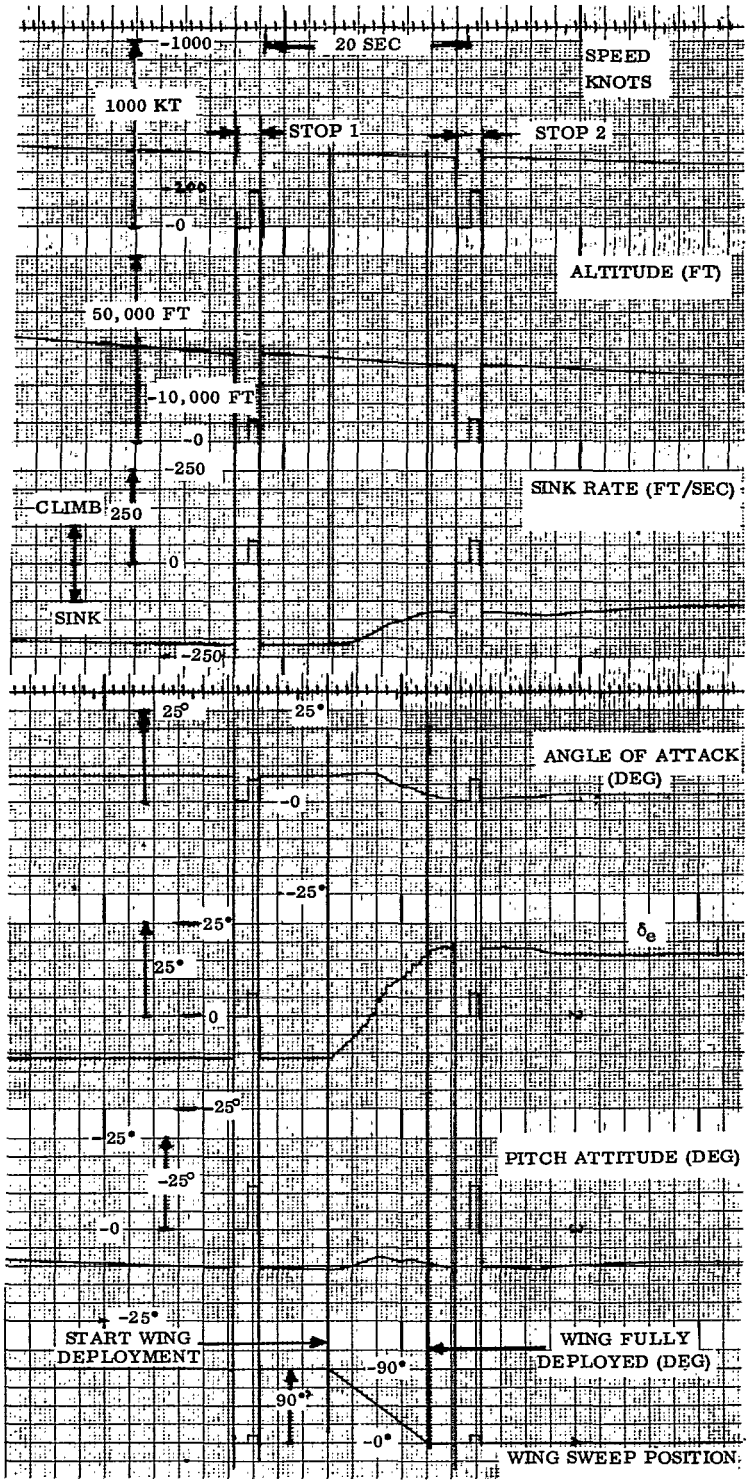

Figure 7-7. Wing Deployment with Pilot Input (10°/sec Sweep Rate)

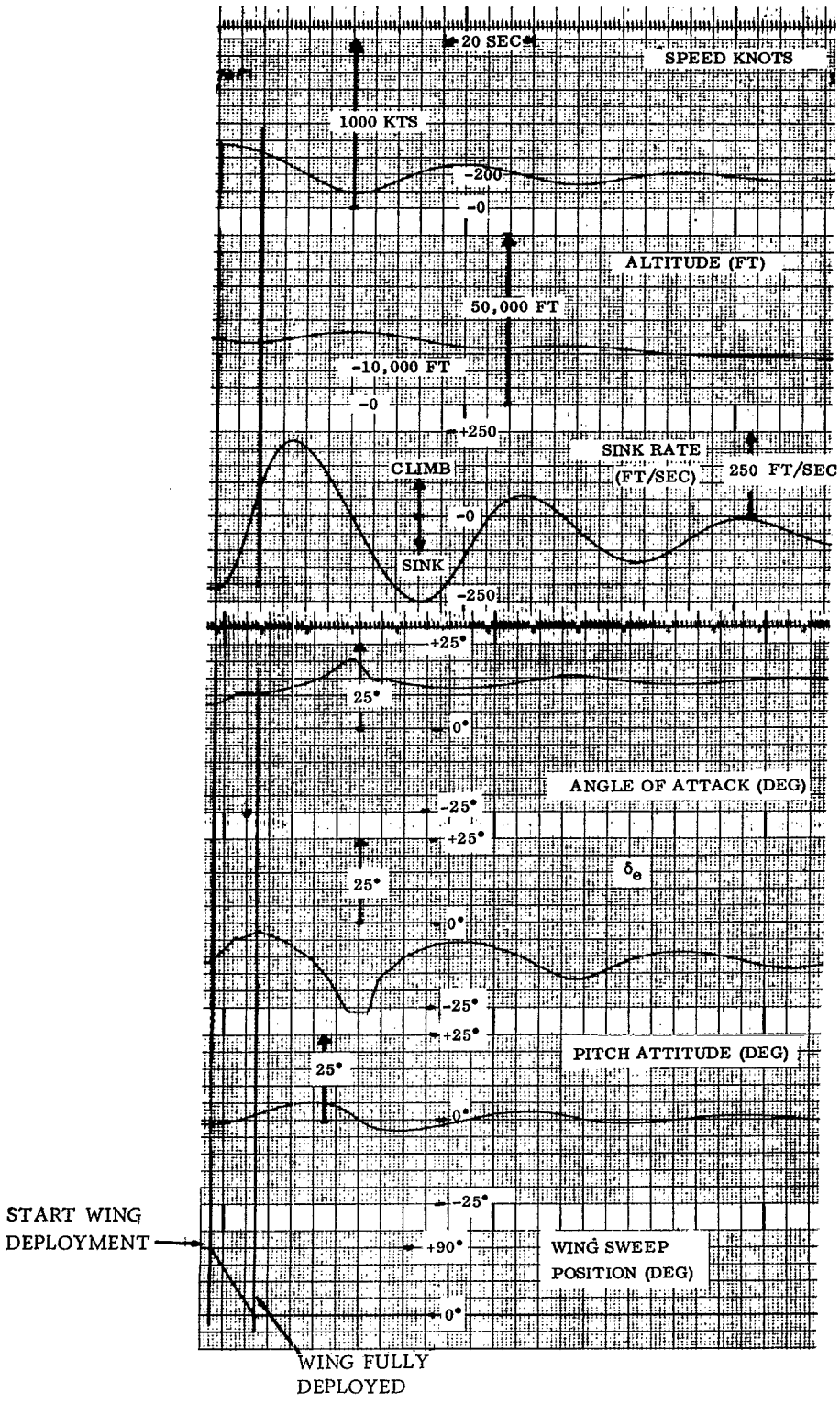

Figure 7-8. Wing Deployment without Pilot Input (10°/sec Sweep Rate)

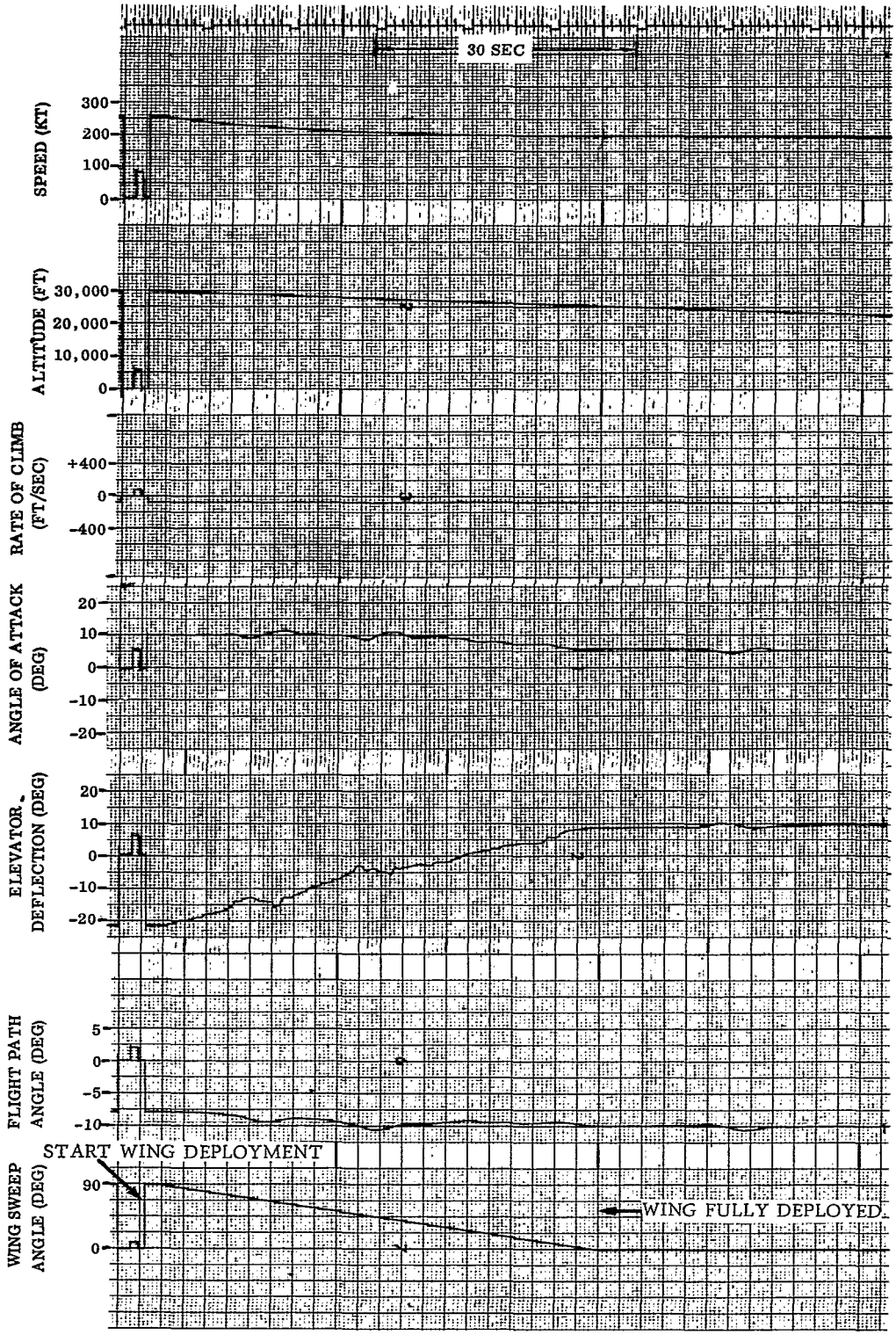

Figure 7-9. Wing Deployment with Pilot Input (2°/sec Sweep Rate)

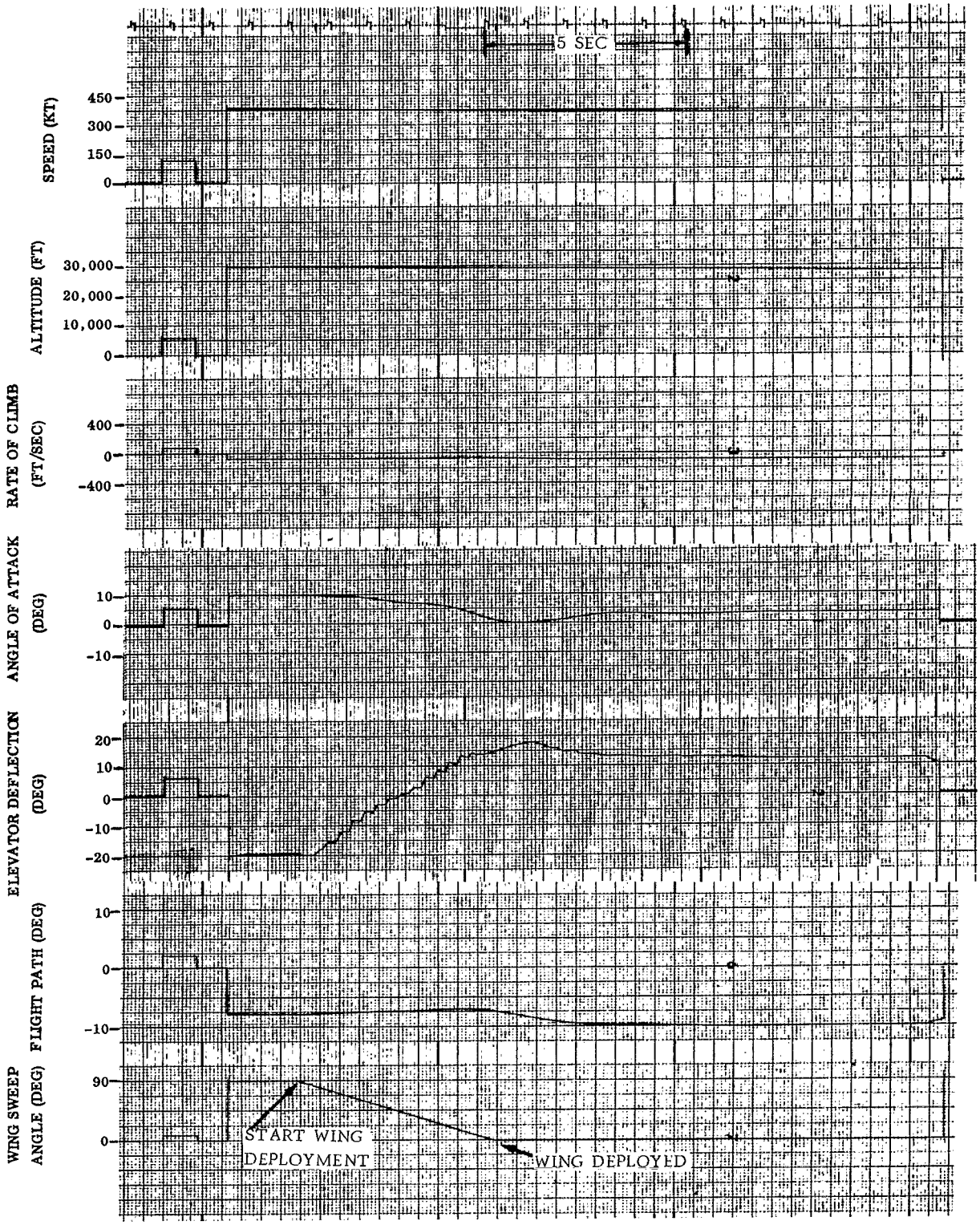

Figure 7-10. Wing Deployment with Pilot Input (20°/sec Sweep Rate)

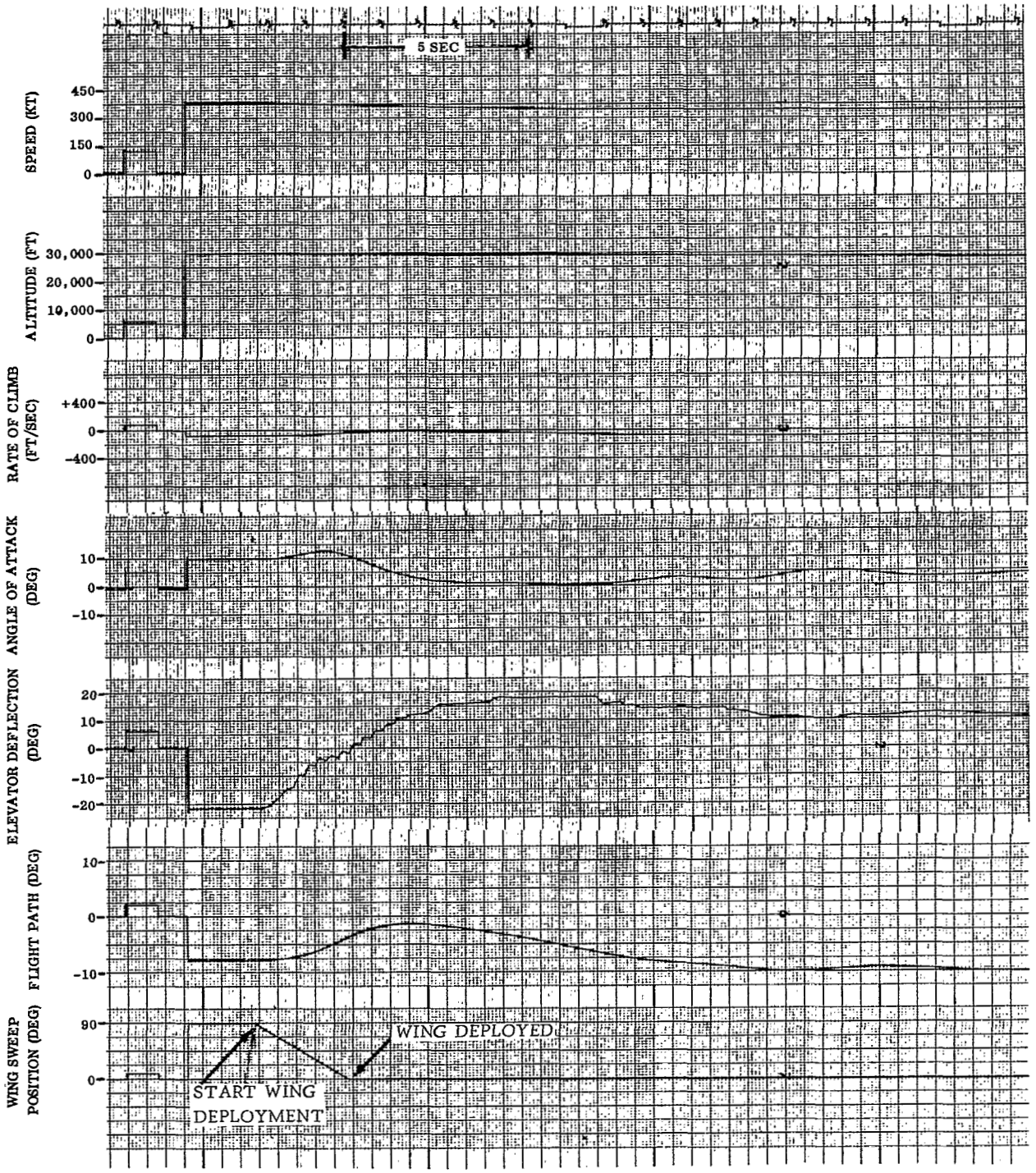

Figure 7-11. Wing Deployment with Pilot Input (40°/sec Sweep Rate)

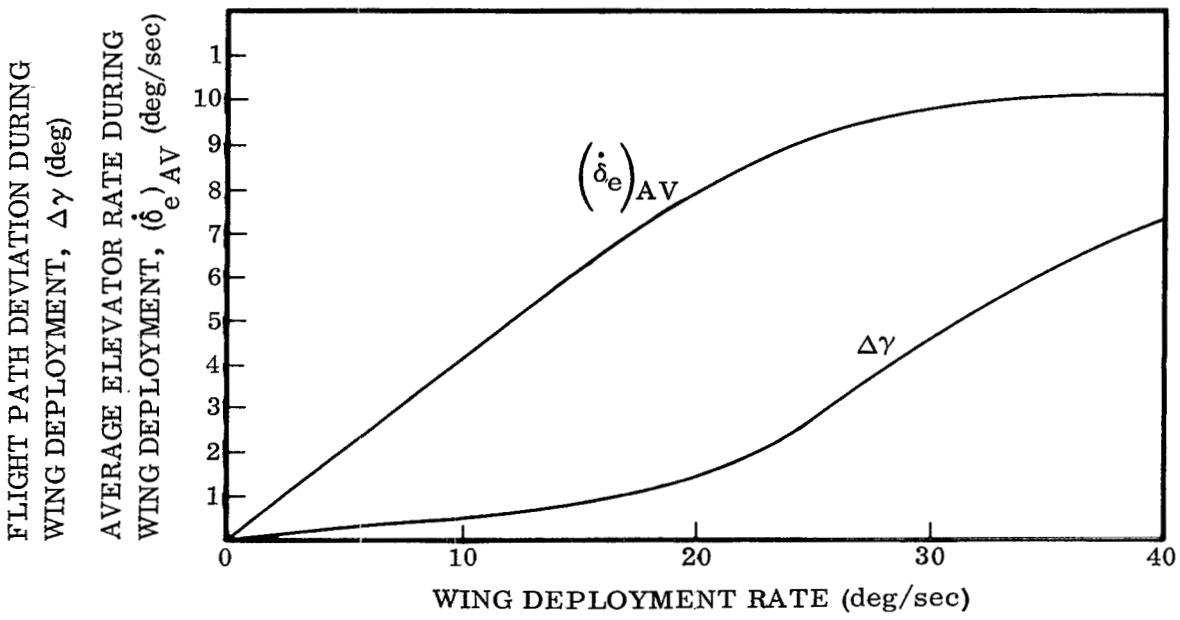

Figure 7-12. Elevator Deflection Rates Required During Wing Deployment

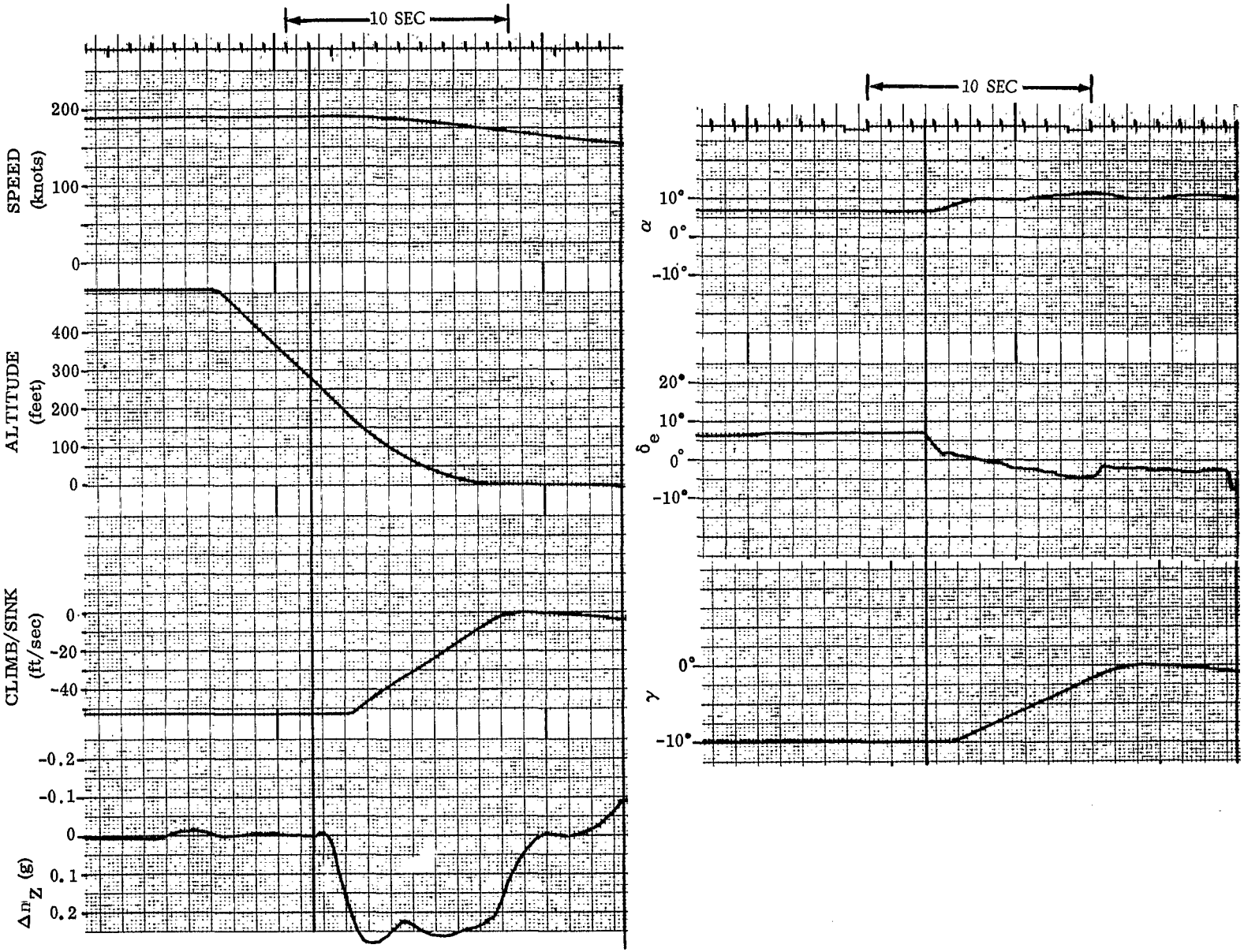

Figure 7-13. Time Histories of Dynamic Parameter During Landing without Flaps

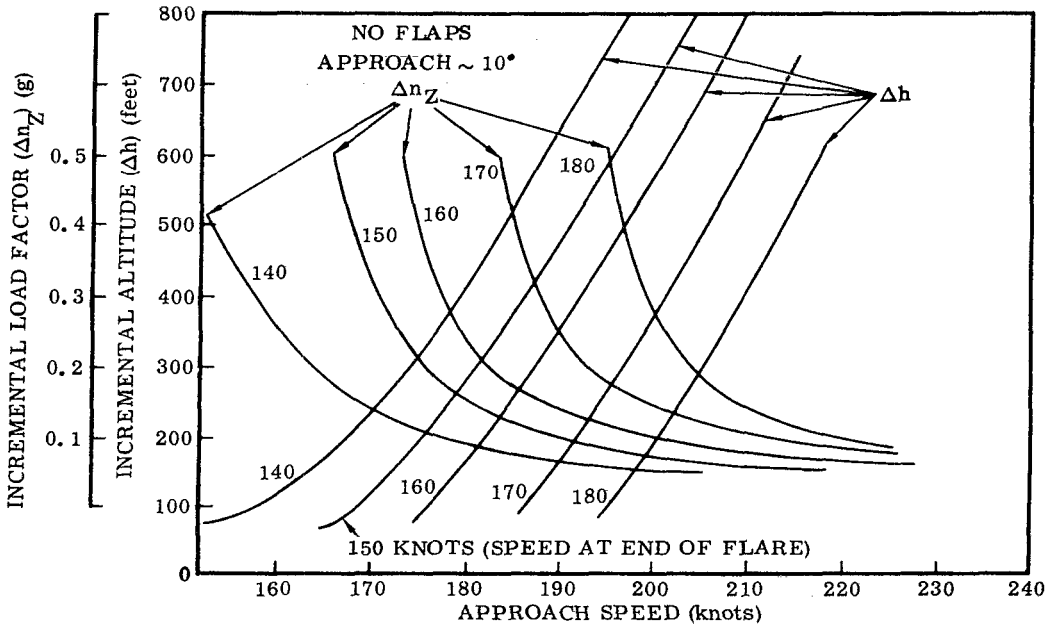

Figure 7-14. Summary of Landing Characteristics without Flaps

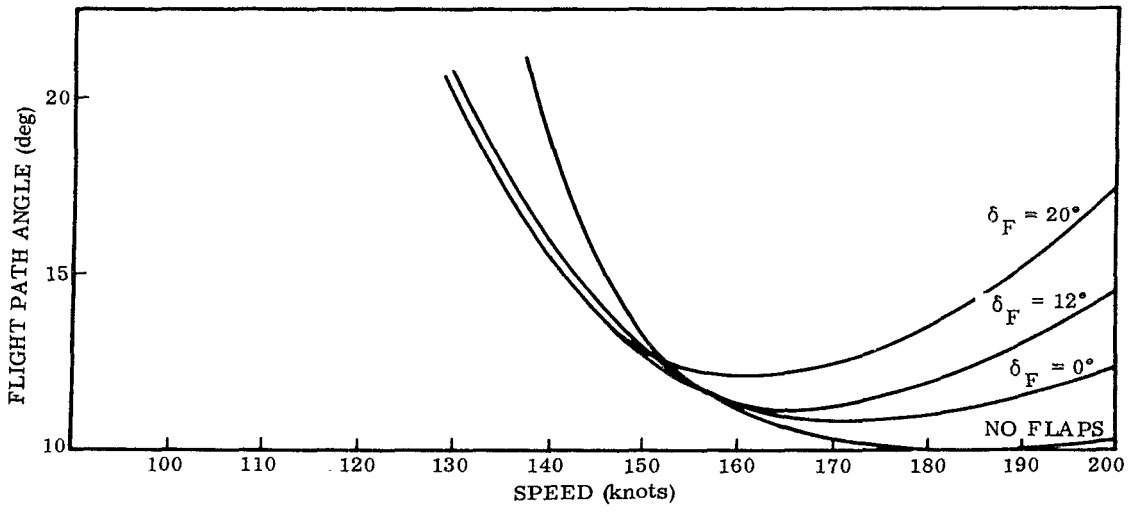

Figure 7-15. Approach Glide Angles with and without Flaps

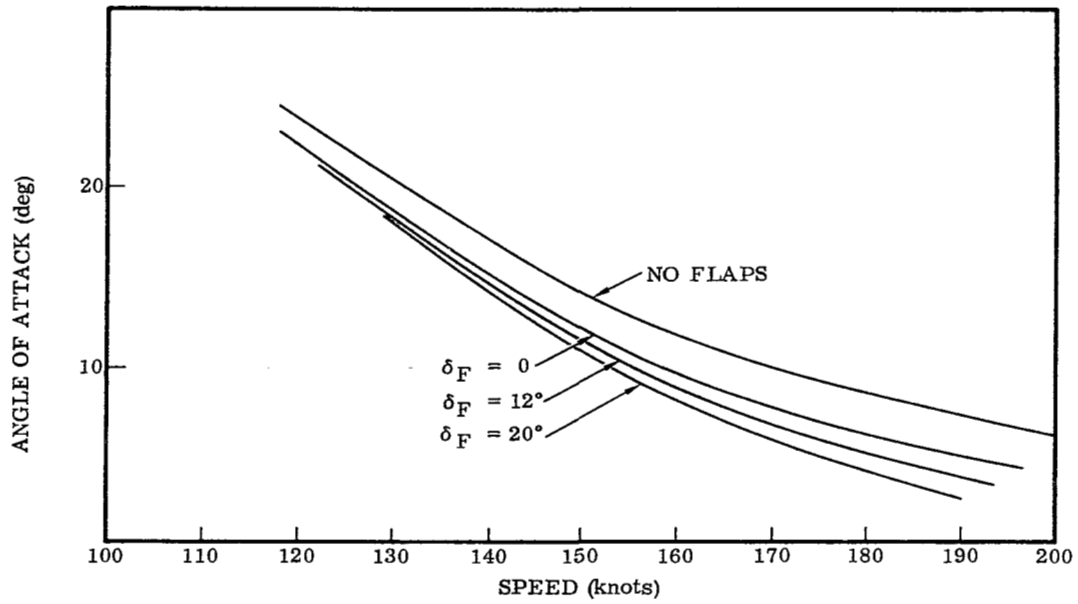

Figure 7-16. Trim Angle of Attack for Landing Approach

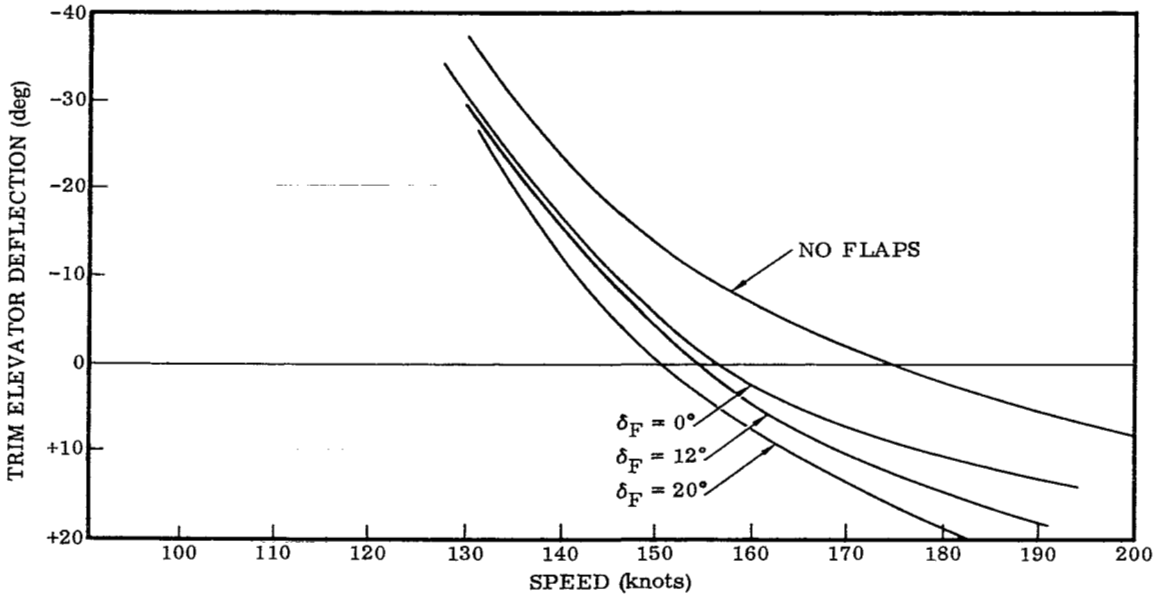

Figure 7-17. Trim Elevator Deflections for Landing Approach with and without Flaps

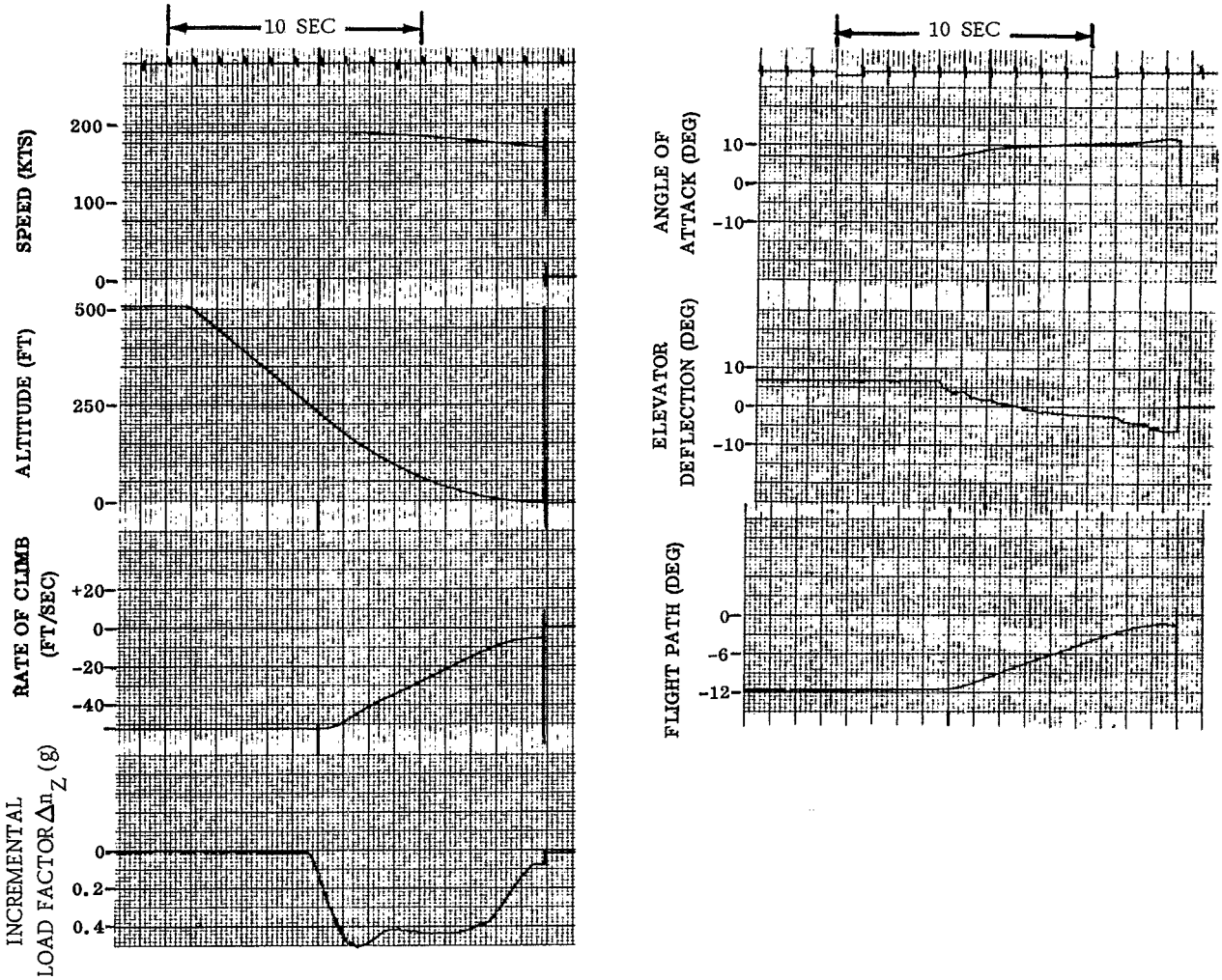

Figure 7-18. Time Histories of Various Dynamic Parameters During Landing with Flaps

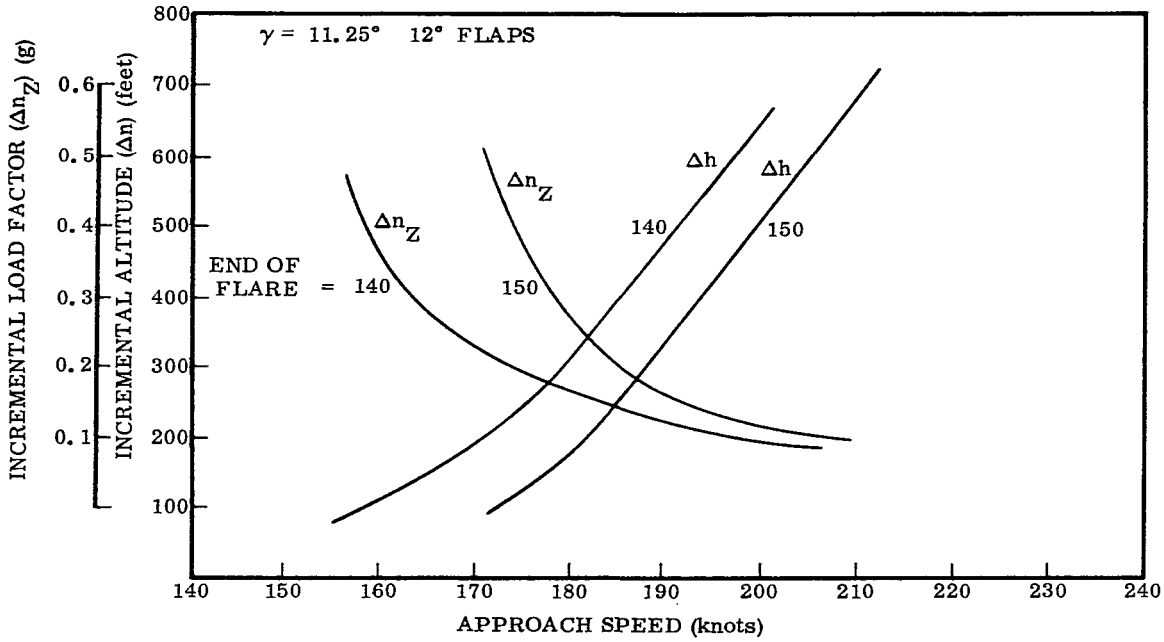

Figure 7-19. Summary of Landing Characteristics with 12° of Flaps

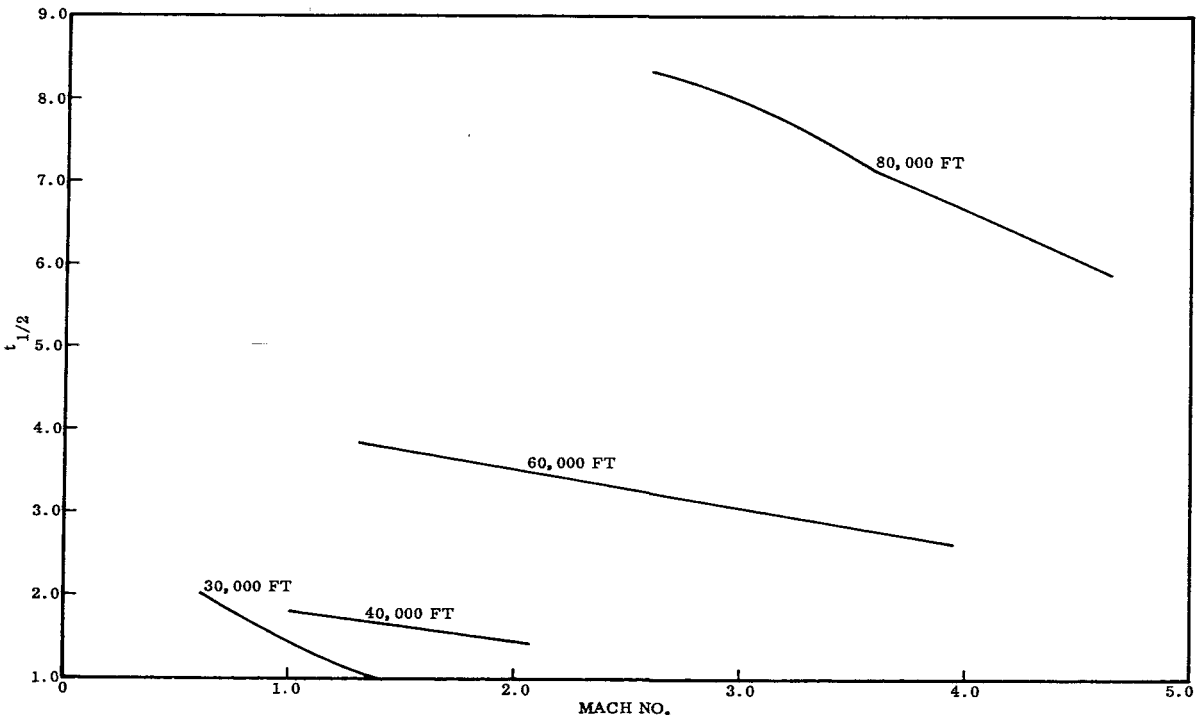

Figure 7-20. Wing Stowed Longitudinal Characteristics (Unaugmented)

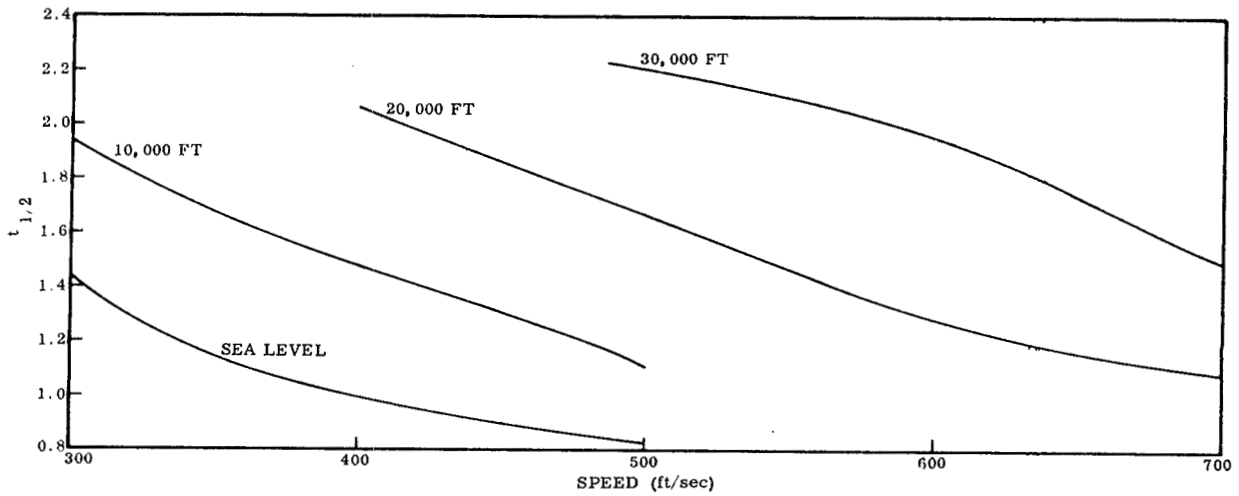

Figure 7-21. Wing Deployed Longitudinal Characteristics (Unaugmented)

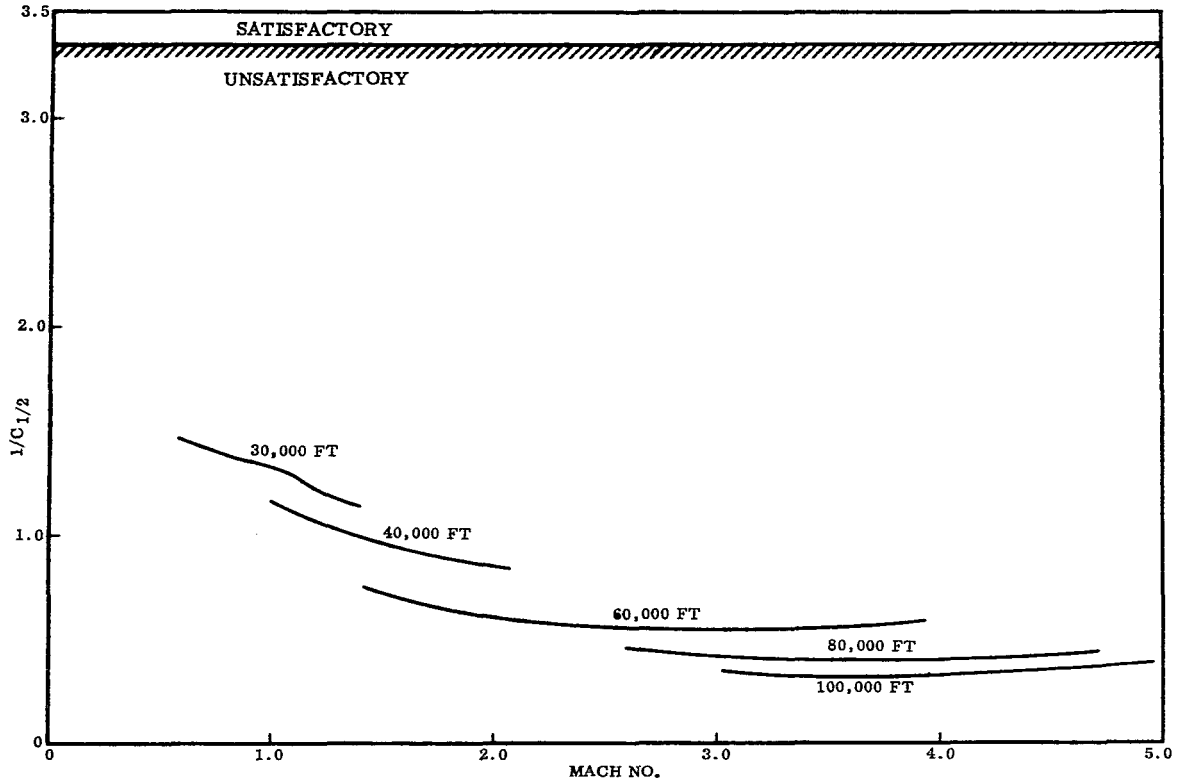

Figure 7-22. Wing Stowed Longitudinal Damping Characteristics (Unaugmented)

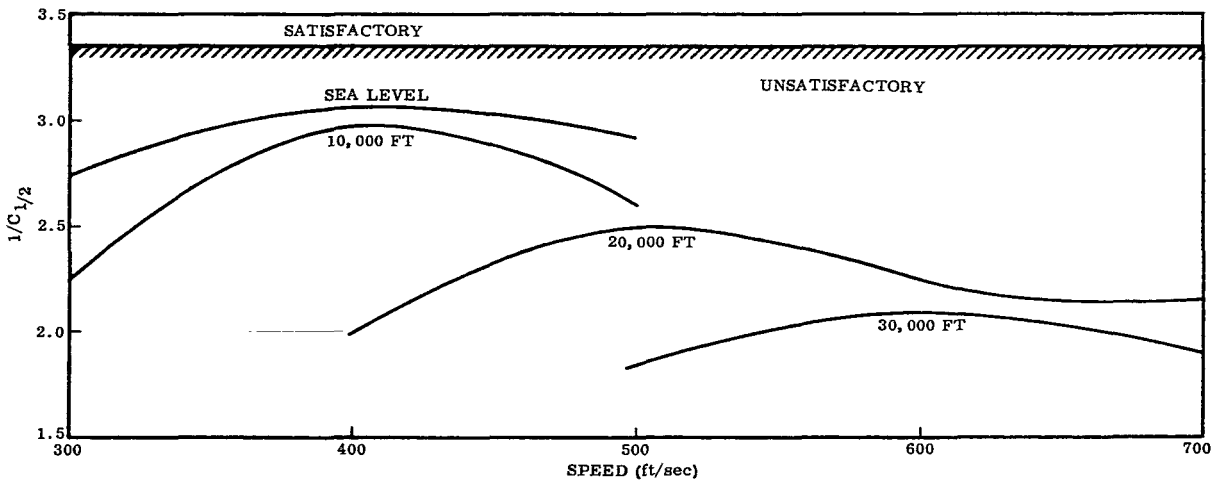

Figure 7-23. Wing Deployed Longitudinal Damping Characteristics (Unaugmented)

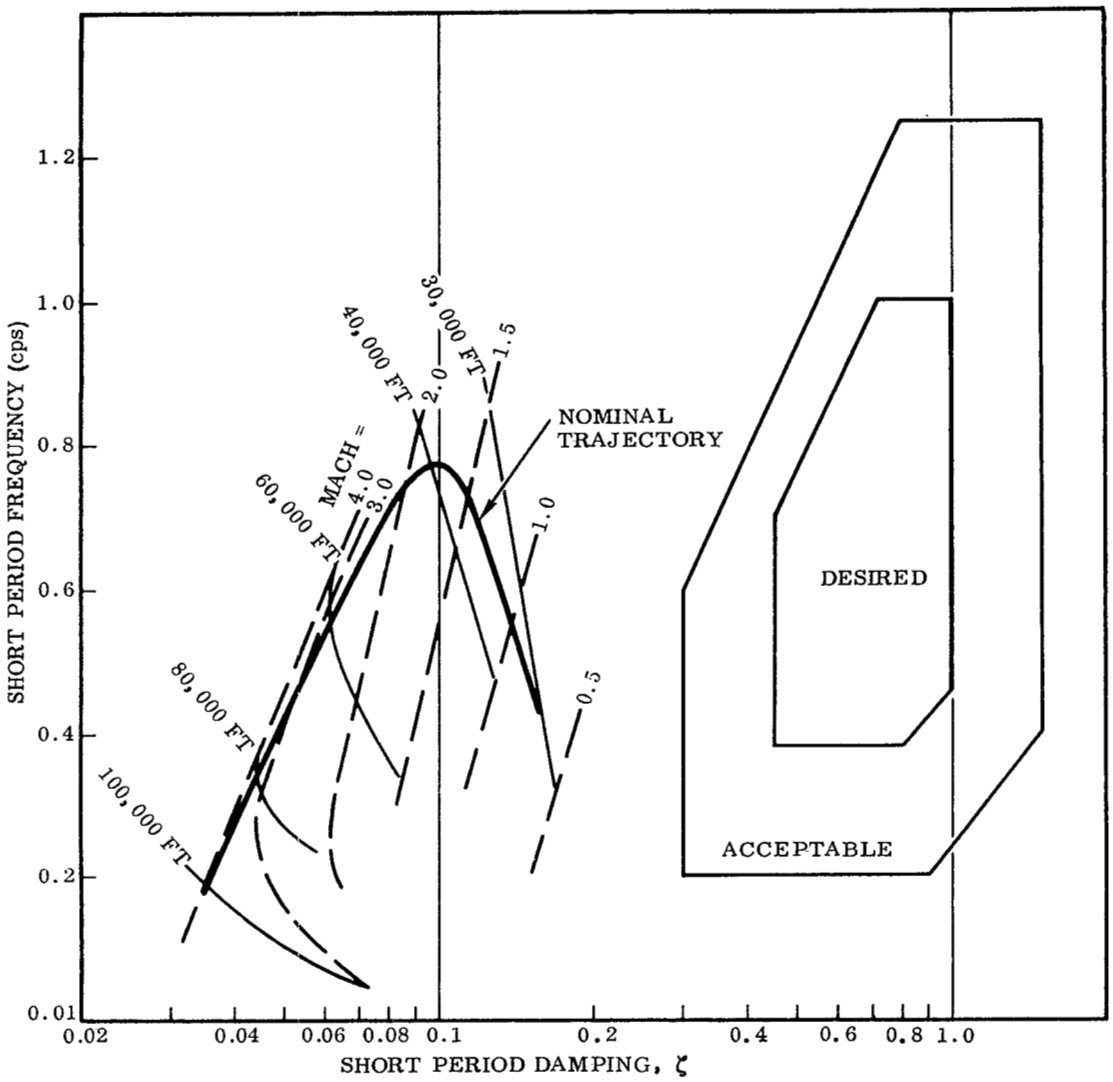

Figure 7-24. Longitudinal Handling Qualities Compared to Specified Entry Vehicle Characteristics (Unaugmented)

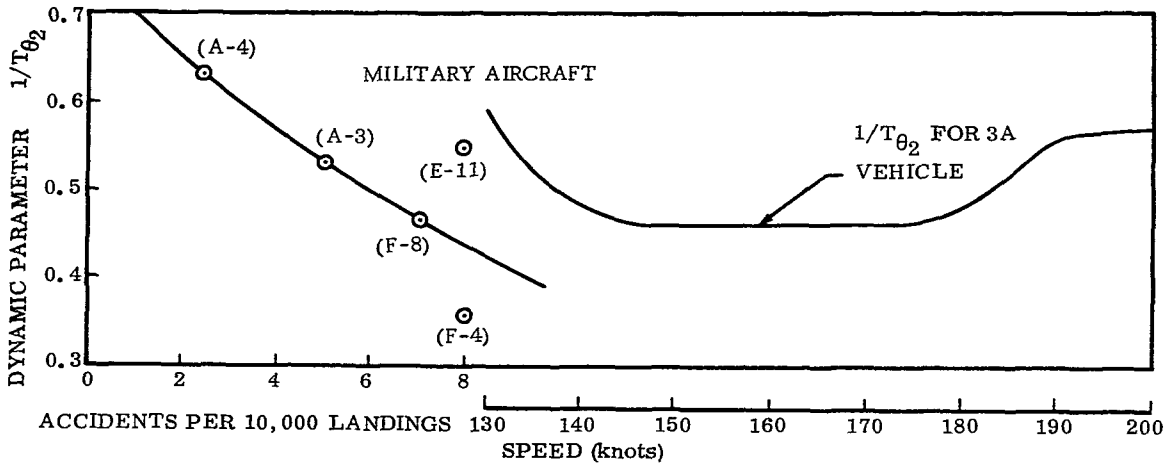

Figure 7-25. Accident Rates as Function of the Parameter $T_{\theta 2}$

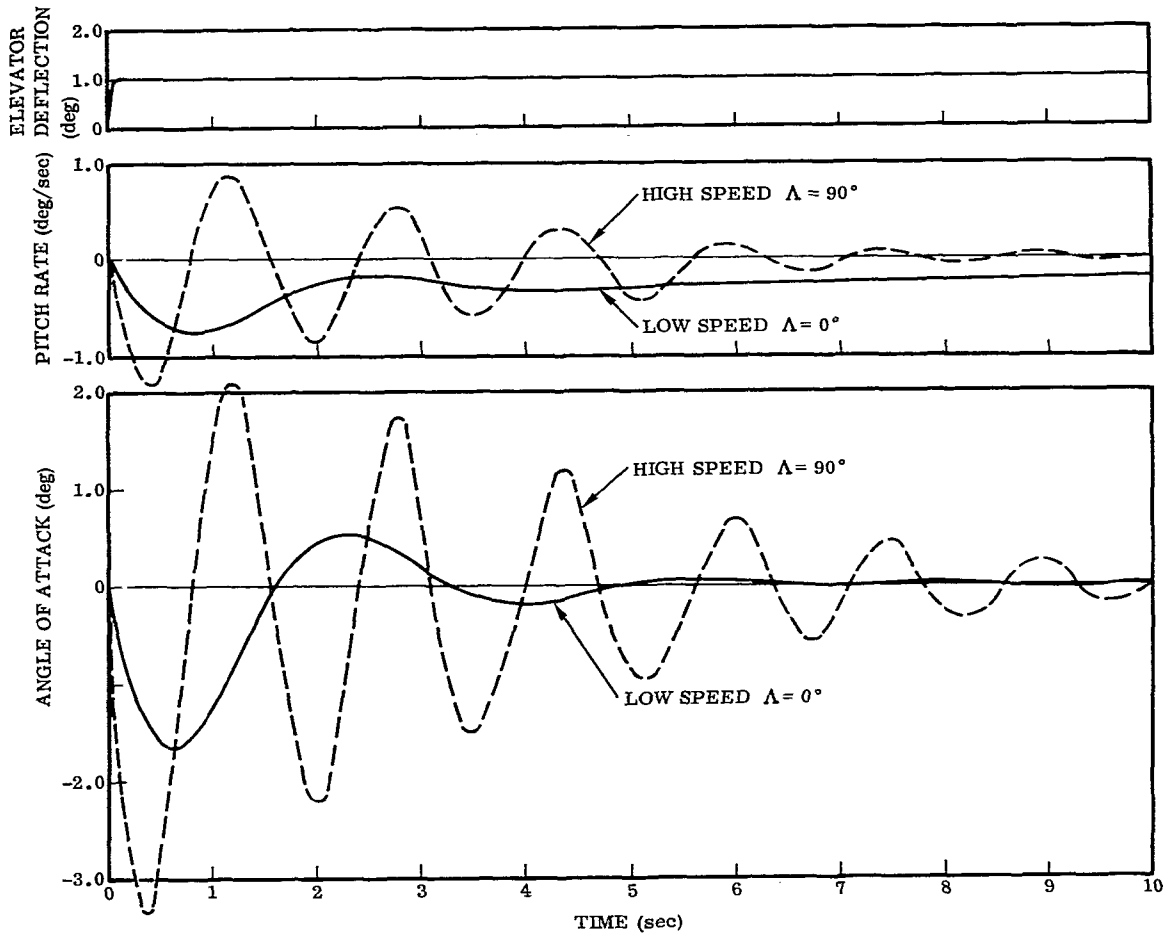

Figure 7-26. Longitudinal Time History for an Elevator Step (Unaugmented)

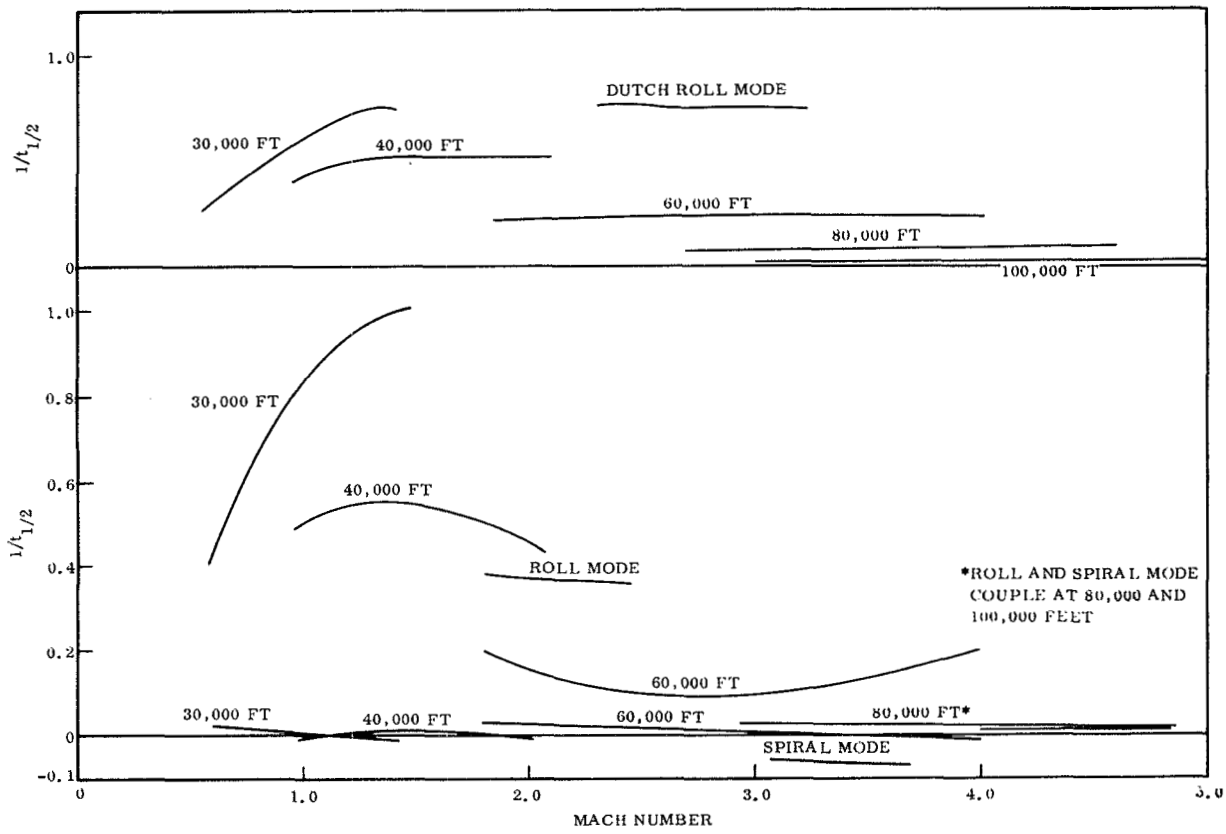

Figure 7-27. Wing Stowed Lateral Characteristics (Unaugmented)

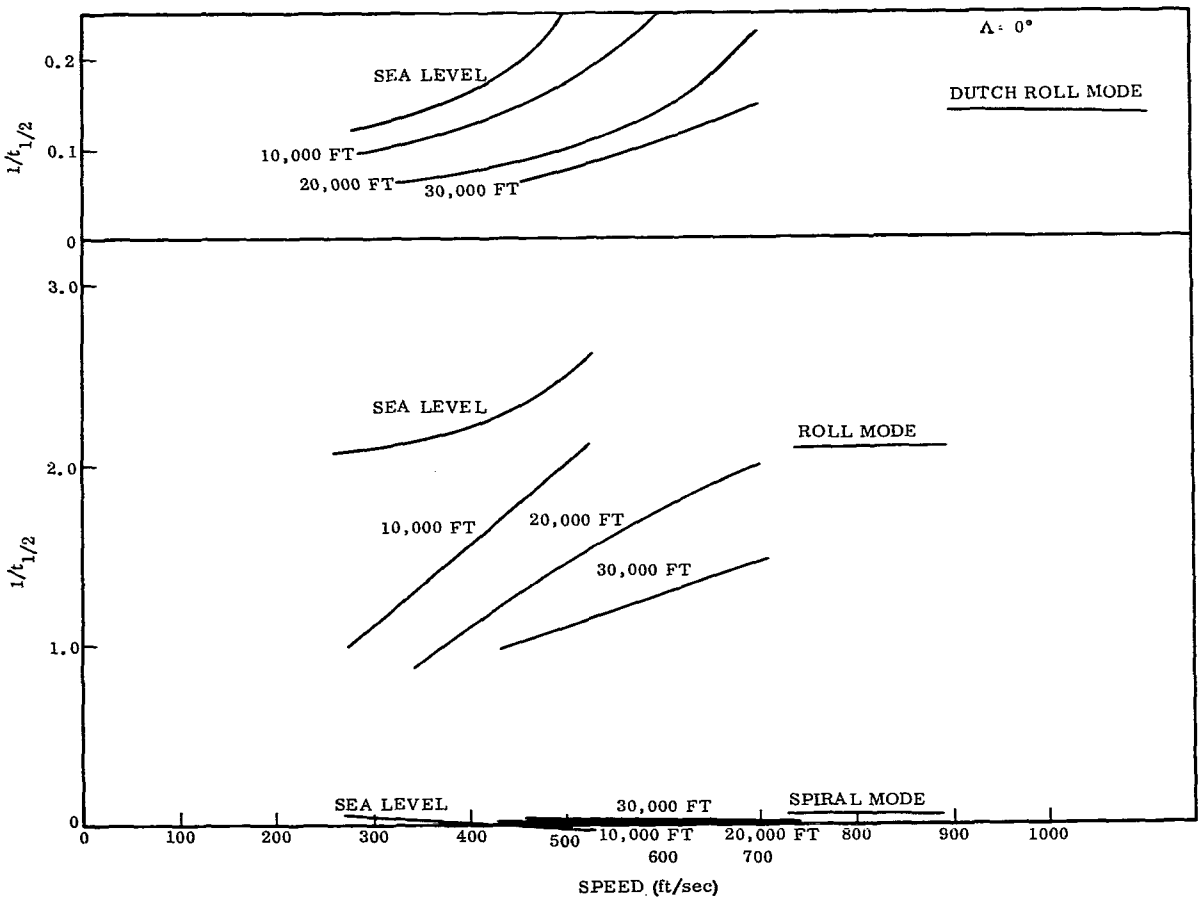

Figure 7-28. Wing Deployed Lateral Characteristics (Unaugmented)

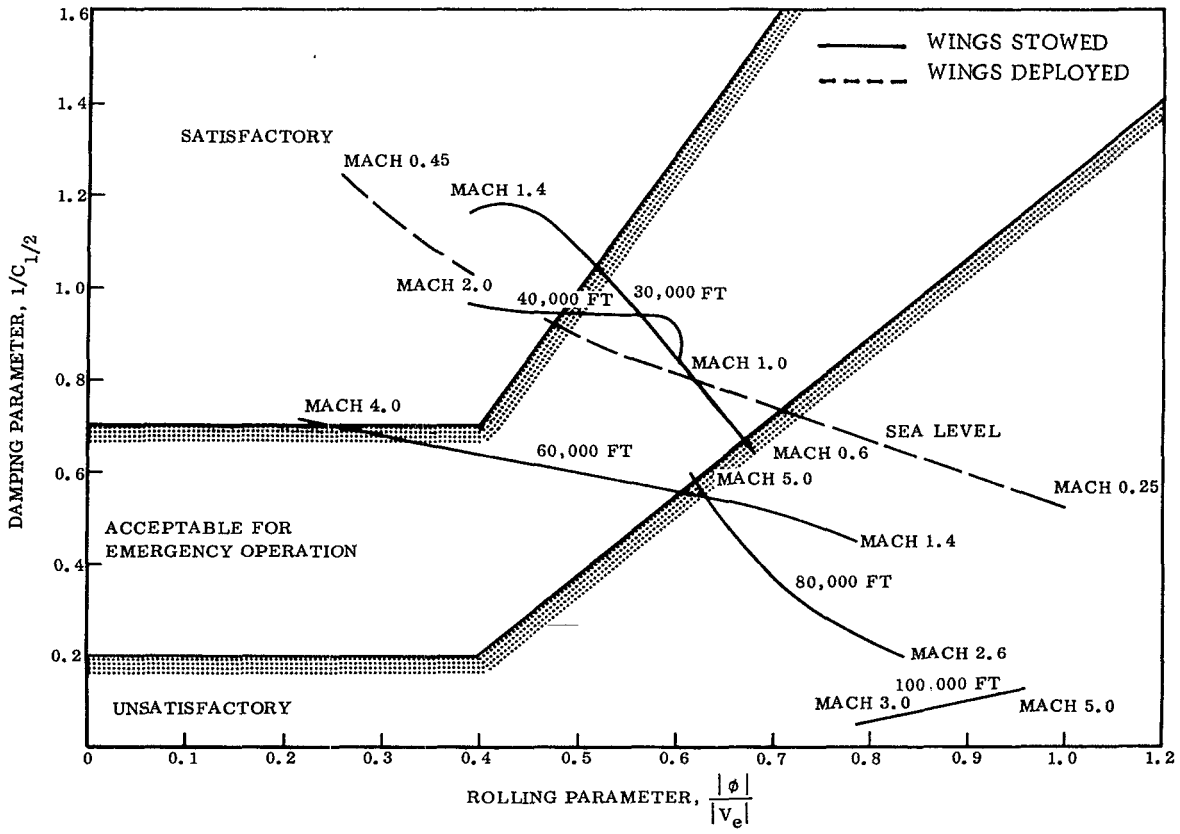

Figure 7-29. Lateral Characteristics in Terms of Military Specification (Unaugmented)

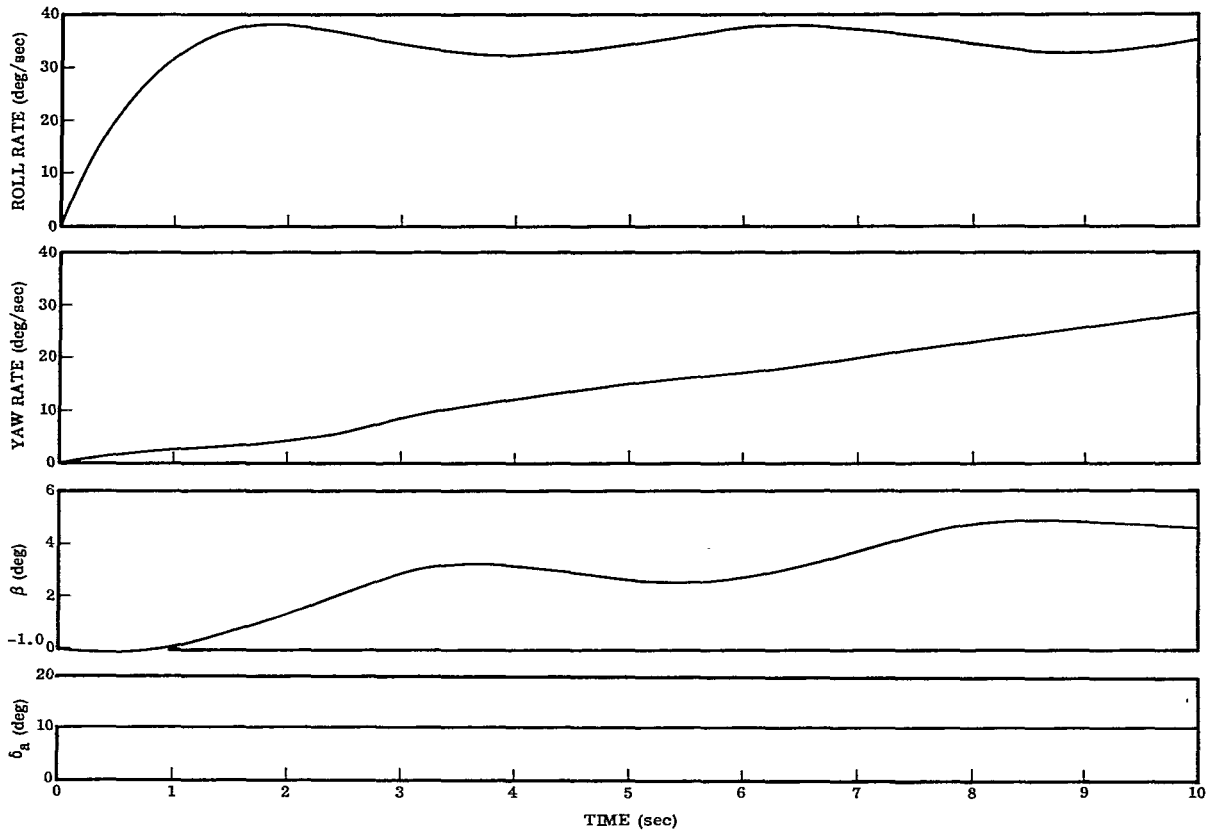

Figure 7-30. Lateral Time Histories at Low Speed for Aileron Step $\Lambda = 0°$ (Unaugmented)

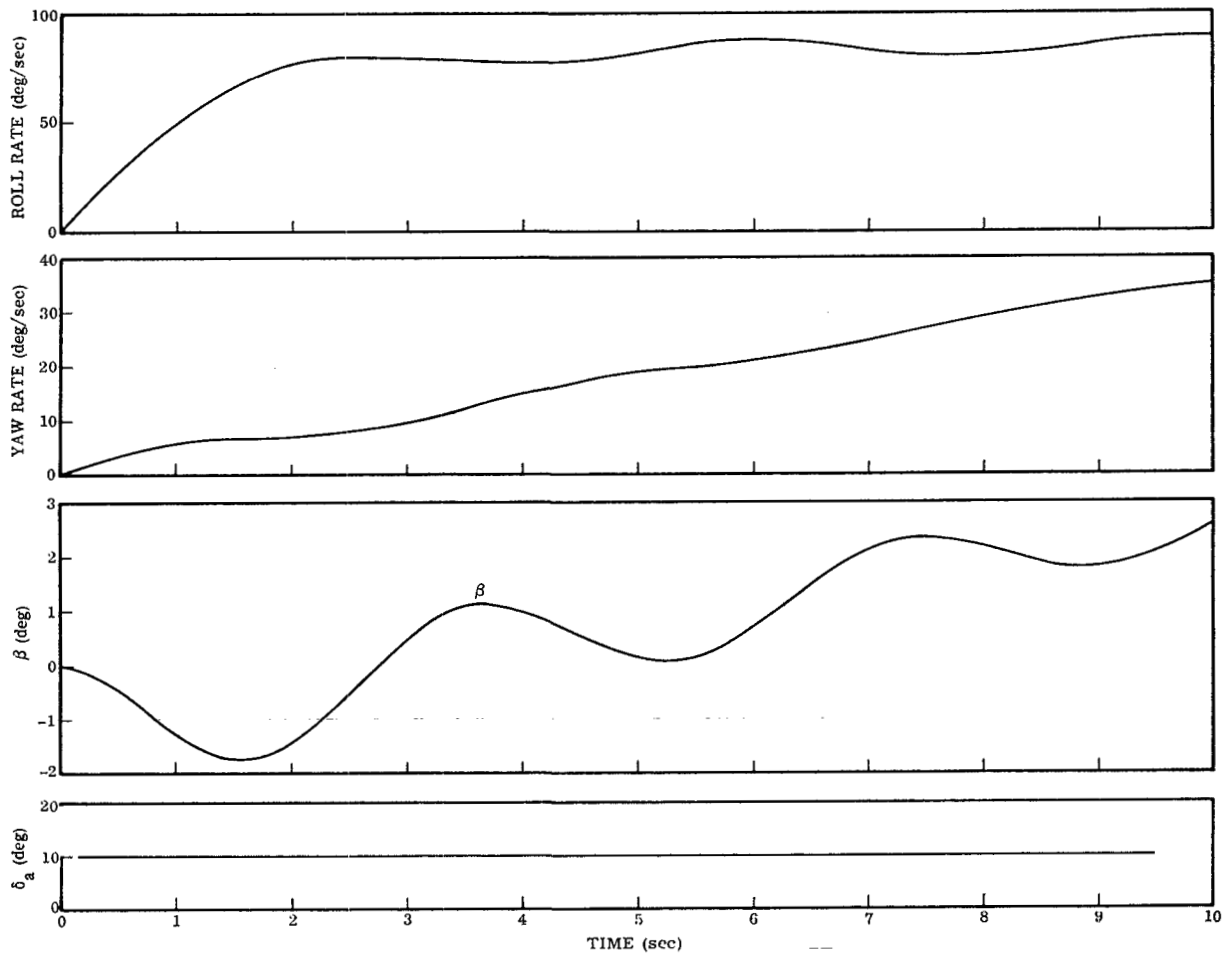

Figure 7-31. Lateral Time Histories at Medium Speed for Aileron Step $\Lambda = 0°$ (Unaugmented)

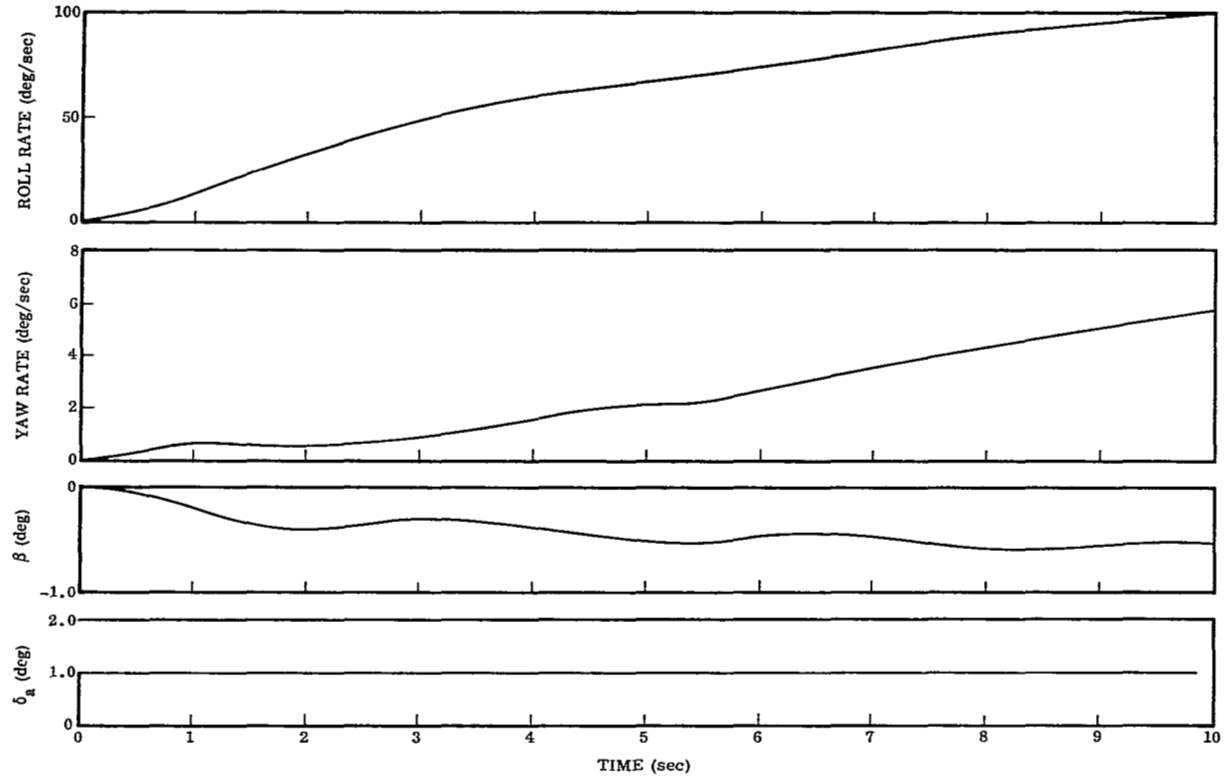

Figure 7-32. Lateral Time Histories at High Speed for Aileron Step ($\Lambda = 90°$) (Unaugmented)

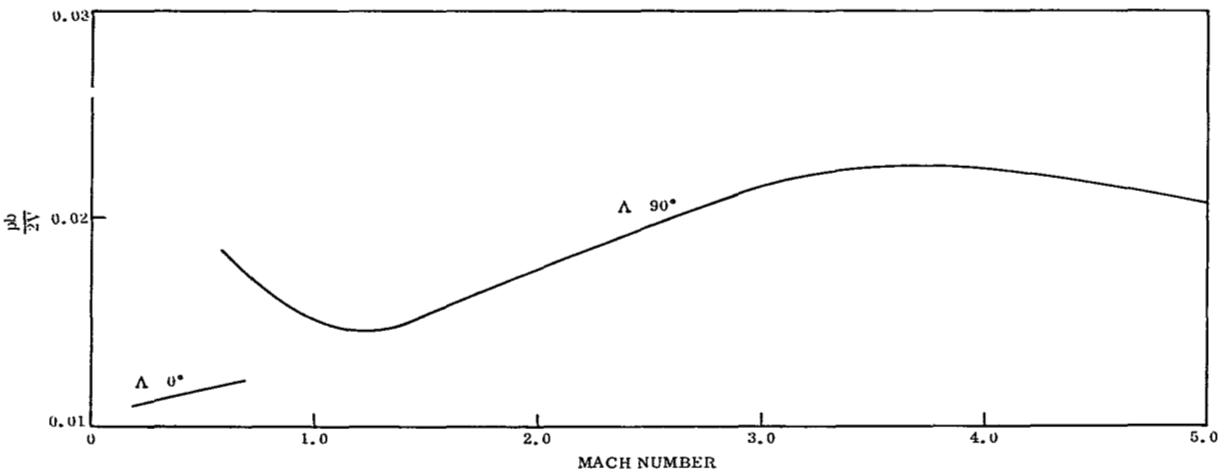

Figure 7-33. Roll Parameter pb/2V

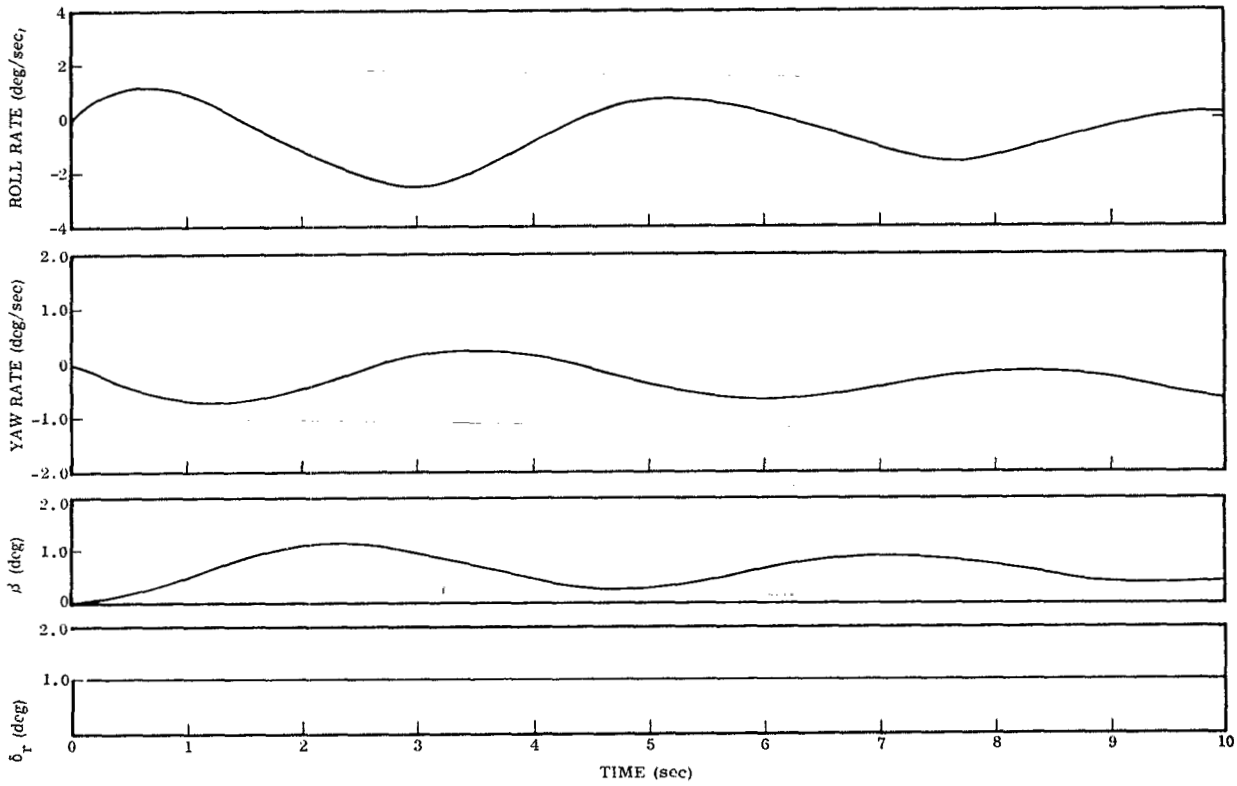

Figure 7-34. Lateral Time Histories at Low Speed for Rudder Step ($\Lambda = 0$) (Unaugmented)

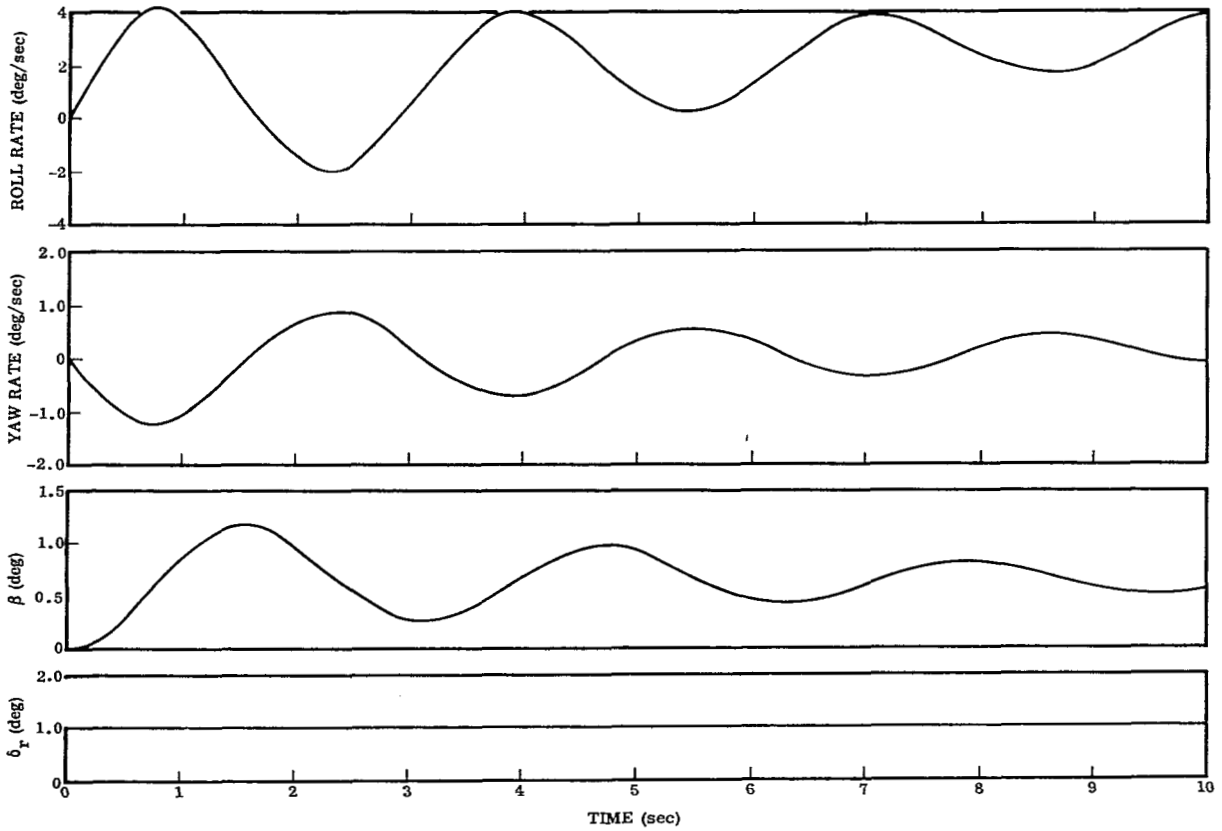

Figure 7-35. Lateral Time Histories at High Speed for Rudder Step ($\Lambda = 90°$) (Unaugmented)

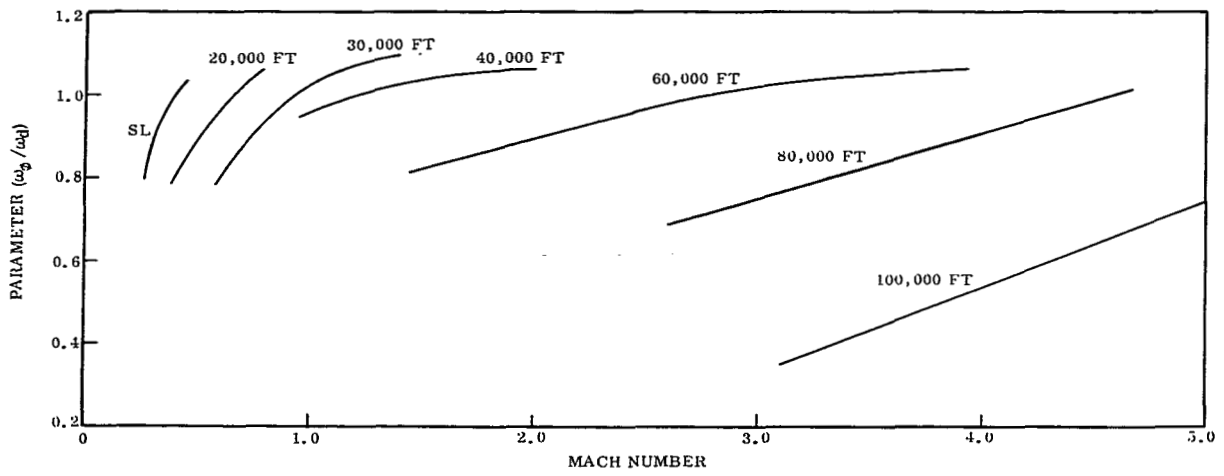

Figure 7-36. Lateral Parameter (ω_ϕ/ω_d)

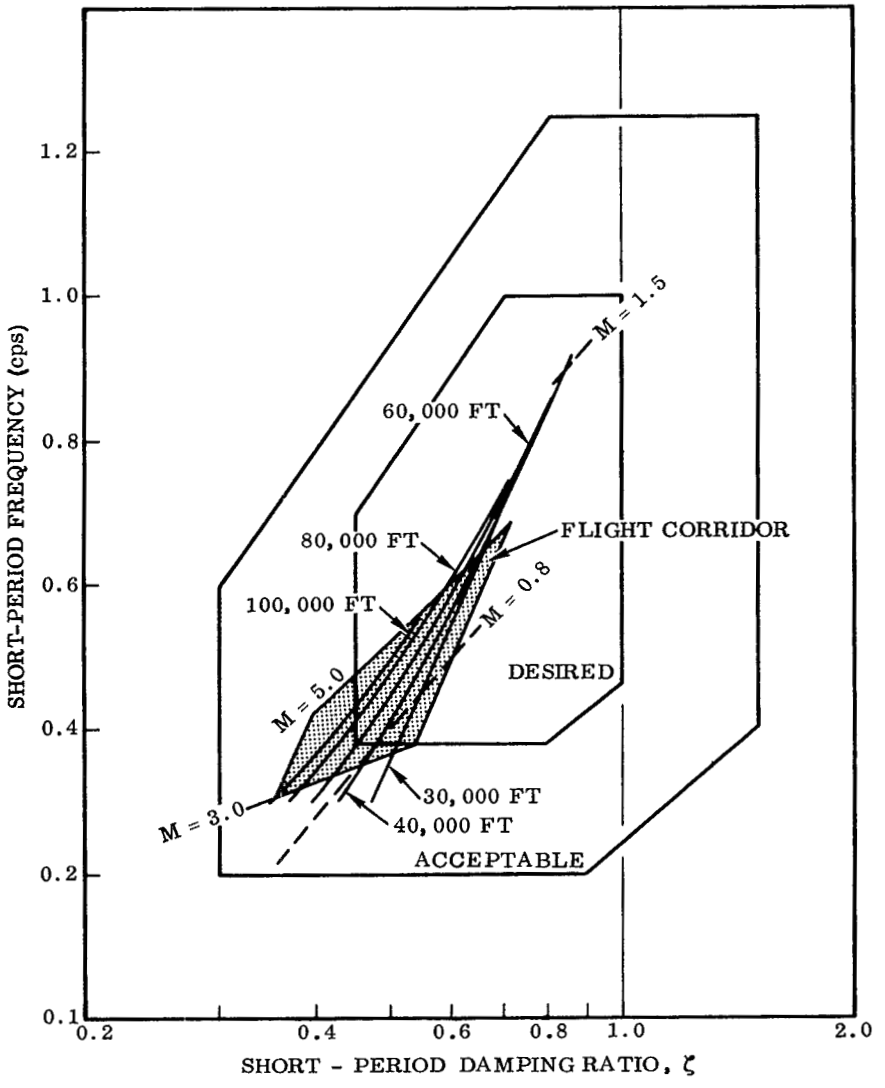

Figure 7-37. Longitudinal Handling Qualities with Augmentation

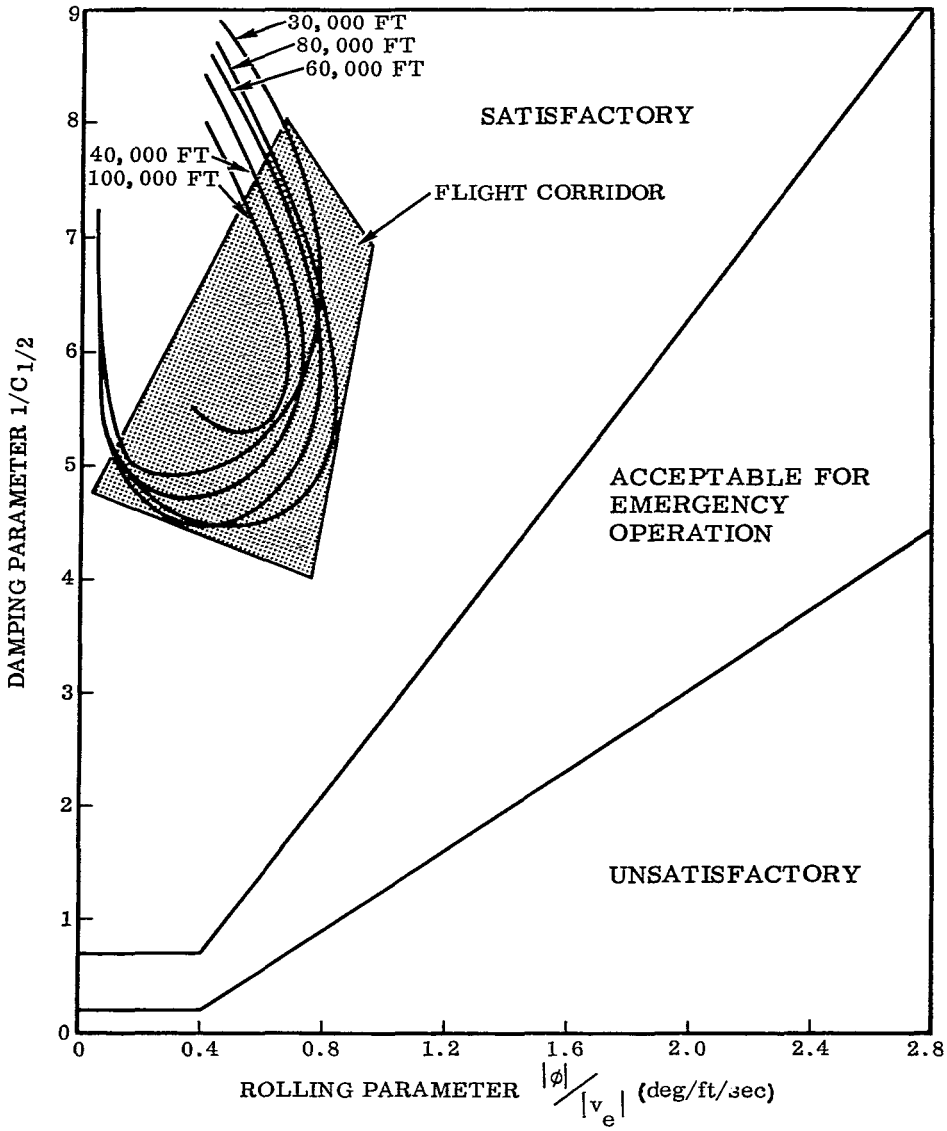

Figure 7-38. Lateral Handling Qualities with Augmentation